INVESTIGATING THE ROLE OF SILICON ON THE ELECTROCHEMICAL PROPERTIES OF POWDER METALLURGY STAINLESS STEELS

BY

JUNIAD AHMED

A Thesis Presented to the
DEANSHIP OF GRADUATE STUDIES

KING FAHD UNIVERSITY OF PETROLEUM & MINERALS

DHAHRAN, SAUDI ARABIA

In Partial Fulfillment of the
Requirements for the Degree of

MASTER OF SCIENCE

In

MATERIAL SCIENCE AND ENGINEERING

APRIL 2016

KING FAHD UNIVERSITY OF PETROLEUM & MINERALS

DHAHRAN- 31261, SAUDI ARABIA

DEANSHIP OF GRADUATE STUDIES

This thesis, written by **JUNAID AHMED** under the direction of his thesis advisor and approved by his thesis committee, has been presented and accepted by the Dean of Graduate Studies, in partial fulfillment of the requirements for the degree of **MASTER OF SCIENCE IN MATERIALS SCIENCE AND ENGINEERING**

4/26/2016

Dr. Ihsan ul Haq Toor
(Advisor)

Dr. Zuhair Mattoug Gasem
Department Chairman

Dr. Tahar Laoui
(Member)

Dr. Salam A. Zummo
Dean of Graduate Studies

Dr. Mohammad Abdul Samad
(Member)

17/5/16

Date

This work is dedicated to our beloved Prophet Mohammad ﷺ and His family.

ACKNOWLEDGMENTS

Firstly, all praise is due to Allah Almighty and countless blessings on Prophet Mohammad (P.B.U.H). I would like to express my sincere gratitude to my advisor Dr. Ihsan ul Haq Toor for his continuous support, patience, motivation during my study and research. His guidance helped me in the completion of my research and in thesis writing. I could not have imagined having a better mentor for my M.Sc. study. Besides my advisor, I would like to thank my thesis committee: Dr. Tahar Laoui and Dr. Mohammad Abdul Samad, for their insightful comments and encouragement. I am grateful to Mechanical Engineering department and KFUPM as a whole for giving me a chance to work.

My sincere thanks also go to Latif Hashmi and Sadaqat Ali, who helped me in various ways to carry out my research. I would like to appreciate my friends Annas, Arif, Irfan, Khan, Moath for the stimulating discussions and for all the fun we have had in our three years. Also I thank my friends in the following institution

Most importantly, I must express my deep and profound gratitude to my beloved parents, my brother and sisters for supporting me spiritually throughout my education and my life in general.

TABLE OF CONTENTS

LIST OF TABLES

LIST OF FIGURES

LIST OF ABBREVIATIONS

SSs: Stainless Steels

MA: Mechanical alloying

PM: Powder metallurgy

B:P: Ball to powder ratio

RPM: revolution per min

XRD: X-ray diffraction

SEM: Scanning electron microscope

BS-SEM: Back scattered SEM

FE-SEM: Field emission SEM

TEM: Transmission electron microscope

STEM: Scanning transmission electron microscope

SCE: Saturated calomel electrode

PDP: Potentiodynamic polarization

LPR: Linear polarization resistance

EIS: Electrochemical impedance spectroscopy

E_{corr}: Corrosion potential

i_{corr}: Corrosion current density

E_{pit}: Pitting potential

i_p: passive current density

XPS: X-ray photo electron spectroscopy

SE-SEM: Seconday electron SEM

ABSTRACT

Full Name : Junaid Ahmed

Thesis Title : Investigating the role of silicon on the electrochemical properties of powder metallurgy stainless steels

Major Field : Materials Science and Engineering

Date of Degree : April. 2016

Stainless steels (SSs), because of their passivation ability and high resistance to environmental degradation, have secured wide spread use in automobile parts, nuclear reactors and structural applications. To meet varying demands of the industry, many different types of SSs have been developed with main constituent elements being Iron, Chromium and Nickel. Depending upon composition and processing technique (micro-structurally different) SSs are classified into four main groups, Ferritic, Austenitic, Duplex, and Martensitic stainless steels. The main problem associated with SSs is their low resistance to localized corrosion under Cl^{-1} concentrated solutions. It has been reported that the addition of Si in Fe-Cr/Fe-Cr-Ni alloys improve the localized corrosion resistance, passivation ability and pitting resistance.

Grain refinement has a significant influence on the mechanical and electrochemical properties of SSs. Nano-structured SSs prepared by powder metallurgy technique have secured their applications in many industries including aerospace, automotive, chemical processing and medical applications. Densification is the most important factor influencing the mechanical and electrochemical properties of PM SSs.

In this work, nano-structured Ferritic [$Fe_{(82-x)}$-Cr_{18}-Si_x (x = 0, 1, 2, 3)]and Austenitic [$Fe_{(73-x)}$-Cr_{18}-Ni_9-Si_x (x = 0, 1, 2, 3)] alloys were developed from pristine elemental powders by mechanical alloying (MA). Nano-structured alloy powders were sintered by spark plasma sintering (SPS) technique to retain their metastable feature. SPS process parameters (sintering temperature, holding time, applied pressure and heating rate) were optimized to obtain maximum densification. Sintering process parameter optimization showed that, maximum densification was achieved at 1100 °C, 15 min holding time, 60 MPa of applied pressure and 50 degree/min heating rate.

The effect of Si content on the densification, hardness and electrochemical properties showed that with the increase in Si content, densification, hardness and corrosion resistance increased as well. The electrochemical investigations showed that, Si has improved the pitting corrosion resistance both in Cl^{-1} and SO^{-4} concentrated solutions.

ملخص الرسالة

الاسم الكامل : جنيد أحمد

أطروحة العنوان: دراسة دور السيليكون على خصائص الكهروكيميائية من مسحوق المعادن الفولاذ المقاوم للصدأ

التخصـــــــــص: علـم وهندسـة المـواد

تاريخ الدرجة العلمية: أبريل .2016

يستعمل الصلب المقاوم للصدأ في قطاع واسع من التطبيقات كقطع السيارات و المفاعلات النووية و الهياكل بشكل عام بسبب قدرته على التخميل و مقاومته للتآكل البيئي. يتم تشكيل الصلب المقاوم للصدأ بشكل أساسي من الحديد و النيكل والكروم والحديد لتركيب صور مختلفة منه مناسبة للحاجات الصناعية المتعددة، و يمكن تقسيم الصلب المقاوم للصدأ إلى أربعة مجموعات رئيسية بناء على التركيب الكيميائي و طريقة التصنيع؛ الفولاذ الفريتي والفولاذ الأوستينيتي والفولاذ المارتنسيتي ودوبكلس الفولاذ. المشكلة الأهم للفولاذ المقاوم للصدأ هي ضعف مقاومة الصدأ المكاني في المحاليل المركزة ب الكلوريد (Cl^{-1}) ، ولذلك اقترح الباحثون إضافة عنصر السيلكيون في سبيكة الحديد و الكروم أو الحديد والكروم والنيكل لتحسين مقاومته للصدأ المكاني والصدأ النقري وتطوير قدرته على التخميل.

أثبت تصغير الحبيبات تأثيره الفعال على الخواص الميكانيكية والإليكتروكيميائية للفولاذ المقاوم للصدأ، وهو ما جعل للتركيب النانوي لهذه النوع من الفولاذ والمبني على تقنيات ميتالورجيا المساحيق تطبيقات واسعة في قطاعات الطيران والمركبات والمعالجة الكيميائية والتطبيقات الطبية. يعتبر التكثيف هو العامل الأهم المؤثر على الخواص الميكانيكية والإليكتروكيميائية للفولاذ المقاوم للصدأ والمعدة بهذه التقنيات.

تم تطوير سبائك الفولاذ الفريتي(($Fe_{(82-x)}$-Cr_{18}-Si_x (x = 0, 1, 2, 3)) والفولاذ الأوستينيتي-($Fe_{(73-x)}$-Cr_{18}-Ni_9 (x Si_x =0, 1, 2, 3)) من المساحيق الأولية عالية النقاوة بتقنية السحق الميكانيكي، والتي تم تلبيدها بتقنية التلبيد بالبلازما والشرارة الكهربائية للحفاظ على ميزة شبه الاستقرار. تمت موازنة متغيرات عملية التلبيد (درجة الحرارة – وقت العملية – الضغط – معدل التسخين) للحصول على أعلى كثافة ممكنة، ونتج عن عملية الموازنة أن المتغيرات الأفضل للحصول على أعلى تكثيف هي درجة حرارة 1100^{o}C و 15 دقيقة كوقت للعملية و 60 MPa للضغط و 50 ^{o}C/min كمعدل تسخين.

أثبتت دراسة إضافة عنصر السيليكون أن التكثيف والصلابة ومقاومة الصدأ تزيد بزيادة كمية السيليكون. أثبتت التحليلات الإليكتروكيميائية أن إضافة السيليكون حسنت من مقاومة الفولاذ للصدأ النقري في المحاليل المشبعة بالكلوريد Cl^{-1} و الكبريتات SO^{-4} .

CHAPTER 1

INTRODUCTION

1.1. Introduction to steels

In metallurgy, word ‘steel’ implies that Fe being the main constituent of the material while the word “stainless” is the ability of the material to resist staining. From metallurgical point of view, to impart “stainless behavior” to steels, the amount of Cr added to Fe must be at least 13 wt%. At this level of Cr addition, a very thin layer of chromium oxide will develop on the surface of steel and have the tendency to self-heal and protect steel from corrosion.

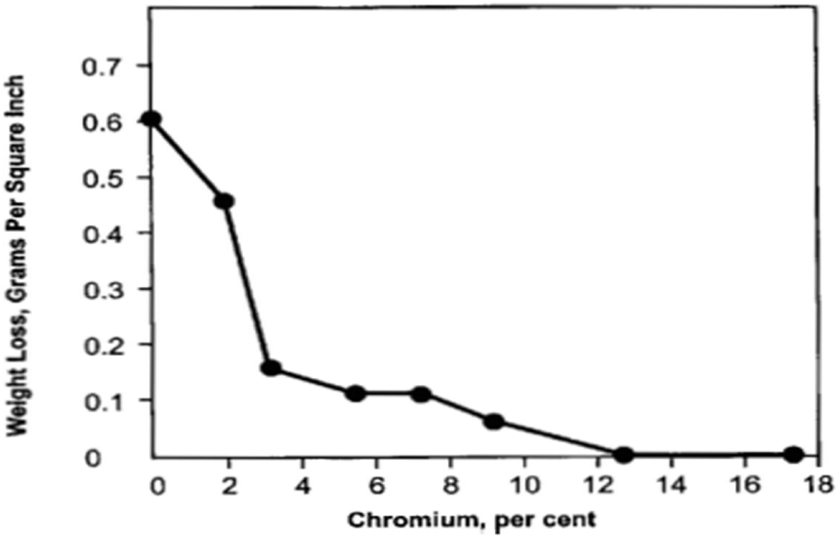

Figure 1.1: Effect of Cr addition on the corrosion rate of carbon steel

In spite of the high thermodynamic reactivity of metals, what makes our metals-based civilization possible is the phenomenon of passivity [1]. Passivity infers kinetic stability of reactive metals in contact with oxidizing aqueous environments, when thermodynamics indicates a large driving force (negative change in the Gibbs free energy) for the reaction of the metal with oxygen (either from O_2 or H_2O) [1]. The observed kinetic stability is due to the formation of a "passive" reaction product/ film on the surface that effectively isolates the reactive metal from the corrosive environment. The passive layer on stainless steels exhibits a truly remarkable property: when damaged (e.g. abraded), it self-repairs as Cr in the steel reacts rapidly with oxygen and moisture in the environment to reform the oxide layer [2]. Increasing the Cr content beyond the minimum of 13% confers still greater corrosion resistance which may be further improved by the addition of 8% or more Ni. The addition of Mo further increases corrosion resistance (in particular, resistance to pitting corrosion), while nitrogen increases mechanical strength and enhances resistance to pitting. Modern SSs, besides Cr, also contain some other alloying elements to enhance some other specific properties and to obtain the required.

Micro-structurally, stainless steels can be classified into several main classes. These are

1. Ferritic SSs
2. Austenitic SSs
3. Martensitic SSs
4. Duplex SSs

All of these classes are different from one another and have different chemical and mechanical properties.

Stainless steel was invented by Monnartz a century ago and suggested its use in cutlery because of its corrosion resistance against attack by some acids [3]. In early 19th century, it was very difficult to produce SSs with very low carbon and high Cr content but with the advent of modern techniques of melting like induction melting, arc melting, it became easy to produce SSs with required compositions.

SSs found their uses in different industries like oil and gas, desalination, automotive, medical and nuclear applications [4]. In automotive industry, the use of Ferritic SSs has had a long history and is very well documented. They found their use in the vehicles moving on the road as well as have been employed in the manufacturing of sea surfers [5]. The 15-5 PH SSs are the best available material for the manufacturing of high speed air planes and 316L are being used in the manufacturing of coronary stents. SSs are also used for the manufacturing of vessels used for storing the radioactive waste from nuclear industry. Duplex SSs are used in making Ferro-plugs which are utilized for temperature measurement below about 600 °C. The measurement of contact pressures during indentation testing, investigation of stresses in sliding tests, uses the phenomenon of transformation of γ to α [6].

1.2. Fe-Cr phase diagram

Equilibrium system can be defined as, a system with minimum free energy at a given temperature and pressure i.e. there is no excess energy and consequently no driving force to cause any change. In a system involving many constituent elements/ phases, it is necessary to consider the free energies of all the constituent elements and phases. The concept of chemical potential or activity is a consequence of the relationship between the free energies of all the phases and their compositions. The calculation of equilibrium phase diagrams requires knowledge of free energy-phase composition relation as a function of temperature. In fact, the intrinsic free energies are not known and it is the difference in free energy with respect to a known common reference state is employed. Various methods like first principle and optimization of thermodynamic parameters are used to express the free energy and the interaction between atoms [7].

First Fe-C phase diagram was developed in 1899 and then experimental research is going on to develop other phase diagrams. To develop phase diagrams, experimental techniques like optical microscopy, XRD, chemical analysis, DSC, dilatrometery and TEM are frequently employed but the fact is, to develop a simplest phase diagram enormous work is required.

Fig. 1.2 shows the experimentally calculated Fe-Cr phase diagram where there are three important regions [8].

- Existence of two phase region called gamma loop separating the ferrite and austenite regions.
- Formation of intermetallic σ-phase.
- Separation of ferrite regions into α and α' regions at low temperature.

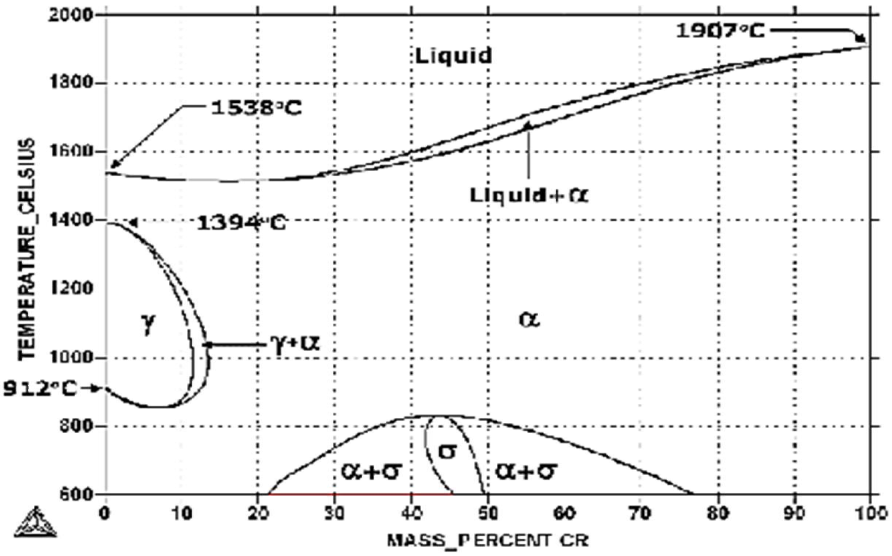

Figure 1.2: Equilibrium phase diagram of Fe-Cr system

1.3. Powder Metallurgy (PM)

PM is getting popular day by day as it is a cheap route for the manufacturing of small components with complex shapes and there is no metal loss from machining and finishing [9]. PM offers some other advantages such as good precision in dimensions, high surface quality, broad chemical composition, good physical and mechanical properties. There are many emerging applications of PM parts in automotive industry as well as in oil and gas sector [5]. The sintered components are designated for engine parts, gear boxes, shock absorbers, cams, sprocket, synchronizer and brake systems. Applications for offshore include metallic filters, anti-corrosive painting, thermal spray coatings, valve body, elbow raiser and there are many more [7].

Use of PM parts in automotive industry includes, ABS (antilock brake sensors) that is made from Ferritic SSs made because of their soft magnetic nature. Their oxidation properties made them best choice for applications like turbo compressors, solid oxide fuel cells and parts of automotive exhausts.

CHAPTER 2

LITERATURE REVIEW

2.1. Nano-structured SSs

Research have shown that grain refinement can improve both the corrosion and mechanical properties; however, grain refinement was limited to a few microns [4]. A nanocrystalline structure in SSs has been reported to impart significantly higher oxidation resistance (owing to greater Cr diffusion and ease of formation of compact Cr-oxide layer), and mechanical properties as compare to conventional coarse grain counterparts of the same chemical composition [10]. The credit of unique properties of nano-crystalline materials goes to very fine grain size and a large number of structural/crystal defects, i.e., grain boundaries and triple points [10]. Such a high fraction of structural defects in nano-crystalline materials can lead to a significant increase in free energy which may increase the reactivity of the material. This phenomenon is expected to have a dual effect on corrosion behavior which depends upon material/environment system as reviewed in [11]. In passivating electrolytes (i.e., stainless steel in many aqueous environments) a nanocrystalline structure has been reported to impart an improvement in corrosion resistance, whilst in depassivating electrolytes a decrease in corrosion resistance is reported [12].

Diffusivity of alloying/impurity elements in nanocrystalline materials are reported to be significantly higher than that in conventional coarse grained materials due to considerably higher volume fraction of grain boundaries [12]. Detailed discussion of the diffusion processes in the Nano crystalline material is reported elsewhere [13]. The increase in the diffusivities of solute/impurity atoms in nanocrystalline alloys (and Cr in SS [13]) was reported to influence corrosion behavior. However, recently it was proposed that the diffusion coefficient of Cr in SSs at room temperature, even in nanocrystalline alloys, was too low to cause any significant influence on corrosion behavior of SSs [14]. These contradicting views related to the influence of diffusion on corrosion at room temperature require further investigations.

2.2. Corrosion resistance of SSs

The corrosion resistant property of stainless steels is because of the presence of very thin, typically 1-3nm thick, film called passive film and the phenomenon of film formation is called passivation [15]. For the understanding of growth and kinetics of passive film formation, various theories have been put forth. Earliest one is known as "High Field Model" which assumes that, the formation and growth of the passive film is controlled by "*cation*" transfer rate between adjacent lattices with in the passive film [4]. Then later, "The Mott-Cabrera" model was proposed and it states that, diffusion of metal ions from metal to film at metal/passive film interface is the most important step which determines the formation and growth of the [16]. It was then modified by Fehlner and Mort and stated that, the rate determining step of film formation is the diffusion of "*anion*" from electrolyte into passive film at electrolyte/film interface [17]. The most comprehensive model of passive film was proposed by Macdonald and co-workers. This model is known as "Point defect model" (PDM) which account for the mobility of both positive and negative ions, vacancy, cation and anion interaction, and the reactions carrying out at the passive film/electrolyte and metal/passive film interface. The PMD has also been extended to study the breakdown of passive film and the role of alloying element on the passive film formation [4].

After detailed investigation on passivity of SSs, it is now well established fact that, the addition of Cr to Fe leads to the improvement in corrosion properties. The addition of Cr causes the enlargement of pH region of stable passivity, decrease in passive current density, repassivation potential shifts to more negative potential, pitting resistance increases significantly. The formation of passive film is attributed to the selective dissolution of Fe and formation of Cr-oxide. The role of alloying elements on the formation of passive film has been studied widely. And suggested that, Cr content >50% in passive film is essential for its stability. The % of Cr content in passive film increases with the increase in Cr content of the alloy. Passive films are susceptible to break down in aggressive solutions, pH changes and temperature. Breakdown of passive films lead to a phenomenon called “pitting”.

Pitting can be characterized in three stages: [4]

(1) Pit initiation or nucleation caused by the breakdown of the passive film. Nucleation events are followed by repassivation.

(2) Metastable pitting where pit growth stops on the verge of stability. Metastable pits grow for a finite time and size before repassivation. Metastable pitting is proposed to be a measure of pitting susceptibility.

(3) Pit growth where pits grow as long as the pit interior can maintain the sufficiently aggressive electrolyte such that repassivation is prevented.

2.3. Effect of alloying additions on the properties of SSs

Alloying elements in SSs are added to improve mechanical and corrosion properties or to obtain a specific microstructure. A very common way to index the corrosion resistance of SSs is PRE (Pitting Resistance Equivalent) which is evaluated as PRE = %Cr + 3.3 %Mo + 16 %N. From the equation, it can be deduced that, Cr, Mo and N play the most important role in improving the pitting corrosion resistance of SSs. Let’s discuss the role of different alloying additions in SSs

Carbon is an important alloying addition in all Fe based alloys and is present in almost all grades of SSs and heat resistant alloys. The percentage of carbon is kept to low levels in all austenitic, ferritic, and duplex stainless steels to retain the desired microstructure and mechanical properties. In martensitic SSs, carbon plays a very important role in increasing the strength and hardness because it forms martensitic structure. The effect of Carbon on the electrochemical properties can be studied by determining the form of carbon in the alloy**.** If it is present in combined form with Cr by forming chromium carbide, it will decrease the corrosion resistance of the steel. As it remove the Cr from the bulk and thus decreasing the amount of Cr available to provide corrosion resistance to the alloy. This detrimental effect of carbon is because of the slow cooling of hot worked or annealed samples. This slow cooling resulted in an unwanted precipitation of Cr-carbide at the grain boundaries and this phenomenon of precipitation of Cr-carbide at grain boundaries is known as "*sensitization"*. This precipitation of carbide decreases the corrosion properties and making the steel vulnerable to localized corrosion i.e. intergranular corrosion at the grain boundaries following the carbide phase [18].

Cr plays the most important role in imparting the corrosion resistance of steel as the high reactive nature of chromium laid the principle for the addition of chromium in SSs. As discussed in section 2.2 that, good corrosion resistance of SSs is because of the formation of a protective and adherent passive film that protects the substrate from corrosion. The passive layer is of the order of 1-2nm thin. But it imparts high corrosion resistance. It has also been explained that the corrosion resistance to iron-chromium alloys increases as the chromium content increases [18].

Si is not only a very good deoxidizer in SSs but also improve their oxidation resistance and reported to increase hardness and reduces ductility [19] Toor et al. have reported that, addition of Si helps to increase the pitting corrosion resistance of the alloys [20]. Thomasov et al. studied the effect of various alloying elements on the variations in the intensity and nature of pitting corrosion as well as the mechanisms involved in rendering stainless steels less susceptible to pitting corrosion by the specific effect of the alloying elements [21].

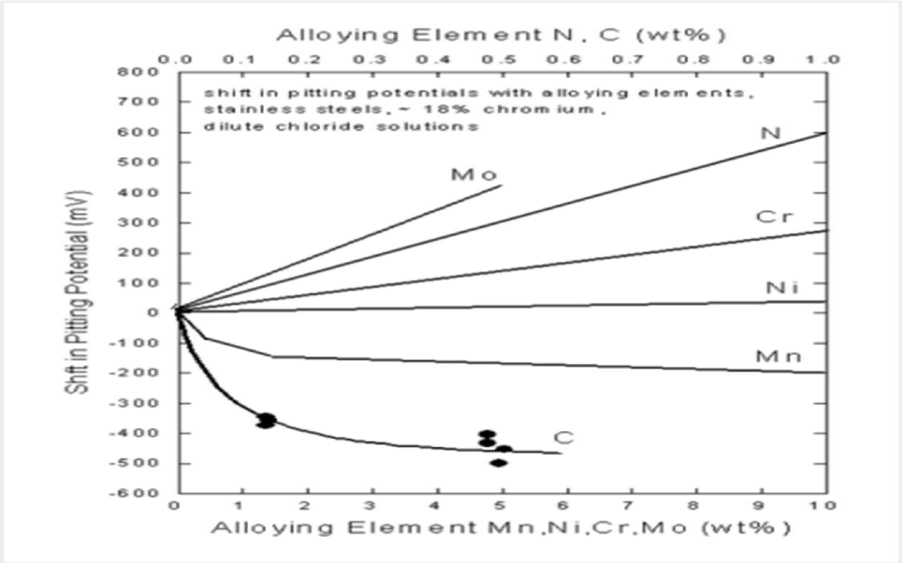

Figure 2.1: Effect of alloying elements on the pitting potential of Fe-18Cr-14Ni SSs

Fig. 2.1 illustrates the effect of different alloying elements on the corrosion rate of Fe-18Cr-14Ni SSs in a 0.5N $FeCl_3$ solution. Increase in Mo, Ni, N, Mn will increase the pitting corrosion resistance while increase in C will decrease the pitting resistance and the steel will be prone to localized corrosion.

The maximum amount of Molybdenum added in SSs is up to 8% but generally it is added in the range of 2 to 4%. Even with such small percentages of Mo, it plays a powerful role in improving the pitting corrosion resistance and crevice corrosion resistance of both Fe-Cr and Fe-Cr-Ni alloys especially in chloride environments [22].

Mn acts as a deoxidizer in liquid metal and also imparts specific properties. Mn has a high affinity towards oxygen forming MnO and with Sulphur forming MnS. The formation of MnS is very beneficial as Sulphur in the absence of Mn reacts with Fe and causes hot shotness and cold shotness [22].

Since the objective of the research was to investigate the corrosion properties of Si containing SSs, the following paragraphs will review the effect of Si on the electrochemical behavior of SSs.

Most commercially produced stainless steels (SSs) contain Si as alloying additions because Si acts as oxygen absorber in liquid metal. Moreover, it is been reported that, the small addition of Si content increases high temperature oxidation resistance of wrought stainless steels in both austenitic [23] and ferritic SSs [24]. It is also been reported that, the addition of Si to SSs also suppresses breakaway oxidation at high temperature [24]. The advantageous effect of Si is because of the formation of Silica at the interface of external Chromia layer and the base metal. Which acts as diffusion barrier for cation transport [23, 24]. Some authors also suggest the increase in oxidation resistance is because of the discontinuous network of Silica particles both at and beneath the Steel-Chromia interface [25]. Thus Silica acts to reduce the flow of cation from bulk substrate to the scale [26]. In wrought SSs, the effect of Si content on the localized corrosion resistance at room temperature has also been studies [27]. The Ferritic SSs have shown more sensitive behavior to corrosion resistance affected by the addition of Si than austenitic stainless steels [27].

Many researchers have studied the effect of Si content on the electrochemical properties. Toor et.al [20] investigated the Si effect on the repassivation kinetics and SCC susceptibility of SSs and concluded that, Si improves the localized corrosion resistance. The reason being is the enrichment of Si in the passive film. Nishimura et.al [28] investigated the effect of Si content on high temperature oxidation properties of Fe-Cr and Fe-Cr-Ni alloys in CO_2 environment and reported that, Si delayed the oxidation of alloys at high temperature. Perez et.al [27] investigated the effect of Si ion implantation on the localized corrosion of SSs and reported that, Si improved the pitting corrosion resistance. Sharon et.al [29] investigated the Si effect on the mechanical and corrosion properties of PM SSs. And there are many more

2.4. Mechanical Alloying (MA) and Milling

Suryanarayana defined MA, as "It is a process in which a homogenous alloy will form by involving the powders in solid state causing the transfer of material during the operation". During this process, material transfer takes place to obtain a homogeneous alloy [30]. This technique was developed in 1966 by John Benjamin and his colleagues to developed nickel based super alloys for gas turbine application. Basically they were trying to combine dispersed oxide (high temperature strength) and gamma prime precipitate (intermediate temperature strength), at the same time obtaining the high corrosion resistance. Till 1980's MA was not considered as the true alloying process. Then Koch et al. published a landmark paper which, for the very first time demonstrated the mechanism of alloying in ball mill and proves that MA can form true homogenous alloys. They also stated that, the outcome of the MA process can be a metastable material such as an amorphous alloy [23].

The entire process of MA starts with the blending of elemental powder with required chemical stoichiometry and providing the vials with required operating medium i.e. inert atmosphere or vacuuming the vials to avoid any oxidation of the powders.

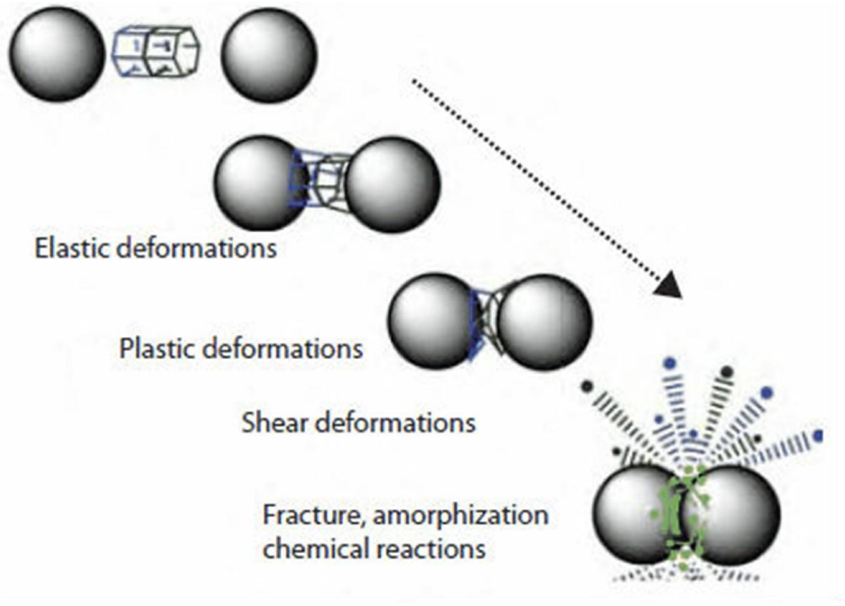

Figure 2.2: Working principle of mechanical alloying

MA process can be classified into two steps. First, the powder particle having high flow-ability and low friction will be deformed by the impact force of grinding media leading to work hardening. Further milling will result in more work hardening and ultimately result in the fracture by fatigue failure mechanism and by the fragmentation of fragile flakes. In this stage there is no agglomeration force between the powder particles and thus will continue to fracture. Secondly, formation of new surfaces yields the increase in surface energy of the new particles and this can bring the agglomeration of particles due to existence of van der Waal forces. Powders having less flow-ability and irregular surfaces trap between the balls and self-binding enables them to cold weld these particles. Thus increases the size of the particles

Fig. 2.2 illustrates the process of alloying or metastable phase formation while Fig. 2.3 shows the principle of size reduction of powders during milling operation.

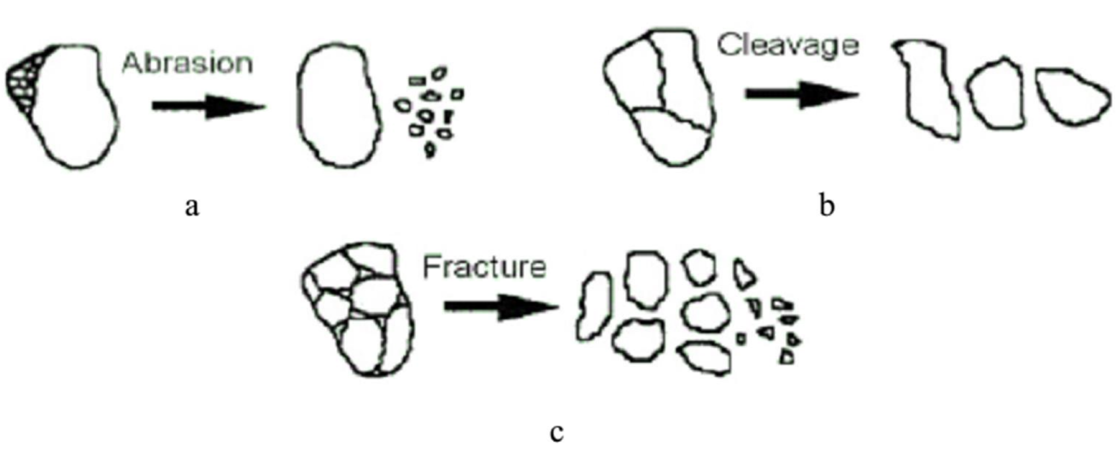

Figure 2.3: Working principle of size reduction during MA

During MA process, lots of phenomena are occurring at the same time. To obtain the required product the whole process need lot of optimization and precautionary measurements [31].

The milling machines are of different types and they differ in their capabilities, speed and ability to control the operation. Selection of mill is important before starting the milling operation. The selection of mill depends on the type of powder, quantity of the powder and constitution/phase required at the end of milling. For example, The SPEX shaker mill will be used for alloy screening purposes, when bulk powder will be needed planetary ball mills or the attritors will be used.

The selection of milling vials/ containers are important as Suryanarayana [31], stated that, the material of the vials should be of the same composition as that of the powders to be milled. As during milling operations, the grinding action of the balls and the walls of the vials may contaminate the milled powders. This contamination may give rise to the phases that are not required or may results in metastable phase formation [31]

The speed to the mill is among the most important parameters to be controlled for the achieving the required phase and size of the powder after milling. But there are some limitations for the speed of the mill. For example, in conventional ball mill, increasing the speed of the mill above certain critical speed will pin the balls to the walls of the vials due to high centrifugal force. Thus the balls will not fall onto the powders. Another limitation of speed of the mill is, very high speed will increase the temperature of the vials which can be beneficial and can degrade the system. High temperature of the vials can be beneficial when the homogenization of the phases is required and can be disadvantageous as it can contaminate the powders [31].

Time given to milling is the most important parameter of the milling process as it defines the steady state achievement between fracturing and cold welding of the powders. The time given to milling process also depends upon the ball to powder ratio employed, type of mill, milling temperature etc.

Ball to powder ratio is very important parameter defining the time given for milling. In principle, the higher the charge ratio, shorter will be the milling time [31].

2.5.Spark Plasma Sintering (SPS)

Spark plasma system has been often known by a name of spark plasma sintering or plasma activated sintering. SPS is a complete description owing to its ability to sinter metals, ceramics, polymers, joining of metals, crystal growth and can give rise to chemical reactions. SPS is most state of the art technology that enables the powders to be densified to the maximum extent at much lower temperature and in short period of time by introducing the intervals of high electrical energy between powder particles and high sintering pressure [32,33]. SPS incorporate moderate uni-axial pressure (typically < 100MPa) along with on-off DC pulsating current to bring about sintering. During on-off period of DC current, number of proposed mechanisms occurs to speed up the sintering process. These can be spark impact pressure [33] cleaning of particle surface by plasma [34], joules heating, local melting/ evaporation, particle surface activation and diffusion due to electric field [35].

As far as consolidation is concern, Processing temperatures are the most critical step in retaining the nanocrystalline structure, generated during MA, by impeding the grain growth. SPS has the ability to produce nano-grained stainless steels having high density and remarkable properties without changing their fundamental chemical composition.

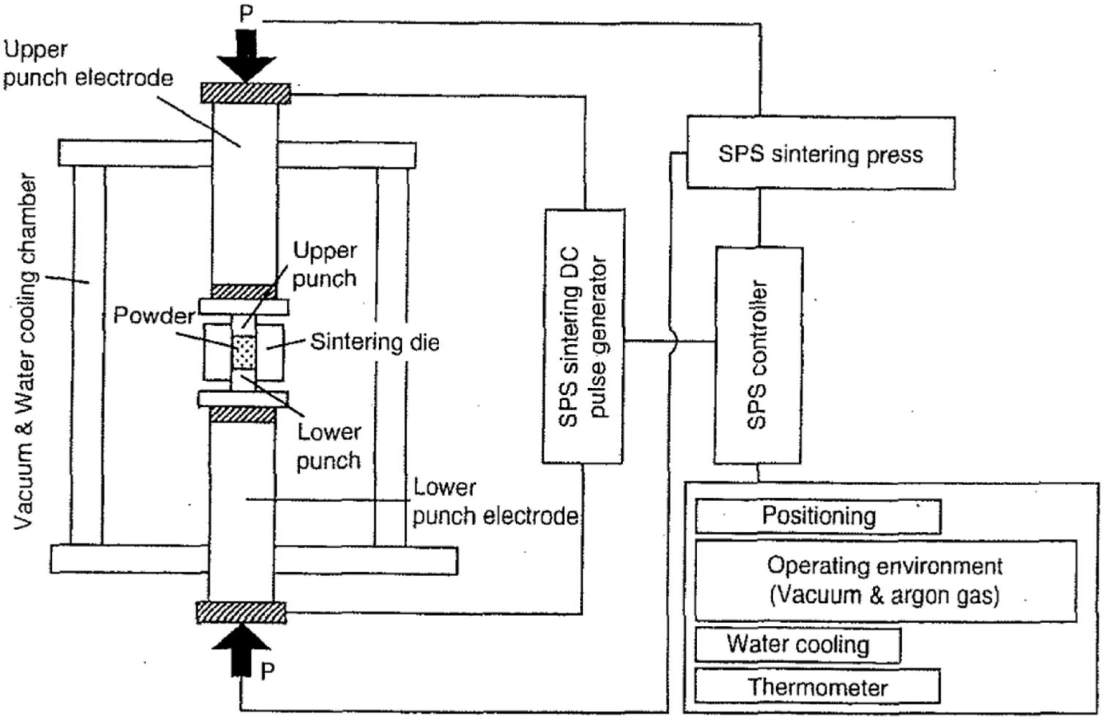

Figure 2.4: Working principle of spark plasma sintering process

The main advantage of SPS is direct heating of the sintering graphite mold and the powders in the die. Because of high thermal efficiency of SPS process, a very high quality sintered body can be made [36]. In the SPS process, the passage of DC current from the powder particle surfaces purify and activate them and material transfers at both the micro and macro levels take place. So, in this way, a high quality sintered body can be obtained at much lower temperature than that of conventional sintering process. Fig. 2.5 shows the flow of DC current from the powder particles during sintering process.

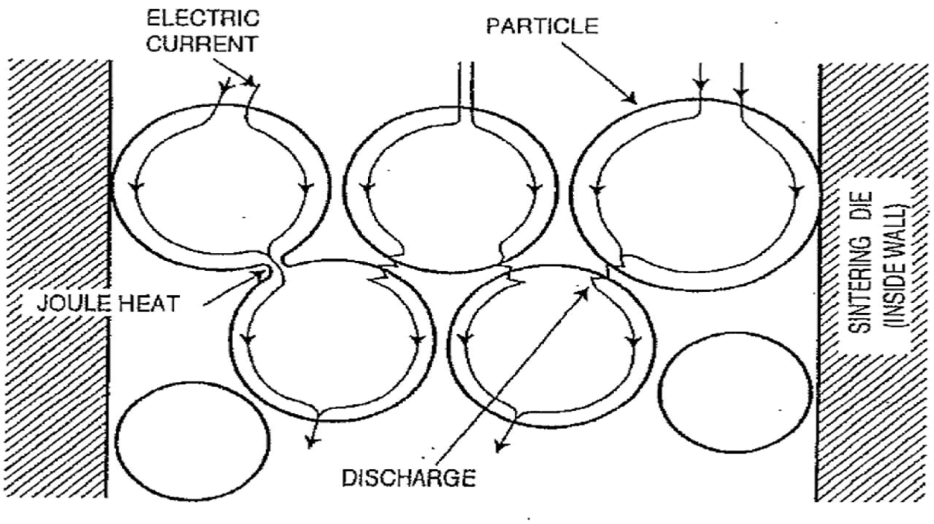

Figure 2.5: Flow of DC pulsating current through powder particles in SPS process

The basic mechanism involved in sintering with SPS can be explained as "when a spark is being generated between the powder particles, it gives rise to the localized increase in the temperature to ten thousands of centigrade just for the very small amount of time. This very high temperature causes evaporation and melting at the surface of the powder particles and the formation of neck between the particles take place. Fig. 2.6 illustrates the formation of plasma during DC current flow while Fig. 2.7 shows basic mechanism of neck formation by the plasma.

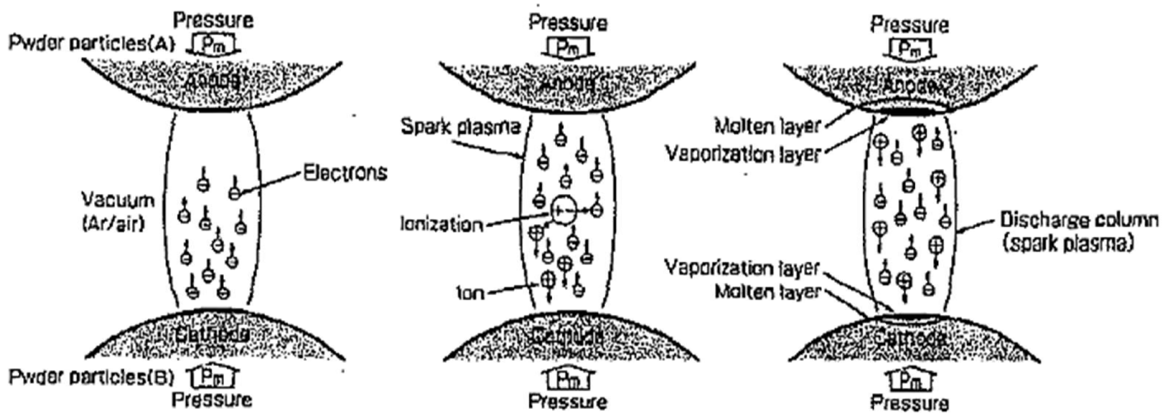

(I) Initial stage of spark discharging by ON-OFF pulse energization (II) Generation of spark plasma (III) Vaporization and melting actions on the particle surfaces

Figure 2.6: Generation of plasma due the spark generated because of the DC pulsating current during SPS

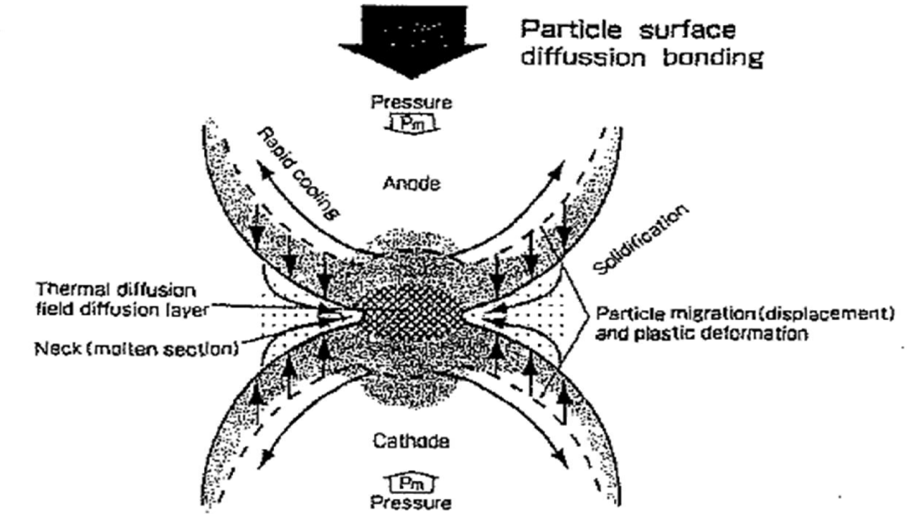

(V) Neck formation by spark plasma

Figure 2.7: Neck formation between the powder particles due to the flow of DC pulsating current during sintering process

2.6. PM SSs and their corrosion behavior

SSs produced by PM are getting popular day by day and they have found their huge applications in automotive industry. PM involves the manufacturing of metal powders, consolidation at high pressure and sintered under control atmosphere for limited time. Due to huge applications, electrochemical properties of PM SSs are of greater concern these days. In this section, the work that has been done to develop SSs by PM and their electrochemical investigations has been reviewed.

Raman et al. [37] prepared Fe-10Cr alloy by using high purity (99.9%) powders in high energy ball mill SPEX Model 8000 shaker for 20hs with ball to powder ratio (BPR) 10:1. Their basic work was to investigate the effect of grain size of the alloys produced by MA and have reported the increase in oxidation resistance of nano-crystalline structure as compare to microcrystalline structure (Fig. 2.8).

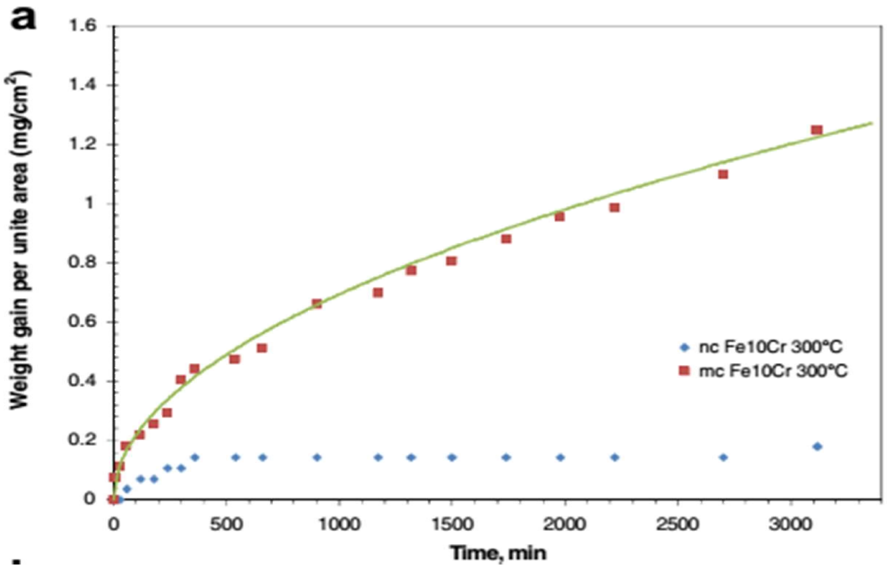

Figure 2.8: Comparison of weight gain with time for nano crystalline vs microcrystalline structured Fe-10Cr alloys

Gupta et al. [38] manufactured nano-crystalline Fe–Cr alloys using high energy ball milling and successfully consolidated them at 600 °C. Nanocrystalline and coarse grained alloys thus prepared were used to investigate influence of nanocrystalline structure on corrosion performance in H_2SO_4 with and without Cl^{-1}. Electrochemical properties of nanocrystalline Fe–Cr alloys (52 nm) were found to be superior to that of their coarse grained (1.5μm) counterparts. Nanocrystalline structure decreased the passive current density, increased breakdown potential (in presence of chloride ions), and decreased passivation potential and critical current density (Fig. 2.9). This marked improvement in corrosion behavior was attributed to the greater Cr enrichment of the passive film.

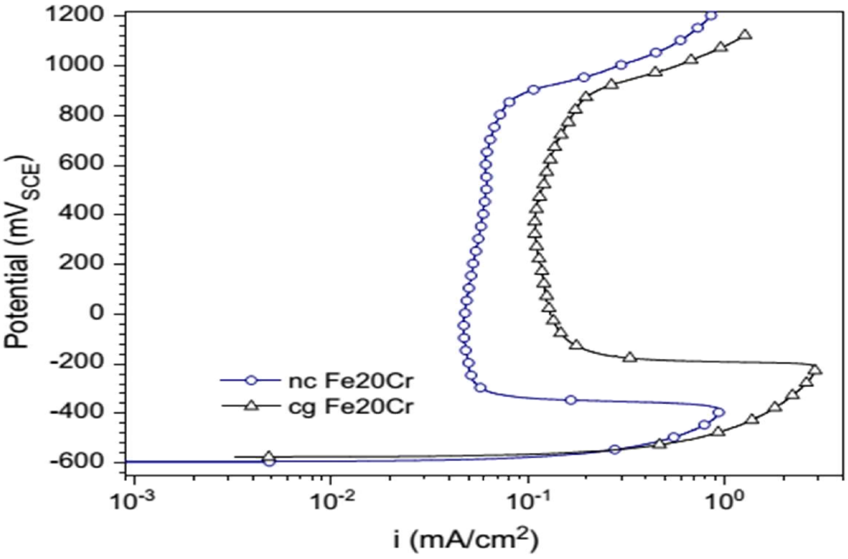

Figure 2.9: PDP curve showing the effect of grain size on the corrosion properties of Fe-20Cr alloys prepared by PM

Velasco et al. [15] prepared 434L with 2% Si by sintering in vacuum and studied the electrochemical behavior at high-temperature and in aqueous solutions. The results showed that, Si not only improves the corrosion resistance of sintered specimen but also the sintered density at lower sintering temperature.

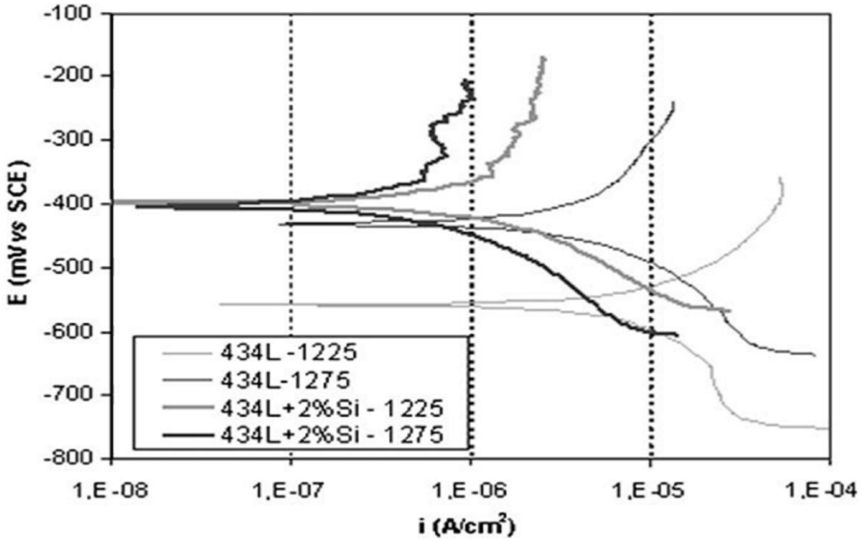

Figure 2.10: Effect of sintering temperature and Si addition on corrosion behavior of 434L alloys

Toor et al. have prepared nano-crystalline Fe-18Cr-2Si alloys by ball milling the pristine elemental powders in a planetary ball [39]. The effect of sintering holding time on the electrochemical properties has been studied in different solutions with different techniques. The results showed that, with the increase in densification, both mechanical and electrochemical properties increased.

2.7. Advanced electrochemical techniques for corrosion testing of SSs

Advance electrochemical technique like electrochemical impedance spectroscopy has been used by researchers to study the corrosion behavior of cast as well as PM steels. EIS use Nyquist and Bode plots illustrate the corrosion behavior of the specimen along with different electrical circuits to model the spectrum obtained. In this section, the work done on the electrochemical investigations of sintered steels by EIS has been enlisted.

2.7.1. Electrochemical Impedance Spectroscopy (EIS) technique

Bautista et.al [40] developed two different types of SSs with AISI 409LNb & 434L powders and sinter at three different temperatures (1225, 1250 and 1275 °C) in vacuum. They studied the effect of sintering temperature on the electrochemical behavior of these 6 alloys with PDP and EIS techniques in 0.1M Na_2SO_4. Typical Bode plot (Fig. 2.11) has been drawn to show the effect of sintering temperature on the corrosion resistance of sintered specimens. They deduced that, with the increase in the sintering temperature, the corrosion resistance increases and reason being is the increase in density with the increase in sintering temperature.

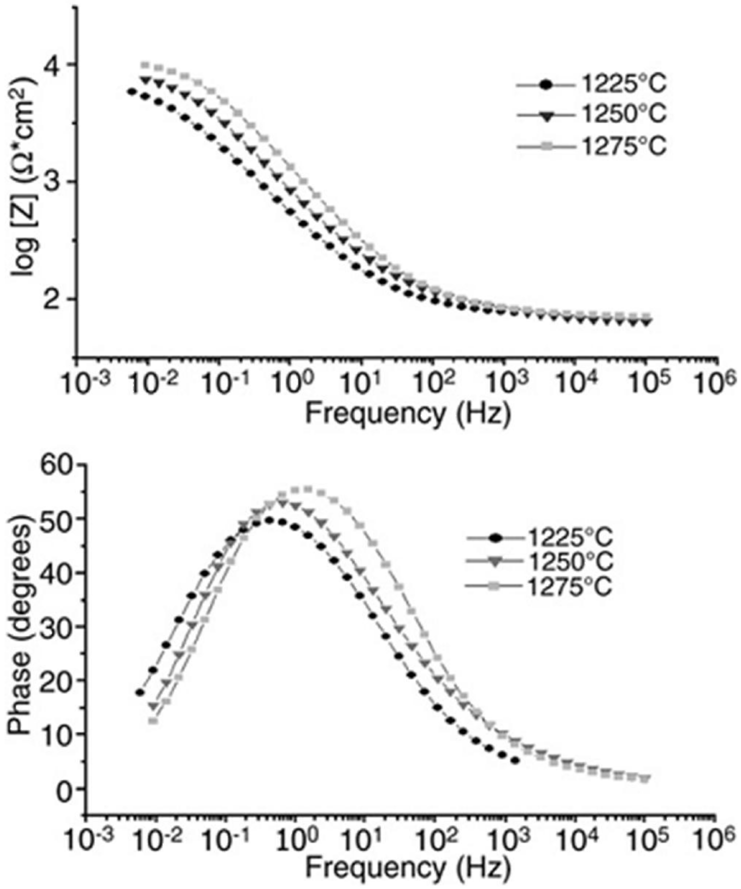

Figure 2.11: Bode plot showing the effect of sintering temperature on the corrosion behavior of 409LNb steels

Wallinder et al. [41] have studied the effect of surface finish, passivation and ageing on the corrosion properties of 205LVM stainless steels and deduced that, the samples with smoother surface finish exhibits higher corrosion resistance.

Hamdy et al. [42] investigated the corrosion behavior effect of Nb of austenitic stainless steels by EIS in 3.5%NaCl and draw a Nyquist plot (Fig. 2.12) showing that the sample having higher Nb content exhibit better corrosion resistance.

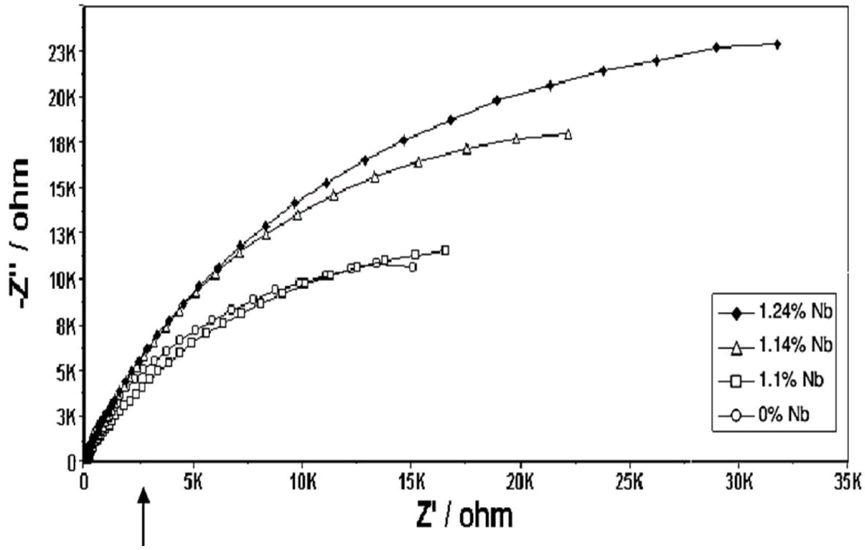

Figure 2.12: EIS spectra comparing the effect of Nb content on the corrosion behavior of austenitic stainless steels

Pan et al. [43] studied the effect of high temperature oxidation of S30403, S30815 and S44600 SSs by EIS in 0.1M Na_2SO_4 solution and used two layer model to simulate the data. The results reveal that the oxide on S30403 grows and becomes defective while the oxide on S44600 thickens rapidly and retains its protective ability for a relatively long time and the oxide on S30815 remains thin and resistive.

Abreu et al. [44] studied the effect immersion time on the formation of oxide layer on three different SSs by drawing Nyquist plot. Fig. 2.13 shows a typical Nyquist plot of as received AISI 316 sample without any immersion while Fig. 2.14 illustrates the effect of immersion.

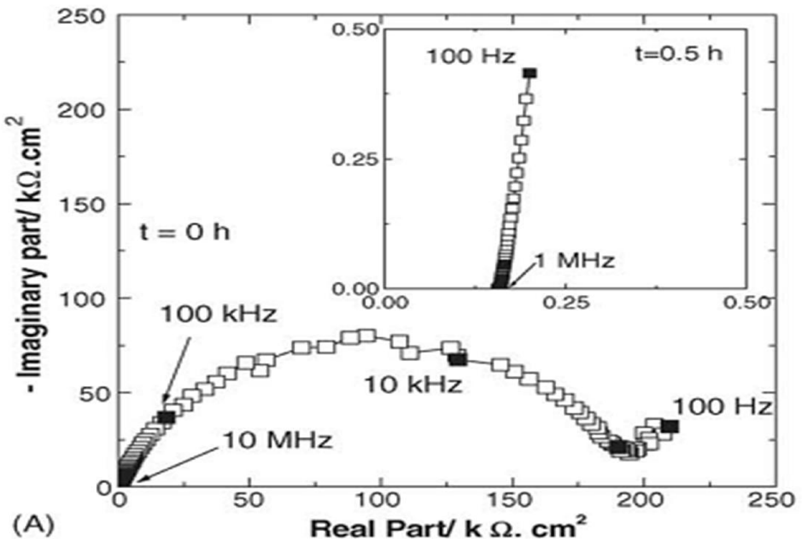

Figure 2.13: EIS spectra for as received AISI 316 SSs

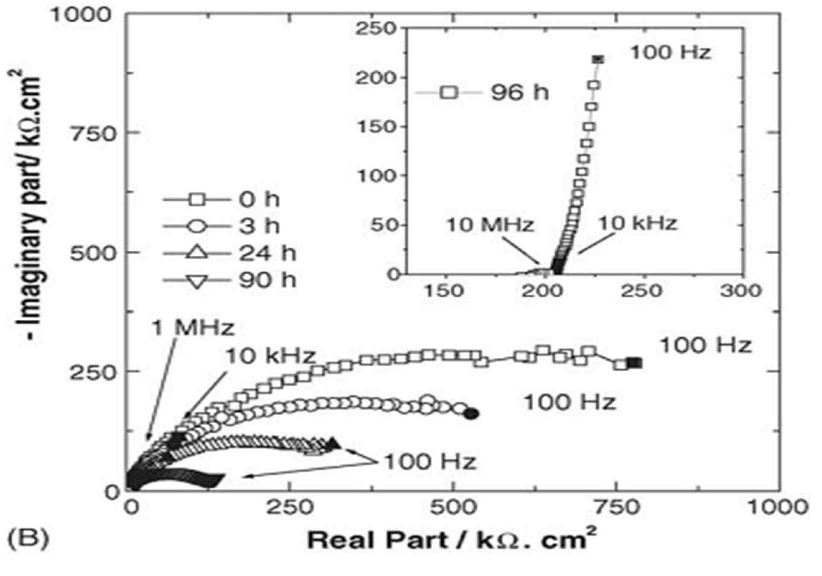

Figure 2.14: EIS spectra comparing the effect of immersion time on corrosion behavior of AISI 316 SSs

M.A. Ameer et al [45] used EIS to investigated the effect of Mo in austenitic stainless steels in varying concentration of Cl^{-1} and SO^{4-} ions. Nyquist plots (Fig. 2.15 and 2.16) drawn show that, as the concentration of Cl^{-1} ions increases, corrosion resistance of specimen decreases.

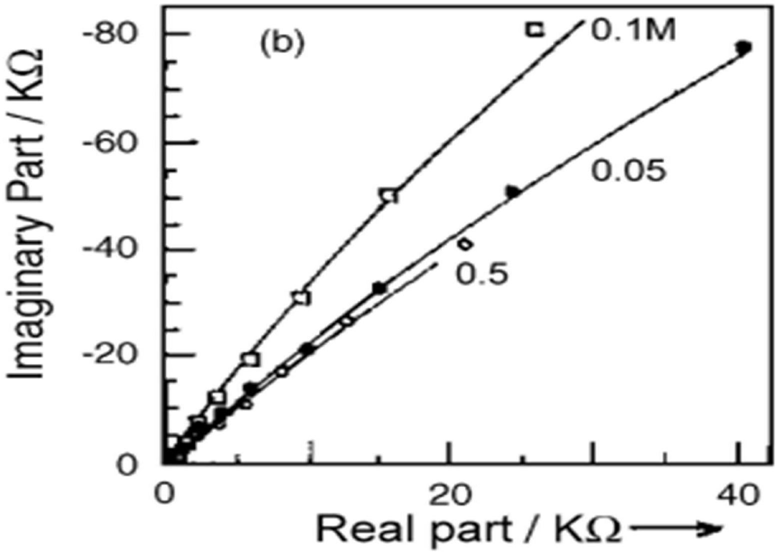

Figure 2.15: Effect of Cl-ion concentration on the corrosion behavior of Mo containing austenitic stainless steels

Motivation

Corrosion is a serious global industrial problem and billions of dollars are spent annually due to damages incurred by corrosion in oil & gas, petrochemical and power generation industries. Proper selection of materials and proper investigation can predict corrosion and cut down these losses. Ferritic, Austenitic, and Duplex SSs are the most commonly used ferrous alloys and these alloys have some serious issues of corrosion that led them to catastrophic failures. The most common corrosion issues with these alloys are localized corrosion (pitting and crevice corrosion) and stress corrosion cracking in Cl^{-1} concentrated solutions.

Production of new grades and especially nano-crystalline structured SSs can solve these issues but corrosion properties of these materials need to be studied very deeply. Among other manufacturing techniques, powder metallurgy (PM) has been proven to be the best technique to manufacture nano-structured SSs. Some typical applications of PM SSs include automotive rearview mirror brackets, automotive flanges and sensors of exhaust systems, antilock brake system sensors, stainless steel filters and other porous stainless steels. The off-shore applications of PM SSs are increasing day by day ranging from self-lubricated bearings, anticorrosion painting etc. So, the electrochemical properties of these SSs need to be investigated by the use of advance electrochemical techniques like EIS.

Hence, PM SSs have been selected for in-depth electrochemical investigations with the help of state of the art techniques like EIS. Previously there has been extensive research carried out to evaluate their corrosion behavior by some simple techniques.

Objective

The purpose of this study is to develop Ferritic [$Fe_{(82-x)}$-Cr_{18}-Si_x $(x = 0, 1, 2, 3)$] and Austenitic [$Fe_{(73-x)}$-Cr_{18}-Ni -Si_x $(x = 0, 1, 2, 3)$] SSs by using planetary ball mill and sintered by spark plasma sintering. To achieve maximum densification and ultimately higher corrosion resistance, sintering process parameters (sintering temperature, holding time, applied pressure and heating rate) need to be optimized. FE-SEM, XRD, FE-TEM will be used to characterize the alloy powder as well as sintered specimens. Different electrochemical investigation techniques like Potentiodynamic polarization (PDP), linear polarization resistance (LPR) and electrochemical impedance spectroscopy (EIS) will be used to investigate the electrochemical properties of alloys. Effect of sintering parameters on the electrochemical properties of the alloys as well as samples having different wt. % Si will be investigated in both 0.2M NaCl and 0.5M H_2SO_4 solutions at room temperature. Characterization of passive layer formed on the surface of the alloys in 0.5M H_2SO_4 will be carried out by XPS.

CHAPTER 3

3. MATERIALS AND METHODS

3.1. Raw Materials

The purity and particle size of the powders used as precursors are listed in table 3.1. The powders were bought from Sigma Aldrich.

Table 3.1: Specifications of as received powders

Element	*Purity (%)*	*Particle size(µm)*
Iron	99	Fine
Chromium	99.95	<150
Silicon	99	<44
Nickel	99.9	Fine

3.2. Alloy Preparation by Mechanical alloying (MA)

The pure elemental powders (Fe, Cr, Si, Ni) with purity of > 99.99% were weighed to give the nominal compositions of $Fe_{(82-x)}$-Cr_{18}-Si_x and $Fe_{(73-x)}$-Cr_{18} -Ni_9-Si_x (x = 0, 1, 2, 3). Powders were mechanically alloyed in a planetary ball mill (Fritsch Pulverisette 5, Fig. 3.1) at room temperature (25 °C) for 5, 10, 15, 20, 35, 65, 85, 90 and 100 h. The powder mixtures were ball milled under argon atmosphere in SS vials (250 ml) with 10 mm SSs balls and ball to powder ratio (BPR) was 30:1. The rotational speed was 300 rpm and 3% of Stearic acid was used to avoid cold welding and agglomeration. The milling was interrupted for 30 min after every 1 h to dissipate any kind of thermal energy and to bring the vials at room temperature. The experiments were conducted 2~3 times to confirm the reproducibility of the results.

As received and milled powders were analyzed by X-ray Diffraction (XRD) in an AXSD8 Bruker machine using Cu Kα radiation (λ = 0.1542 nm) at a step size of 0.02°/sec. Morphology of the milled powders was observed using SEM (JEOL JSM-6460). FE-TEM (JEOL, 200 KV) was employed to confirm and evaluate the results obtained by XRD.

Crystallite size and micro-strain calculations were done for the highest diffraction peak using Williamson-Hall equation ($\beta_{hkl} \cos\theta = K\lambda/D + 4\varepsilon\sin\theta$), where β_{hkl} is corrected instrumental broadening, D is the crystallite size, λ is the wavelength of the X-ray source and K is a shape factor (0.9). Lattice parameter (a) of ball milled powder was calculated by determining the d-spacing of highest Bragg's angle peak (110) and then using the equation $a = d*\sqrt{h^2 + k^2 + l^2}$. h, k and l are the miller indices of Bragg's angle.

Figure 3.1: Planetary ball mill used in this study

3.3. Spark Plasma Sintering

Sintering of ball milled $Fe_{(82-x)}$-Cr_{18}-Si_x and $Fe_{(73-x)}$-Cr_{18}-Ni_9-Si_x (x = 0, 1, 2, 3) alloy powder was carried out by using SPS machine, FCT Systeme GmbH (Fig. 3.2). Powders were loaded in an offset manner in a graphite die with upper and lower punches made of graphite (Fig. 3.3). Graphite sheet was used as a lining inside the die and graphite covers were used to separate the powders and punches. Sintering process parameters (temperature, holding time, heating rate and applied pressure) were optimized to obtain the best combination of properties. Optimization was carried out on ***Fe_{80}-Cr_{18}-Si_2*** alloy and the most desirable property was "high densification" because in PM alloys, higher the densification, higher will be the mechanical and electrochemical properties. After sintering process parameter optimization, the rest of the compositions $Fe_{(82-x)}$ -Cr_{18}-Si_x (x = 0, 1, 3) and $Fe_{(73-x)}$-Cr_{18}-Ni_9-Si_x (x = 0, 1, 2, 3) were sintered as per the optimized conditions. Table 2 shows the Sintering process parameters. The color combination in the table is showing the set of experiments done together to verify one parameter.

Figure 3.2: SPS FCT-systeme-GmbH used for sintering in this work

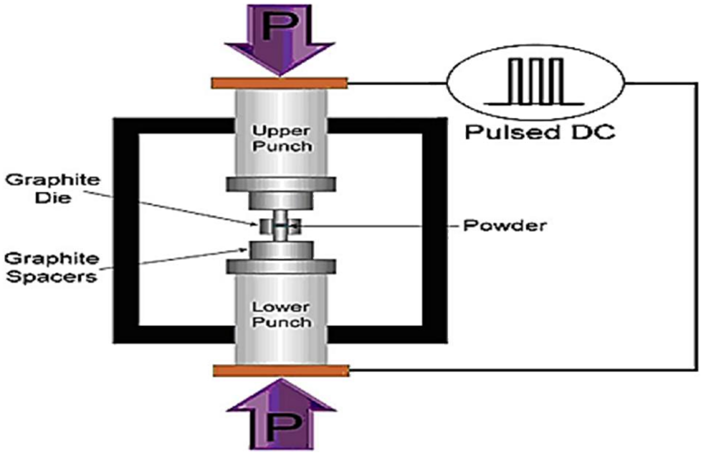

Figure 3.3: Schematic for the offset loading of powders

Table 3.2: SPS process parameter for optimization

Temperature (˚C)	Holding time (min)	Heating rate (degree/min)	Pressure (MPa)
900	10	100	50
1000	10	100	50
1100	10	100	50
1200	10	100	50
1100	5	100	50
1100	15	100	50
1100	15	100	60
1100	15	50	60

3.4. Characterization of sintered specimens

Characterization of sintered specimen includes density measurements, micro-hardness calculations and metallography (SEM/EDX, FE-TEM/SADP, XRD).

Sintered density was measured by Archimedes' principle with the help of density measurement kit provided by Mettler Toledo. After getting the dry and wet weight, actual density was calculated by using:

Dry weight was calculated by a precise weighing machine and wet weight was calculated by suspending the sample in distilled water. Fig. 3.4 shows the schematic of wet weight measurement that was used to calculate sintered density. Densification was then calculated by dividing the actual sintered density by theoretical density of the alloy. Theoretical density was calculated by rule of mixture.

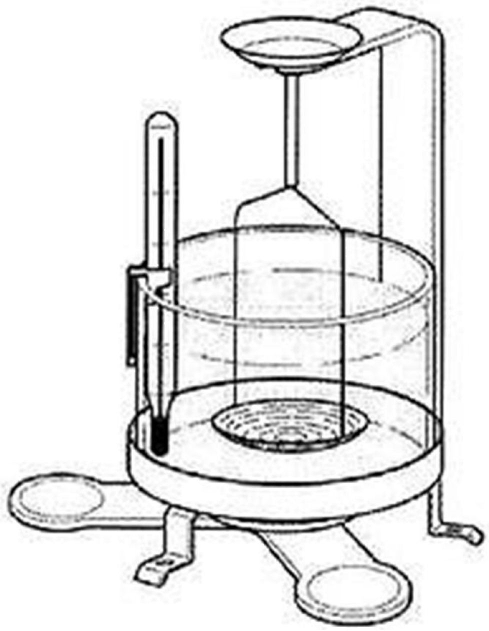

Figure 3.4: Schematic for wet weight calculation to calculate the density of sintered specimen

Before calculation of micro-hardness, the samples were hot mounted in Bakelite using Bhuler hot mounting machine and then ground and polished with alumina suspension. Micro-hardness values were obtained by using Bhuler Micro-Vicker hardness tester equipped with diamond indenter. 500gf (gram-force) was used to load the specimen for 10 sec and the average of 10 readings were reported.

XRD (Bruker D8 advance) was used to study the phase/phases formed after sintering. XRD spectrum were obtained over radiation 20-90° with step size of 0.02°/min. FE-SEM was employed to study the microstructure of the sintered specimens. For micro-structural investigations, specimens were mounted in Bakelite polymer by using Bhuler hot mounting machine. The samples were then coated with gold by using Jeol gold sputter coating machine. Jeol FE-TEM and STEM was employed to study the microstructure of selected sample. Bright field images and SAD pattern were taken to investigate the phases formed after sintering.

3.5. Electrochemical Investigations

The sintered samples were soldered to a copper wire maintaining the electrical connection and then cold mounted in epoxy. The specimens were ground and polished to get a mirror finish surface before conducting electrochemical testing by using Gamry Reference 3000™ Potientiostat. Electrochemical (EC) investigations were carried out in a conventional three electrode electro-chemical cell (Fig. 3.5) having sample as working electrode, graphite rod as counter electrode and saturated calomel electrode (SCE) as reference electrode. The area of the specimen exposed to corrosion at a time was $0.1 cm^2$ and EC investigations have been carried out in chloride solution (0.2M NaCl) and acidic solution (0.5M H_2SO_4) at room temperature. Potentiodynamic polarization (PDP) tests were carried out by swiping the potential from -0.65 to 1.2mV at a scan rate of 0.2mV/sec under deaerated conditions at room temperature. Before experiment, every sample was cathodically polarized at -1.0 V_{SCE} for 180 sec to remove any present oxide film on the surface and open circuit potential was monitored for 5 min. Electrochemical impedance spectroscopy (EIS) tests were carried out by applying a sinusoidal voltage perturbation signal of 10 mV_{rms} with the frequency range of 100000 to 0.2 Hz. Before EIS measurement, potentiostatic film was formed for 30 min under deaerated conditions at room temperature. Linear polarization resistance (LPR) testing was carried out in the potential range of -0.02 to 0.02 mV_{SCE} at scan rate of 0.3mV/sec and sample was cathodically polarized at -1.0 mV_{SCE} for 180 sec and open circuit was monitored for 5 min.

X-ray photoelectron spectroscopy (XPS) was carried out to study the effect of composition of an alloy on the passive layer. Before XPS, a potentiostatic film was formed for 15 min in 0.5M H_2SO_4 solution.

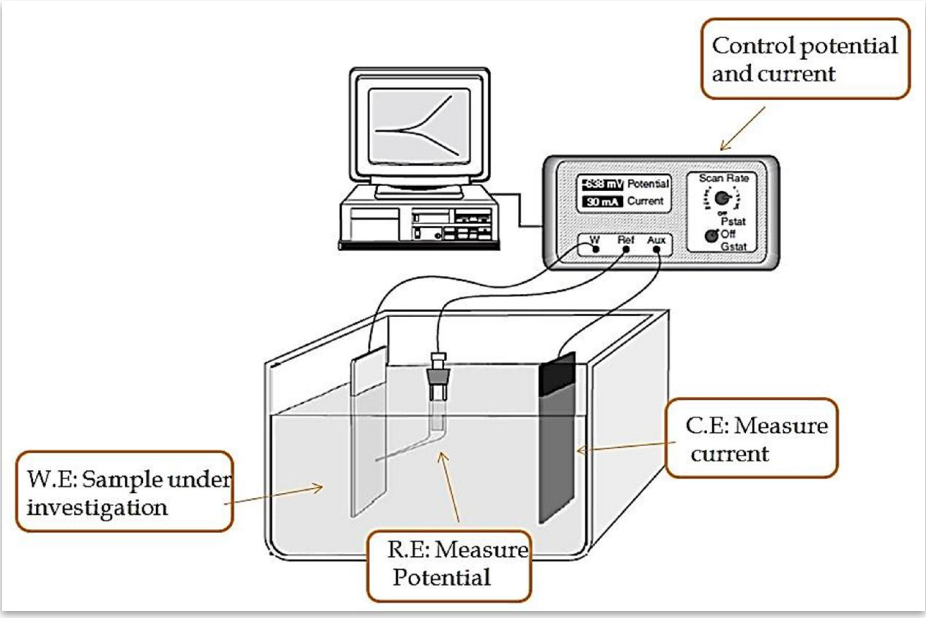

Figure 3.5: Schematic of conventional three electrode system used to carry out the electrochemical investigations

CHAPTER 4

RESULTS AND DISCUSSION

This chapter consists of two sections.

4.1. Development and Characterization of Ferritic stainless steels

- Mechanical alloying of $Fe_{(82-x)}$-Cr_{18} -Si_x (x = 0, 1, 2, 3)
- Spark plasma sintering
- Electrochemical investigations

4.2. Development and Characterization of Austenitic stainless steels

- Mechanical alloying of $Fe_{(73-x)}$-Cr_{18} –Ni_9-Si_x (x = 0, 1, 2, 3)
- Spark plasma sintering
- Electrochemical investigations

4.1. Ferritic Stainless Steels $Fe_{(82-x)}$-Cr_{18} -Si_x (x = 0, 1, 2, 3)

4.1.1. Alloy development by mechanical alloying

4.1.1.1. XRD studies of ball milled powders

XRD of powder specimen milled for 5, 10, 15, 20, 35, 65, 85, 90 and 100 h give clear indication of phase evolution during milling and the phase change in $Fe_{(82-x)}$-Cr_{18}-Si_x (x = 0 & 3 wt.%) have been discussed here. XRD of un-milled powder {Fig. 4.1 a)} show sharp peaks of Fe and Cr while milling resulted in the reduction of peak intensity and considerable broadening. Patil et al. [46] reported that, reduction in the crystallite size and particle refinement due to ball milling is the cause of the broadening in the XRD pattern. It can be seen from the Fig. 4.1 that, after 5 h of milling, Fe (110) peaks shifted toward lower angles (2θ = 44.34°) with little broadening because of solid solution formation of Fe-Cr and Fe-Cr-Si and particle refinement. Milling to 10 h resulted in the decrease in peak intensity and more broadening but XRD pattern of 15 h milled powder showed a broad halo with very low intensity. This type of behavior is attributed to the formation of partial amorphous phase and has been reported by Patil et al. in Fe60Co8Zr10Mo5W2B15 at 20 h of milling [46].

Continued milling of 15 h milled powder to 35 h resulted in the vanishing of Fe (110) peak which is attributed to the formation of amorphous phase. It is well established that with the progression of milling, the long range order of constituent particles is broken down to a short range order because of the formation of different crystal defects like dislocations, vacancies due to severe plastic deformation. Movahedi et al. [47] investigated Fe–Cr–Mo–B–P–Si–C system and observed the formation of saturated solid solution at early stages of milling which later with continued milling transformed to an amorphous phase. Sharma et al. also reported the vanishing of Fe(110) peaks at 10 h of milling due to amorphous phase formation [48]. Suryanarayana have enlisted many instances where the formation of amorphous phase took place due to milling of powders [30,31]. The criteria for the amorphous phase formation during MA of the powders [49] is that there should be a difference in the atomic sizes of the constituent elements (solute and solvent) and produce lattice strain [50]. Egami et al [51] explain the effect of difference in atomic sizes of constituent elements on the glass formability of metals as the lattice strain increases linearly with increasing concentration of solute atoms. When lattice strain reaches a certain value, glassy alloy becomes more energetically favorable as compare to its crystalline counterpart. In simple words, the induce lattice strain destabilizes the crystal lattice and resulting in the amorphous phase formation.

XRD of 65 h milled powder showed that, the powders are still amorphous as there is no peak at all but there is a very low intensity, broad peak after 85 h milling. Milling to 90 h resulted in the reappearance of Fe (110) peak at $2\theta = 44.14°$ which is attributed to the crystallization of amorphous phase. XRD pattern of 100 h milled powder showed a sharp Fe(110) peak at $2\theta = 44.16°$ with considerable broadness due to particle refinement. The same kind of trend has been reported by Patil et al [46] where the crystallization of amorphous phase took place at 50 h. Sharma et al. [48] reported that the amorphous phase formed at 10 h of milling was very stable and it did not crystallized till 40 h of milling when the characteristic Fe(110) peak reappeared and at 50 h there was a sharp peak with considerable broadness. They named this phenomenon as mechanical crystallization [48].

There can be many reasons for the crystallization / mechanical crystallization of amorphous phase during MA but the most important reasons are 1) rise in temperature to a certain level above the crystallization temperature during milling, 2) powder contamination causing the crystalline phase more stable than glassy phase, 3) phenomenon of inverse melting, 4) basic thermodynamic consideration [48]. The trend of solid solution formation leading to amorphous phase and finally recrystallization followed in $Fe_{(82-x)}$-Cr_{18}-Si_x(x = 1 & 2 wt.%) as well.

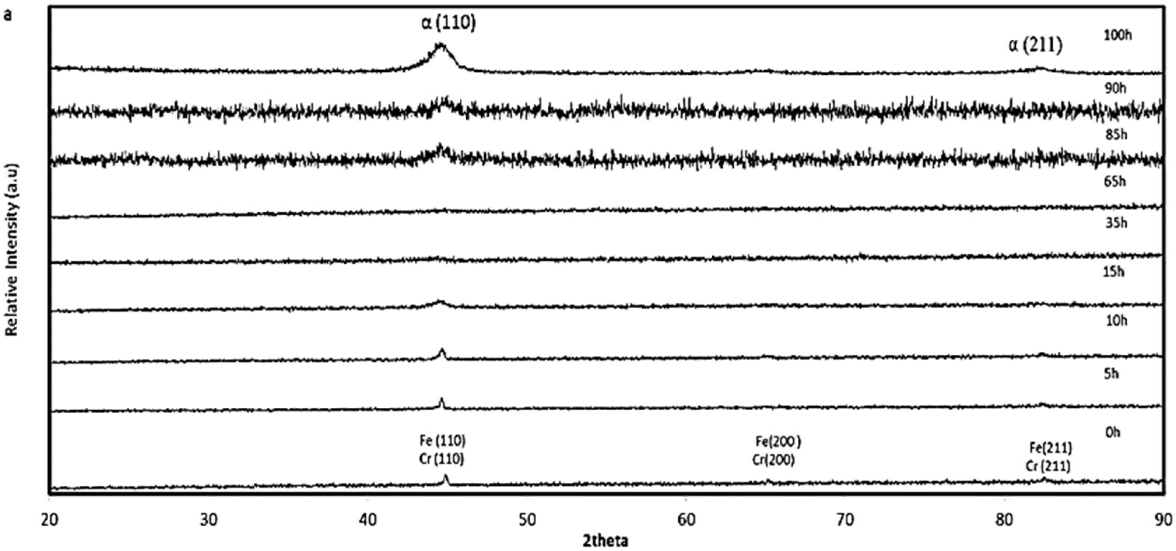

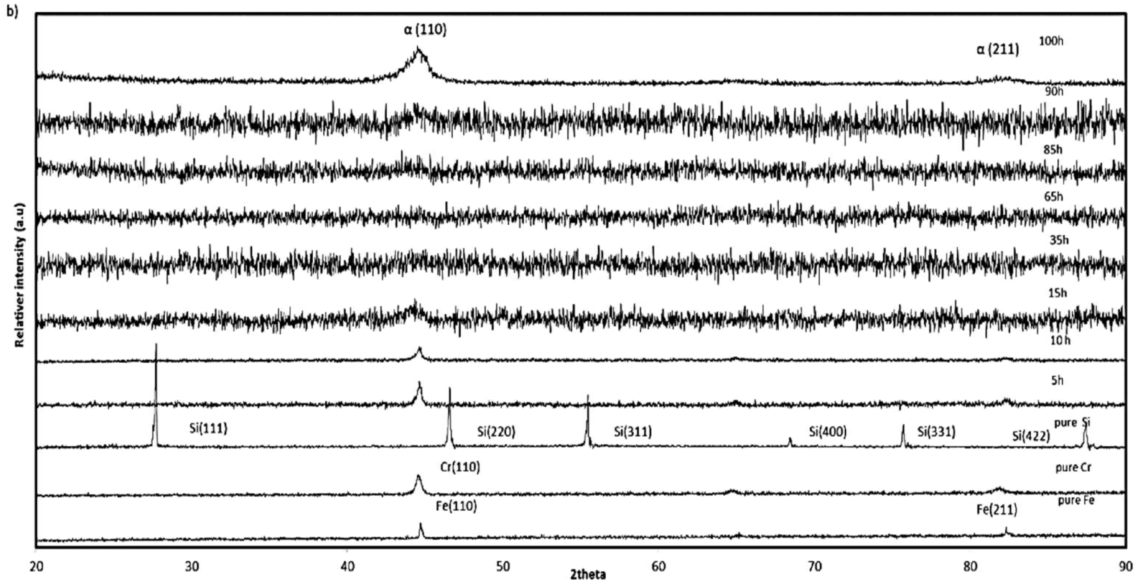

Figure 4.1: XRD of $Fe_{(82-x)}$-Cr_{18} –Si_x (x = 0 & 3) showing the formation of solid solution at 5 h,an amorphous phase at 35 h and mechanical crystallization of the amorphous phase at 100 h of milling

4.1.1.2. TEM of ball milled powders

To confirm the results obtained by XRD, structural analysis of Fe_{79}-Cr_{18}-Si_3 powder milled for 65 h and 100 h was conducted using FE-TEM. Fig. 4.2 (a-d) shows the bright field images and standard area diffraction (SAD) pattern of these two powders respectively. The diffused halo of SAD of powder milled for 65 h (Fig. b) confirms the amorphization of Fe_{79}-Cr_{18}-Si_3 alloy. While the powder milled for 100 h (Fig. 2c) shows the presence of the BCC crystalline phase as was confirmed from the diffraction pattern. These results are in complete agreement with XRD results discussed above.

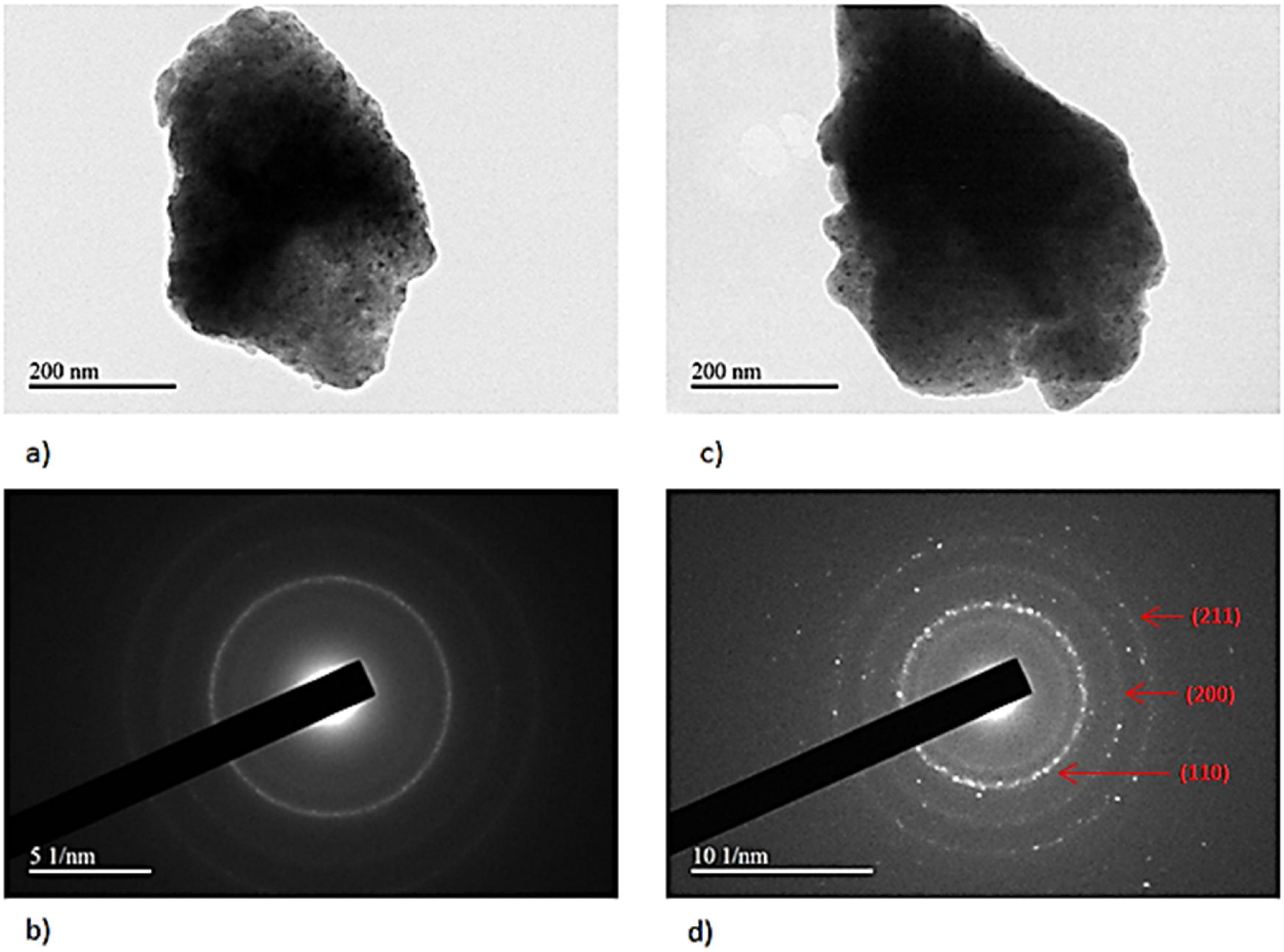

Figure 4.2: FE-TEM bright field images of 65 h (a) and 100 h (c) milled Fe_{79}-Cr_{18}-Si_3 powders, SAD pattern of 65 h (b) and 100 h (d) powders respectively

4.1.1.3. Lattice parameter, crystallite size and lattice strain calculations

The variation of lattice parameter calculated at 0, 5, 10, 15 and 100 h of milling time is shown in Fig. 4.3. It is clear from the Fig that lattice parameter increased continuously up to 5 h of milling and it decreased till 10 h and again increased till 15h and finally started decreasing till 100 h. In other words it can be said that the lattice parameter of the solid solution (at 100 h) was higher than the initial mixture at 0 h of milling.

This variation of lattice parameter can be explained with the help of XRD results of ball milled powders shown in Fig. 4.1 (a & b). As it was observed that, with an increase in milling time Fe(110) slightly shifted towards lower angles indicating the increase in lattice parameter [47]. This increase is attributed to the dissolution of solute atoms (Cr & Si) in the lattice of solvent atom (Fe) forming a solid solution of $Fe_{(82-x)}$-Cr_{18}-Si_x (x = 0, 1, 2, 3). Fig. 4.3 shows that, at 0, 5 and 10 h milling lattice parameter increases drastically and at 15 h the increase is very small in case of 0% Si and with 3% Si lattice parameter decreased. The reason being is, Cr (0.166 nm) is larger than Fe (0.156nm) and its dissolution will drastically change the lattice of Fe_{82} Cr_{18} Si_0. But Si (0.111 nm) is smaller than Fe (0.156), so its dissolution will dilate the lattice parameter of Fe_{79} Cr_{18} Si_3. The lattice parameter of 100 h milled recrystallized powders was lesser as compare to 15 h milled powder. The reason behind the decrease is, recrystallization of amorphous phase at 100 h redistributed the solute atoms in the lattice as reported by Patil et al. [46].

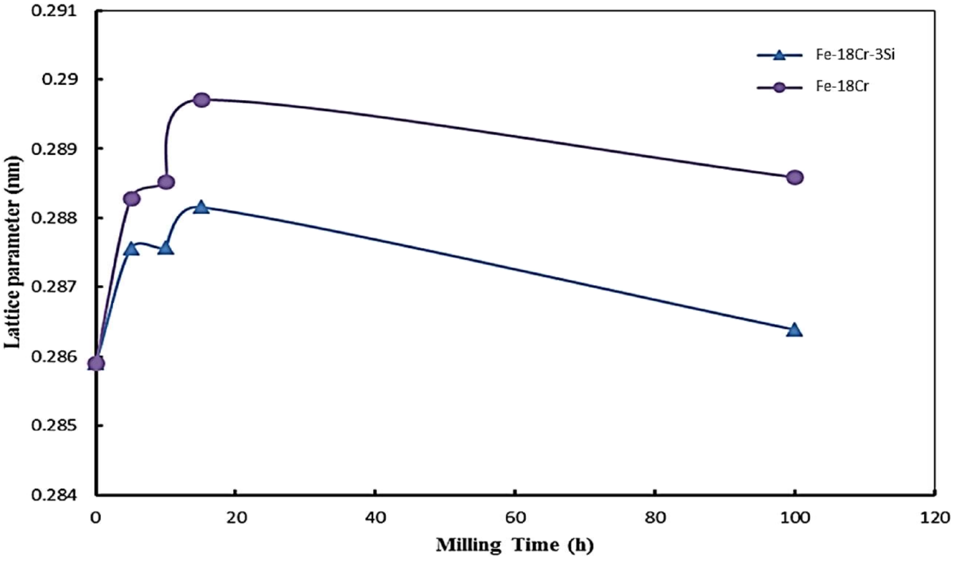

Figure 4.3: Effect of milling time of the lattice parameter variation of $Fe_{(82-x)}$-Cr_{18} -Si_x (x = 0 & 3) alloy powders

Fig. 4.4 illustrates the effect of Si content on lattice parameter variation of $Fe_{(82-x)}$ -Cr_{18} -Si_x (x = 0, 1, 2, 3) alloys formed at 100 h of milling and it can be seen that with the increase in %Si content lattice parameter was decreasing. The effect of %Si content on lattice parameter variation was observed by Yousefi et.al in Fe-Co-Si alloys prepared by ball milling [52]. Lattice parameter calculated from SAD image of 100 h milled powder was very much close to that of calculated by XRD. Lattice parameter of Fe_{79} -Cr_{18} -Si_3 at 100 h calculated by XRD was 0.2878 nm while that calculated by SAD pattern was 0.2877 nm.

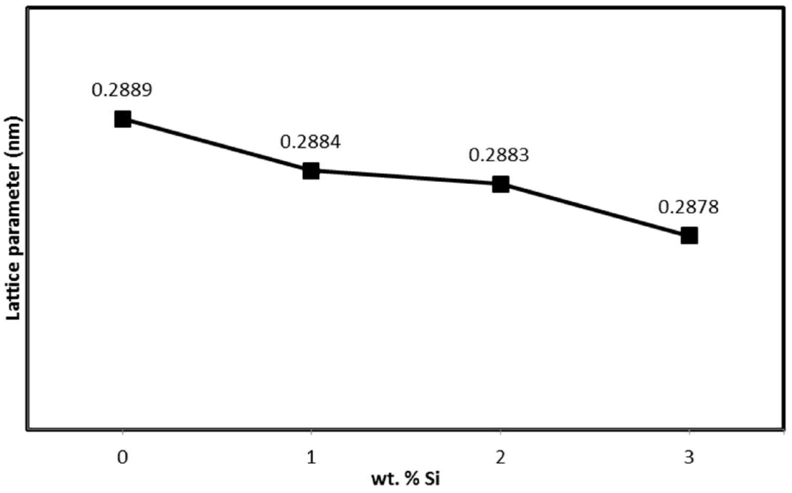

Figure 4.4: Effect of Si content on the lattice parameter of 100 h milled alloy powders

Fig. 4.5 shows the variation of crystallite size at 0, 5, 10, 15 and 100 h milled $Fe_{(82-x)}$ -Cr_{18} -Si_x (x = 0 & 3) alloys calculated by Williamson Hall equation($\beta_{hkl}\cos\theta = K\lambda/D + 4\varepsilon\sin\theta$) [53]. In both cases, the crystallite size was decreasing with an increase in milling time and the mechanism of reduction in crystallite size due to milling has been well explained by Cantor et al. [54]. The reduction of crystallite size was more drastic in case of Fe_{79}-Cr_{18}-Si_3 alloy and the reason behind this drastic decrease is brittleness imparted by Si. Yousfi et al. [52] reported that, powders having more Si content have smaller lattice parameter as compare to that of low Si content powders.

Fig. 4.6 shows effect of wt.% Si content on the crystallite size variation of $Fe_{(82-x)}$-Cr_{18} -Si_x (x = 0, 1, 2, 3) alloys milled at 100 h. Crystallite size was found to be the lowest for Fe_{79} -Cr_{18} -Si_3 as higher Si content contributed towards more brittleness and fragmentation, which ultimately resulted in lowest crystallized size among all alloys.

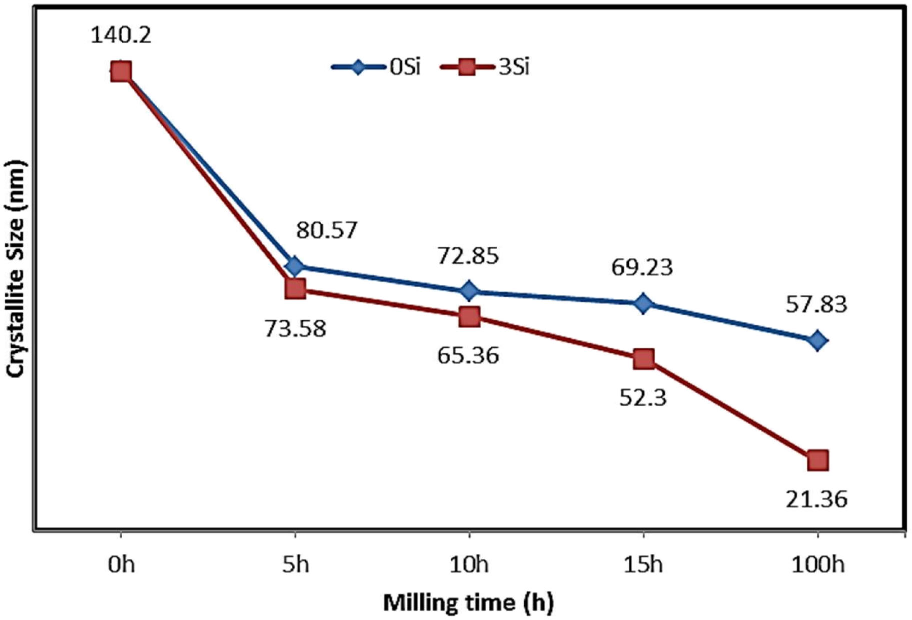

Figure 4.5: Effect of milling time on the crystallite size variation of $Fe_{(82-x)}$-Cr_{18} -Si_x (x = 0 & 3) alloy powders

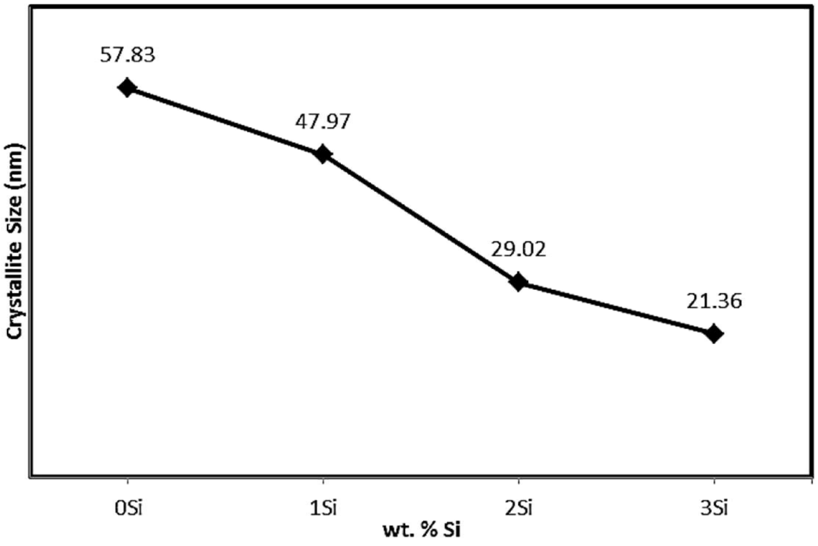

Figure 4.6: Crystallite size variation of $Fe_{(82-x)}$-Cr_{18} -Si_x (x = 0, 1, 2, 3) alloy powders

Fig. 4.7 shows the variation in micro-strain at 0, 5, 10, 15 and 100h milled $Fe_{(82-x)}$-Cr_{18} -Si_x (x = 0 & 3) alloys. It is clear that with an increase in milling time strain generated in milled powders was also increasing. Fig. 4.8 shows the effect of Si content on the micro-stain of 100h milled powders.

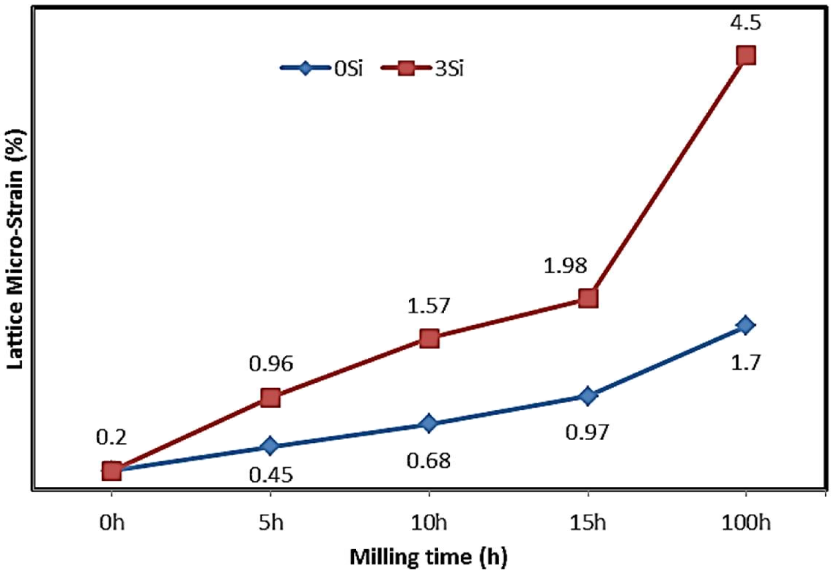

Figure 4.7: Effect of milling time on lattice strain variation of $Fe_{(82-x)}$-Cr_{18} -Si_x (x = 0 & 3) milled alloys

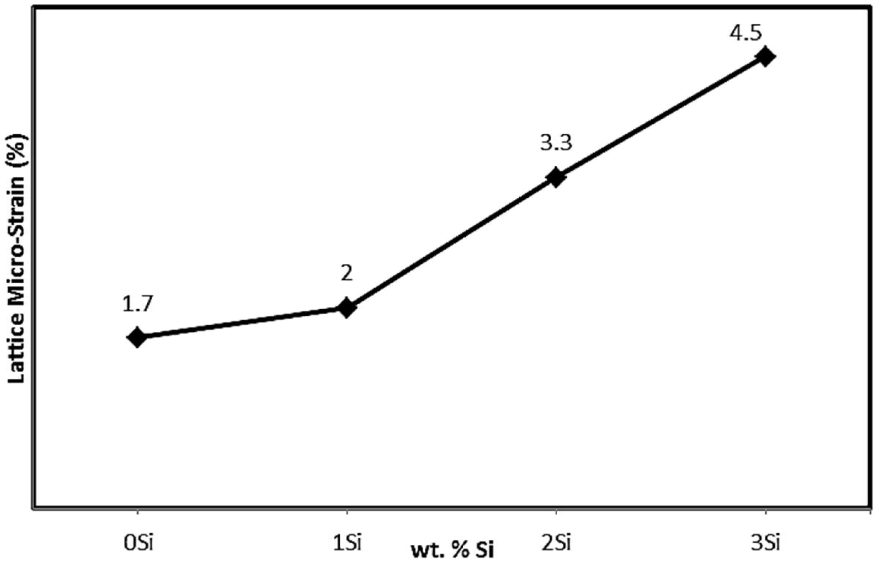

Figure 4.8: Effect of Si content on lattice strain variation in $Fe_{(82-x)}$-Cr_{18} -Si_x (x = 0, 1, 2, 3) alloys milled for 100 h

4.1.1.4. Morphological investigations of ball milled powders

Fig. 4.9 and Fig. 4.10 are showing the scanning electron images of $Fe_{(82-x)}$-Cr_{18} -Si_x (x = 0 & 3) milled powders at 0, 35, 65 and 100 h milling respectively. It is clear in these Figs. that, the particles are getting finer due to prolonged milling and the reason for the decrease in particle size is the hardness or brittleness imparted due to work hardening. It is been reported that, the impingement of balls gives rise to a micro-forging action that deforms the powder particles plastically which results in work hardening and finally leads to fracturing [52]. From Figs. it is clear that the addition of Si contributed in refining the microstructure as the particles of Fe_{79} -Cr_{18}-Si_3 are finer than that of Fe_{82}-Cr_{18}-Si_0. Thus it can be said that, with an increase in Si content, fracture mechanism is more predominant over cold welding.

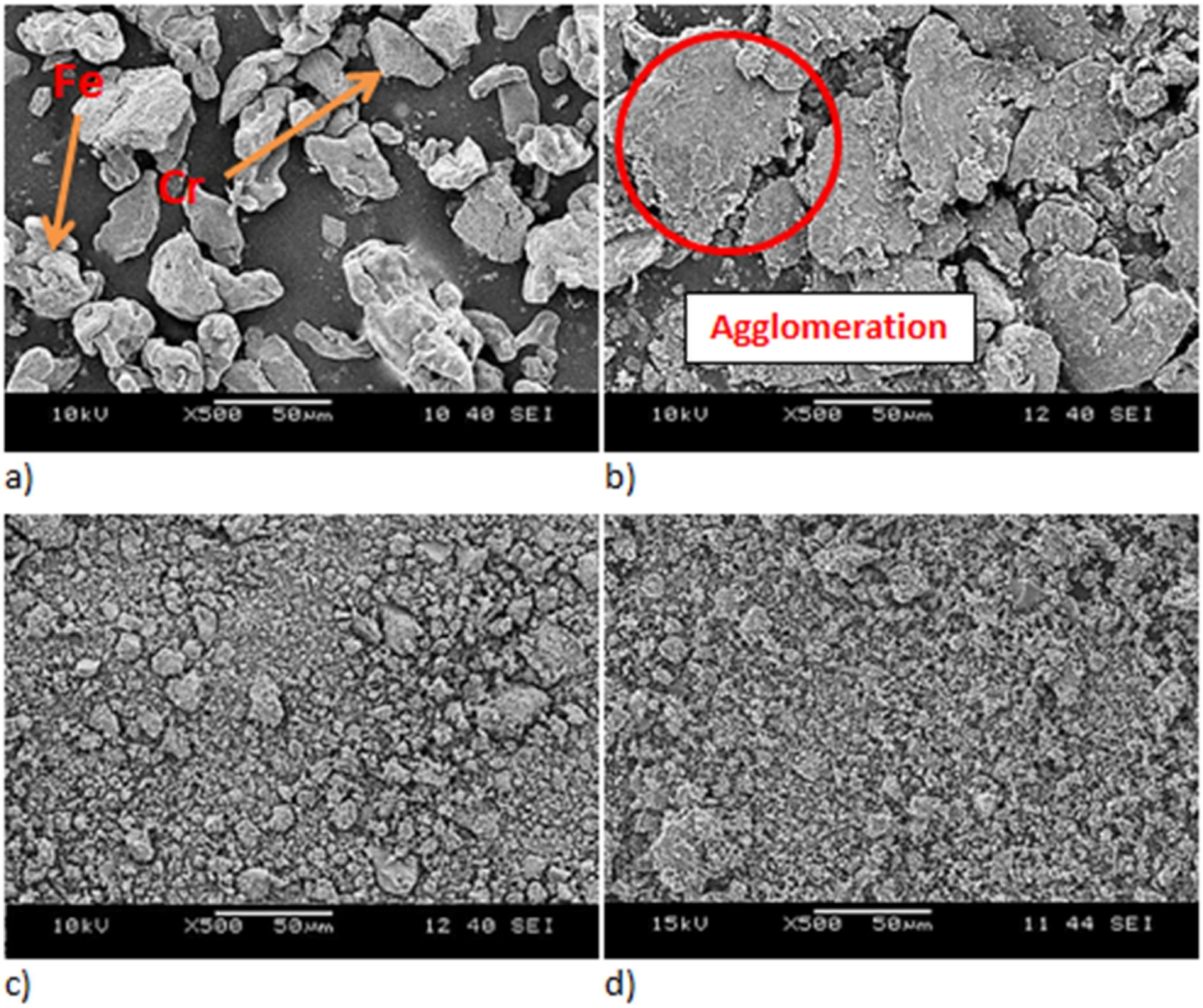

Figure 4.9: SEM images showing the morphology of Fe$_{(82-x)}$ Cr$_{18}$ Si$_x$ (x = 0) milled powders. a)0 h, b) 10 h, c) 65 h, d) 100 h

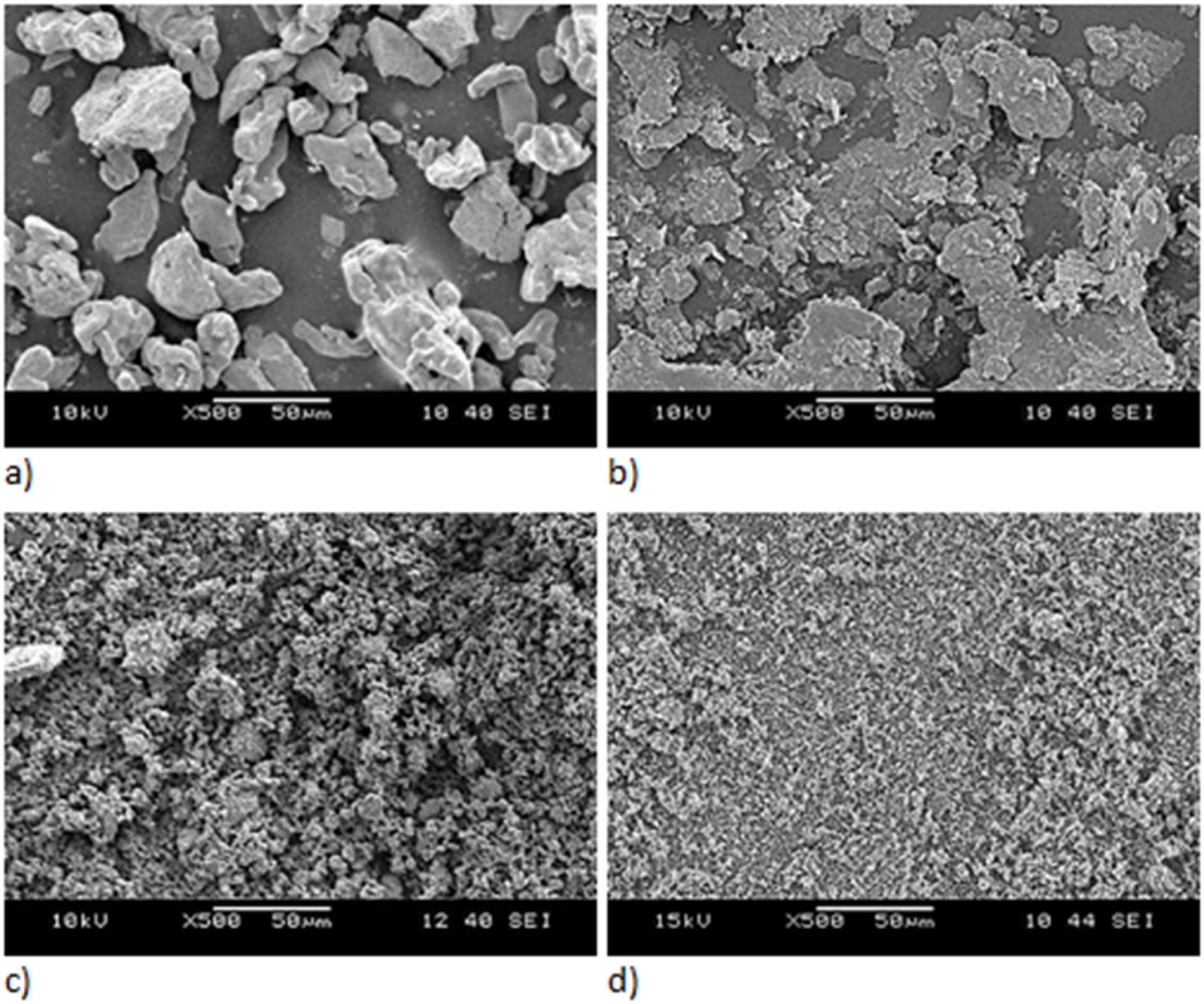

Figure 4.10: SEM images showing the morphology of $Fe_{(82-x)}Cr_{18}Si_x$ (x = 3) milled powders. a)0 h, b) 10 h, c) 65 h, d) 100 h

4.1.2. SPS of ball milled powders

4.1.2.1. SPS parameter optimization on $Fe_{(82-x)}$-Cr_{18} -Si_x (x = 2) milled alloy

In this section of the research, the prime important task was to optimize the sintering process parameters (temperature, holding time, heating rate and pressure) to achieve high densification. Achieving the maximum density was of main concern because electrochemical properties of high density materials are better than that of low density materials.

$Fe_{(82-x)}$-Cr_{18}-Si_x (x = 2) powder milled for 100 h was selected for process parameter optimization and we started by changing sintering temperature (900, 1000 & 1100 °C) by keeping holding time (10 min) applied pressure (50 MPa) and heating rate (50 degree/min) constant. Sintered density was calculated by Archimedes' method and theoretical density was calculated by rule of mixture. Densification was calculated by dividing sintered density by theoretical density. Average of 5 readings of densification with avg. SD of 0.025 has been reported.

The results, of change in sintering temperature on densification have been shown in Fig. 4.11, shows that with an increase in sintering temperature densification increases as well. Maximum densification was achieved at 1100 °C while lowest densification was achieved at 900 °C sintering. Fig also shows that, further increase in sintering temperature (1200 °C) resulted in the decrease in densification because of localized melting. Hussein et al. [55] reported an increase in densification while examining the effect of temperature on densification of Nb-Zr alloys. Zhang et al. [56] also studied the effect of sintering temperature on densification of Fe-0.8%C alloy and reported an increase in the relative density and micro-hardness with increase in sintering temperature. From effect of sintering temperature on densification results, it is concluded that 1100 °C is the optimized sintering temperature.

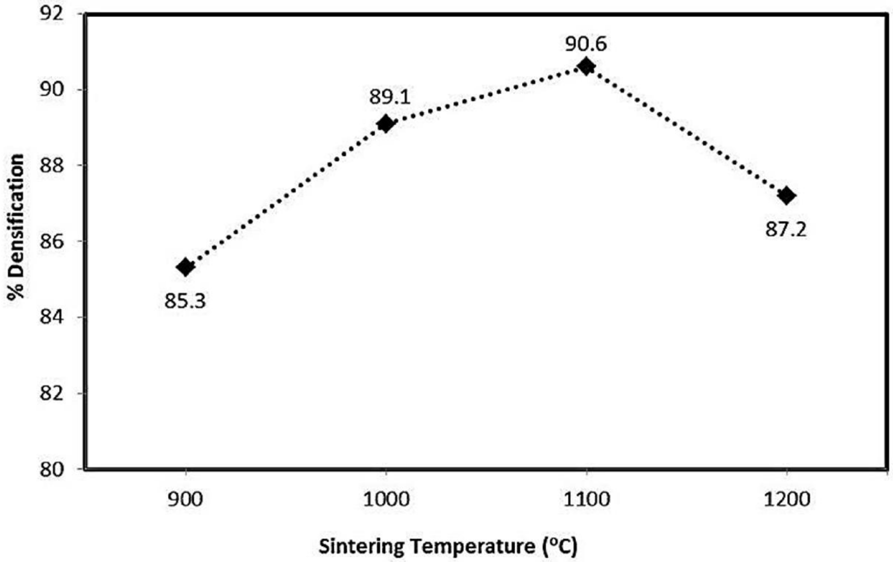

Figure 4.11: Effect of sintering temperature on the densification of $Fe_{(82-x)}$-Cr_{18}-Si_x ($x = 2$) alloys

After optimizing the sintering temperature to 1100 °C, the next step was to optimize the holding time to get maximum densification. $Fe_{(82-x)}$-Cr_{18}-Si_x ($x = 2$) alloy was sintered by changing the holding time (5, 10, 15 & 20 min) and keeping sintering temperature (1100 °C), applied pressure (50 MPa) and heating rate (100 degree/min) constant. The results of effect of holding time on densification have been shown Fig. 4.12 and it can be seen from the Fig that, higher holding time resulted in higher densification. The highest densification was achieved at 15 min of holding time and main reason increase in densification is increased heat flux and longer time given to diffusion leading to reduction in porosity. 20 min of holding resulted in the melting of powders inside the die so we could not get any sample at that holding time. There had been some reported work[57–59] which showed that by increasing the sintering temperature, holding time and pressure applied, high density can be achieved. Cheng et al. [57] reported an increase in density with an increase in sintering holding time, but also highlighted the drawback of grain growth at longer holding times. Zhao et al. [58] while studying ZrB_2–SiC composite, reported an increase in densification and hardness by increase in holding time and pressure. From the results of densification due to varying holding time, it was concluded that 15 min holding is the optimized holding time.

After optimizing sintering temperature (1100 °C) and holding time (15 min), nest step was to optimize applied pressure and heating rate for sintering $Fe_{(82-x)}$-Cr_{18}-Si_x (x = 2) alloy. Alloy powder was sintered by changing applied pressure (50, 60 and 70 MPa) and keeping temperature (1100 °C), holding time (15 min) and heating rate (100 degree/min) constant. The effect of applied pressure on densification has been shown in Fig. 4.13 which illustrate that maximum densification was achieved at 60 MPa. Application of 70 MPa pressure resulted in breaking of graphite die during sintering thus giving no sample for analysis. Finally we changed the heating rate from 100 to 50 degree/min and observed that an increase in applied pressure together with lower heating rates resulted in maximum densification.

Here it is concluded that, best sintering parameters are: 1100 °C sintering temperature, 15 min holding time, 60 MPa of applied pressure and 50 degree/min heating rate.

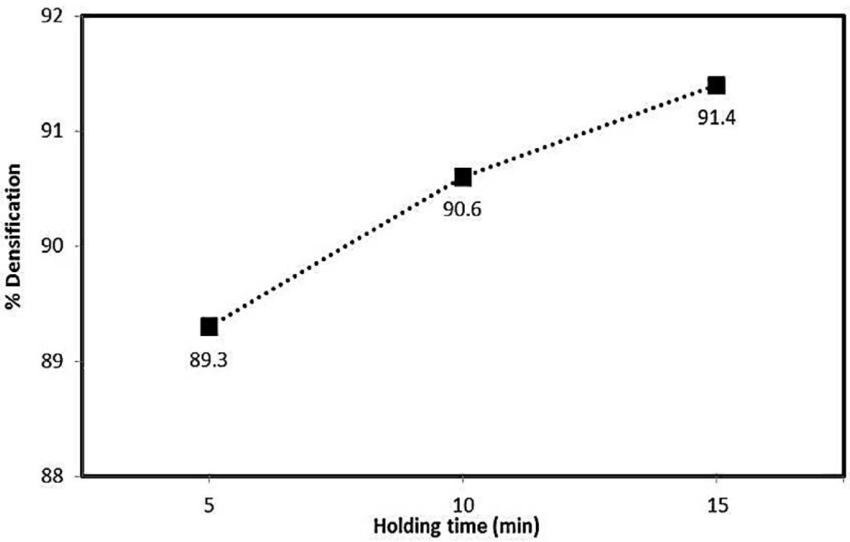

Figure 4.12: Effect of holding time on the densification of $Fe_{(82-x)}$-Cr_{18}-Si_x (x = 2) alloys

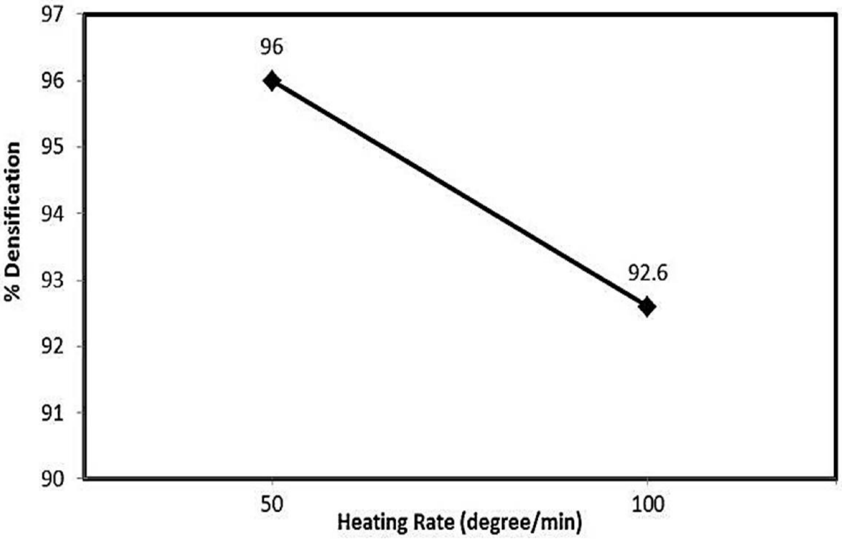

Figure 4.13: Effect of heating rate on the densification of $Fe_{(82-x)}$-Cr_{18}-Si_x (x = 2) alloys

4.1.2.2. SPS of ball milled $Fe_{(82-x)}$-Cr_{18}-Si_x (x = 0, 1, & 3) alloy powders

In this section, the parameters that were optimized in section 4.1.2 were used to synthesize $Fe_{(82-x)}$-Cr_{18}-Si_x (x = 0, 1, 3) alloys. The optimized parameters were 1100 °C temperature, 15 min holding time, 50 degree/min heating rate and 60 MPa applied pressure. Sintered density was calculated by Archimedes' method and theoretical density was calculated by rule of mixture. Densification was calculated by dividing sintered density by theoretical density. Average of 5 readings of densification with avg. SD of 0.025 has been reported.

Fig. 4.14 a) shows the effect of wt. % Si on the densification of the sintered $Fe_{(82-x)}$-Cr_{18}-Si_x (x = 0, 1, 2, 3) alloys and it is clear from the Fig that, as the wt. % Si in the alloy increases densification increases as well. The lowest densification achieved was 94.3% for the alloy having 0% Si and the highest densification (97.6%) was achieved by alloy with 3% Si. Wang et al. reported that samples with Si content have more sintered density as compare to samples without Si [66]. Tsai et al. reported that addition of Si facilitates liquid phase sintering at lower temperature which helps in increasing in the density [67].

Fig. 4.14 b) shows the effect of wt. % Si on the micro-hardness of $Fe_{(82-x)}$-Cr_{18}-Si_x (x = 0, 1, 2, 3) sintered alloys and it is clear from the Fig that, with the addition of Si in the alloy hardness value increases as well. The minimum hardness achieved was 509.6 HV for sample 0% Si and the maximum hardness (7580.6 HV) was achieved for the sample having 3% Si. The results of increase in hardness with the increase in %Si content are in complete agreement with the literature [60, 61]. The reason for the increase in hardness with the Si content is the improvement in density the density of the specimen increases, hardness increases as well. Saravanan et al. also reported the effect of Si in improving the hardness of Ai-Si alloys by lowering the grain size of an alloy [68].

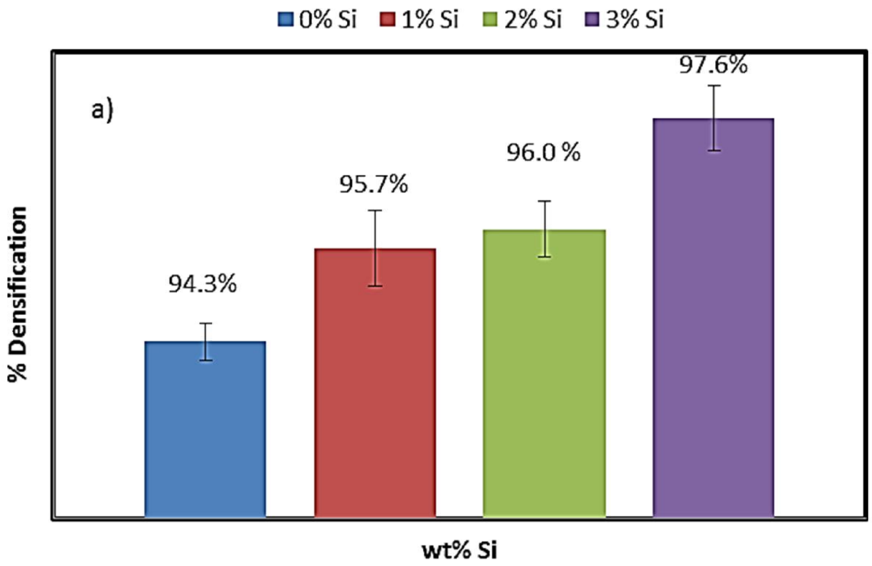

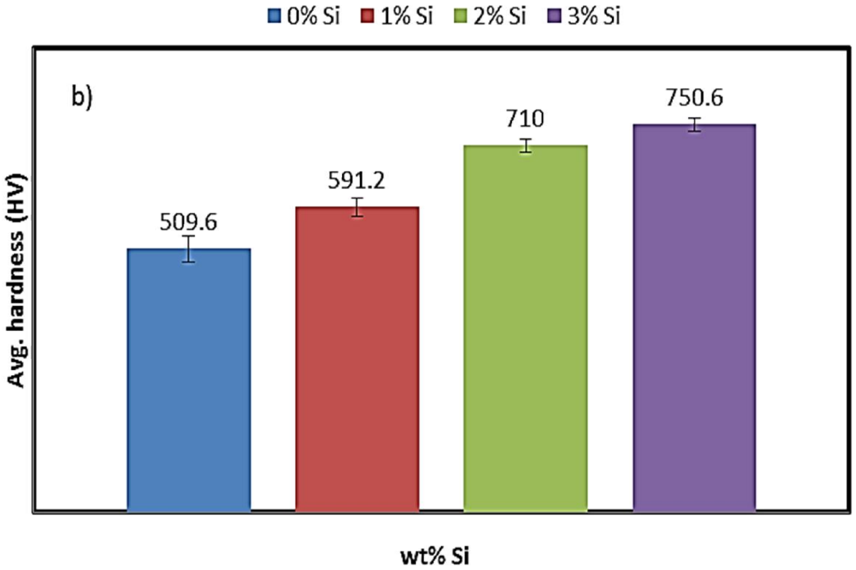

Figure 4.14: Effect of Si content on the a) Densification, b) Micro hardness of $Fe_{(82-x)}$-Cr_{18}-Si_x (x = 0, 1, 2, 3) sintered alloys

4.1.3. Microstructural Investigations of sintered alloys

FE-SEM was used to study the microstructure of samples sintered at different conditions. Fig. 4.15 shows the secondary electron (SE) image of polished surface samples sintered at 900, 1000 and 1100 °C and it is clear that with the increase in sintering temperature, porosity is decreasing. The dark regions in SE-SEM images show the presence of porosity in the samples and these results verify the densification results. The back scattered (BS) images (Fig. 4.16) showing the compositional variation as dark regions are Cr enriched while grey regions are Fe enriched and this has been confirmed by EDX analysis.

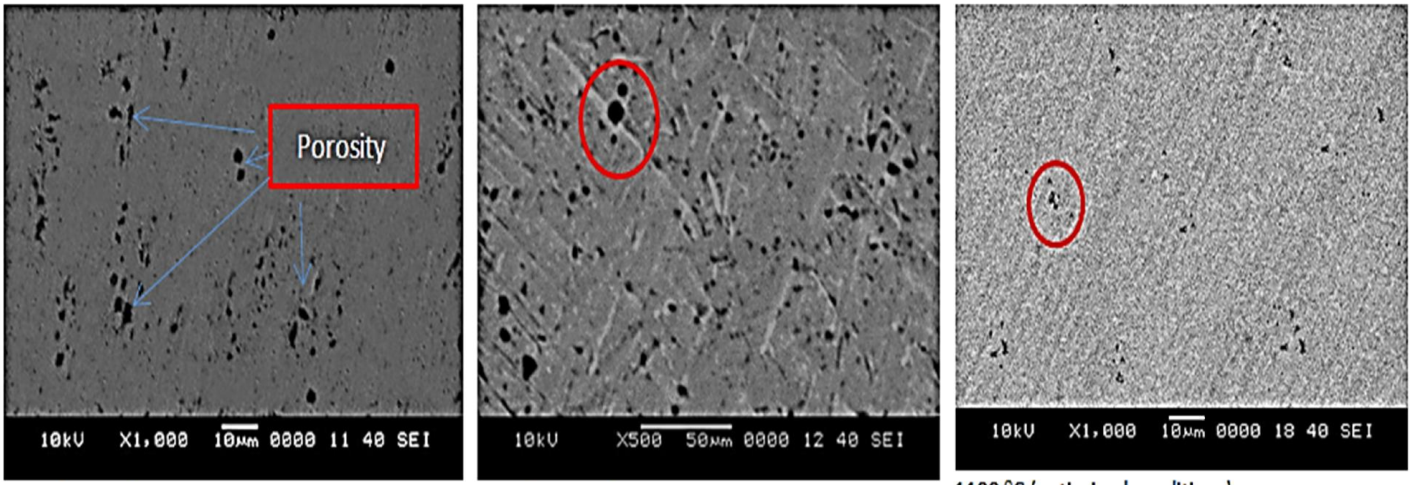

a) 900 °C-10min

b) 1000 °C-10min

1100 °C (optimized conditions)

Figure 4.15: Secondary electron SEM image of polished surface samples sintered at different conditions

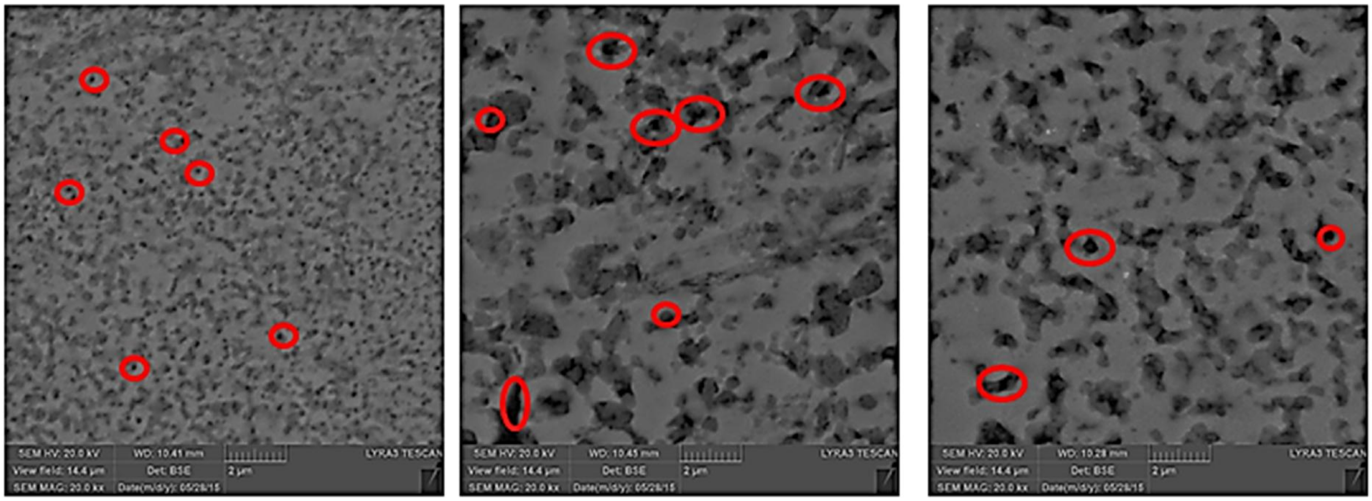

a) 900 °C-10min b) 1000 °C-10min c) 1100 °C-10min

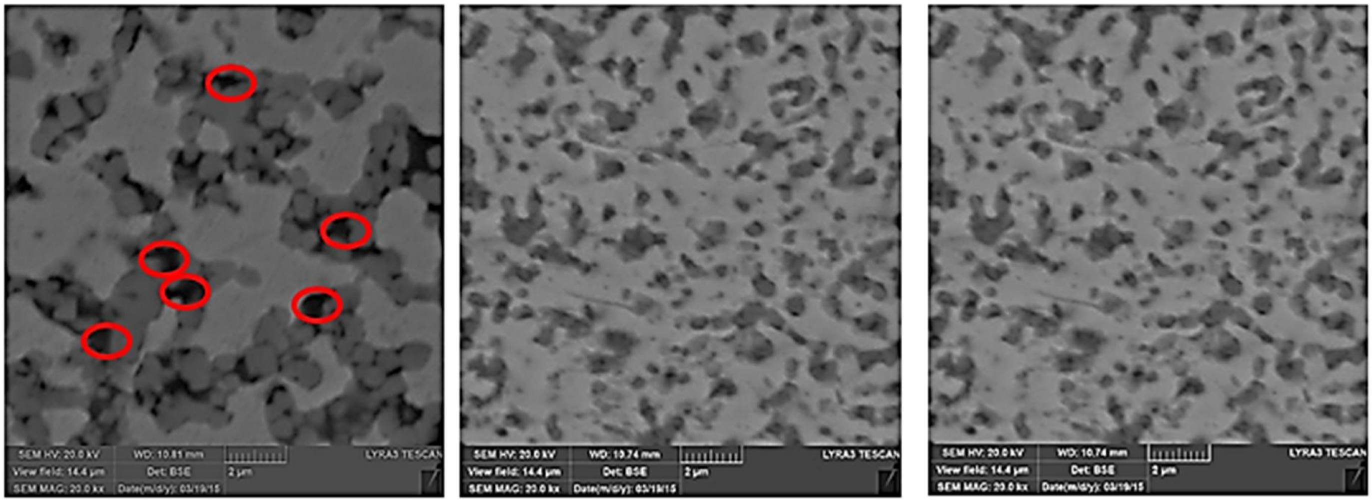

d) 1100 °C-5min e) 1100 °C-10min f) 1100 °C-15min

Figure 4.16: BS-SEM images of $Fe_{(82-x)}$-Cr_{18}-Si_x (x = 2) alloys sintered at different conditions

FE-TEM was used to deeply study the micro-structure of $Fe_{(82-x)}$-Cr_{18}-Si_x (x = 2) sintered at optimized conditions of temperature, holding time, applied pressure and heating rate. Fig. 4.17 a) shows the BSE image where the grey and black contrast is showing that there is compositional difference between these regions. The EDX results showed that, the black regions are slightly Cr enriched and grey regions are Fe enriched. The HAADF STEM image in Fig. 4.17 b) clearly resolves the image and showed that, these dark regions have the size of about 25 nm and EDX results (inset) verified that, these dark regions are rich in Cr and grey regions are rich in Fe. BF-FE-TEM image shown in c) shows that, these dark regions have a microstructure of martensitic laths and the possible reasons for formation of martensitic laths are a) Carbon intake from SPS Die and punches, b) Cr depletion in the matrix due to formation of Cr rich precipitates and c) very fast cooling rate induced in SPS cycle. Auger et.al [60] has reported the formation of these Cr rich phases in $Fe_{14}Cr$ SPS alloy and given the reasons the formation of these precipitates in the Fe rich matrix. The inset of Fig. c) revealed that, their crystalline structure was M_2O_3 (M=Cr) which correspond to Corundum. Fig. 4.14 d) shows that the microstructure of the alloy has equiaxed grains with un-textured BCC structure shown in the inset of Fig. 4.17 d). EDX analysis through STEM (Fig. 4.18) confirmed that, dark regions have higher Cr percentage with huge amount of oxygen making them Cr-oxide and grey regions are lean in Cr.

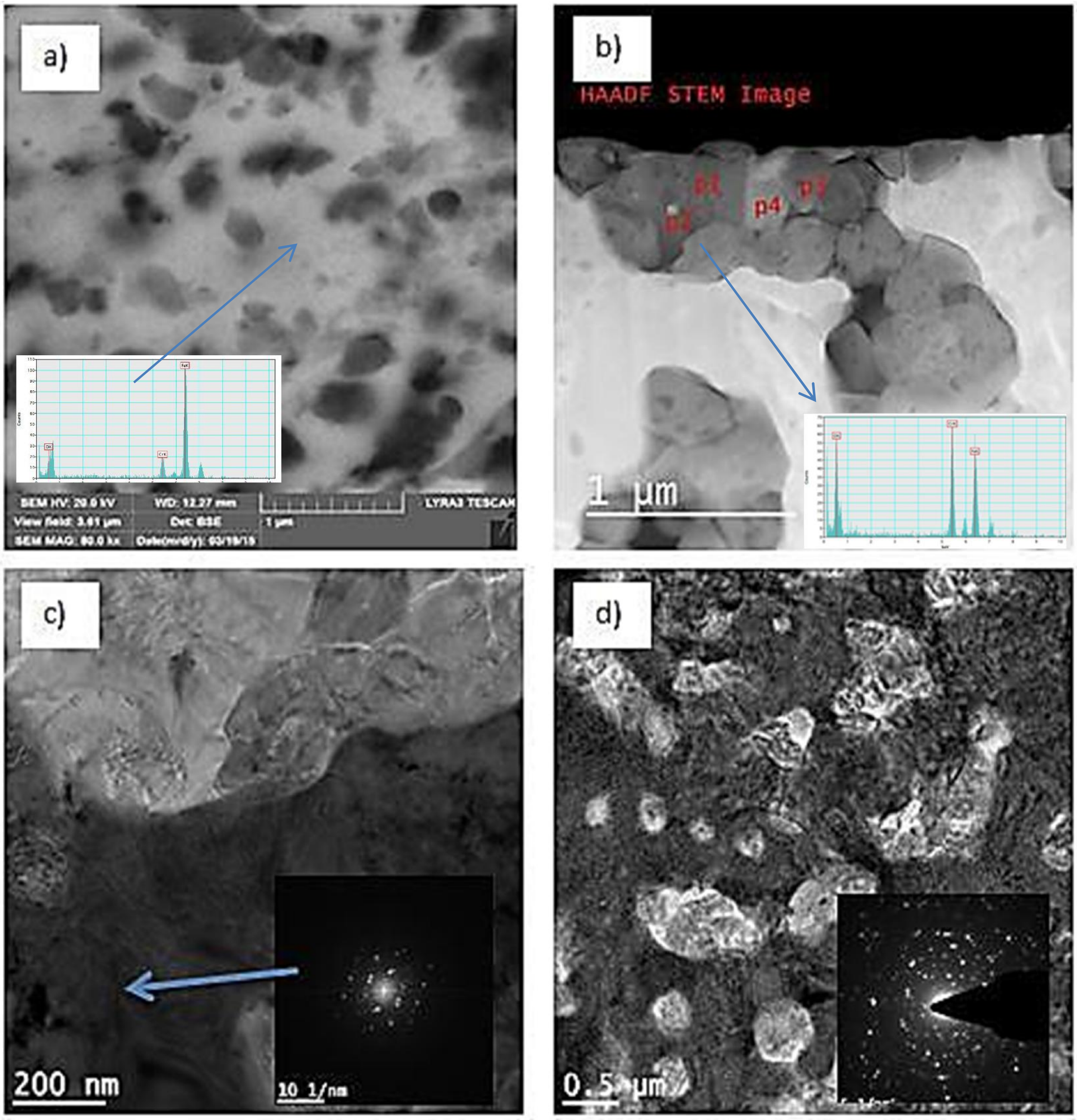

Figure 4.17: Microstructure of $Fe_{18}Cr_2Si$ alloy. a) BSE-SEM images showing the compositional contrast. b) HAADF STEM image revealing the Cr-rich precipitate inside Fe rich matrix. c) BF-TEM image showing the lath like structure of Cr-rich precipitates. d) BF-TEM image showing the equiaxed grains with the inset showing untextured BCC phase

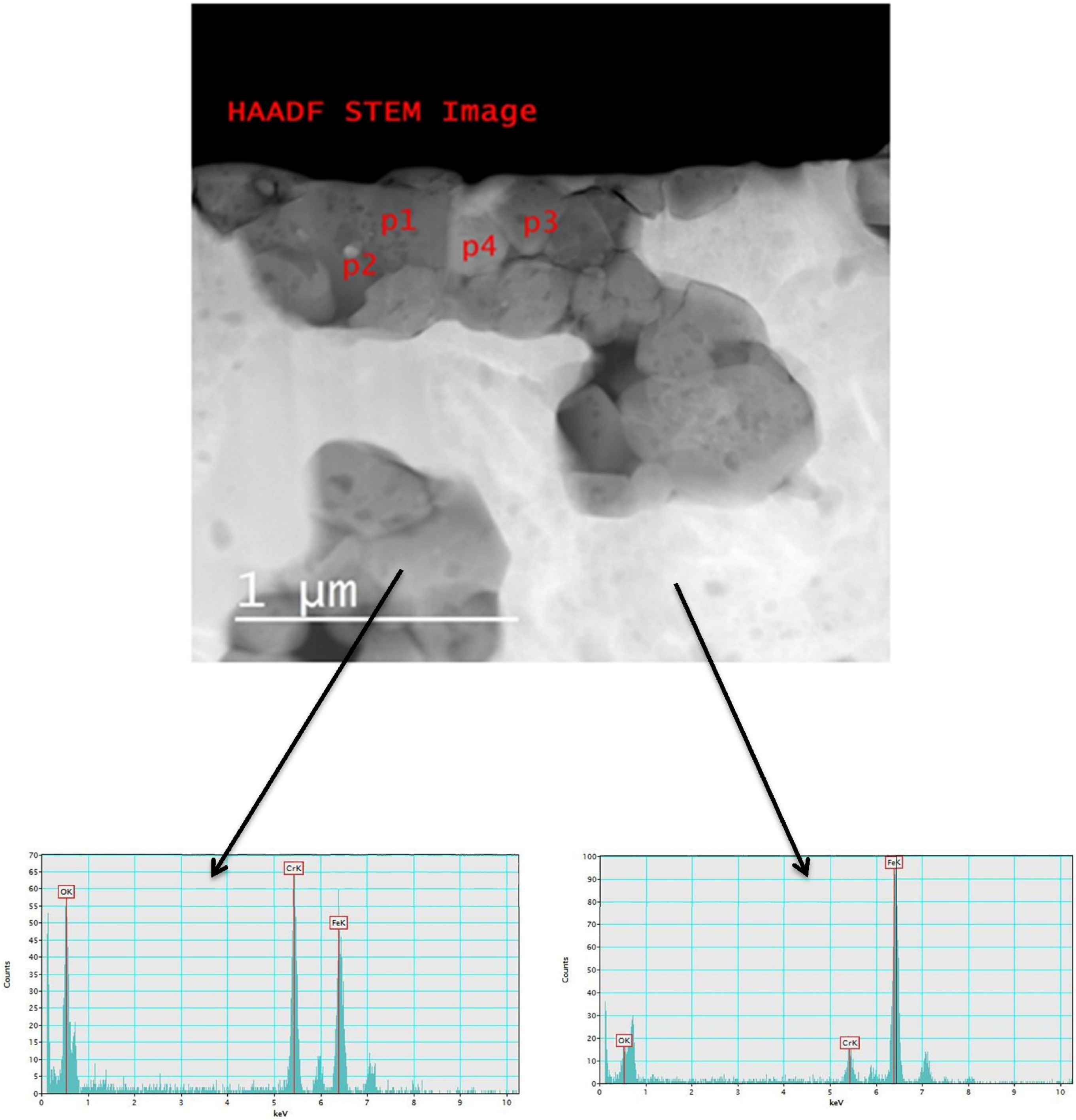

Figure 4.18: EDX analysis of Fe$_{(82-x)}$-Cr$_{18}$-Si$_x$ (x = 2) sintered alloy, Dark regions are Cr enriched while grey regions are Fe enriched.

4.1.4. Electrochemical Investigations

In this part of the research, we have investigated the electrochemical (EC) properties of $Fe_{(82-x)}$-Cr_{18}-Si_x (x = 2) samples prepared during sintering process parameter optimization as well as samples with varying wt. % Si i.e. $Fe_{(82-x)}$-Cr_{18}-Si_x (x = 0, 1, 2, 3). EC properties of samples sintered at different sintering temperature, holding time were investigated by different techniques like PDP, LPR and EIS in 0.2M NaCl and 0.5M H_2SO_4 solutions. A conventional three electrode cell was used to conduct corrosion testing in which graphite rod was used as counter electrode, SCE as reference and sintered sample was acting as working electrode.

4.1.4.1. Effect of sintering conditions on electrochemical properties of $Fe_{(82-x)}$-Cr_{18}-Si_x (x = 2) sintered alloys

4.1.4.1.1. Potentiodynamic Polarization tests (PDP)

Potentiodynamic polarization tests were conducted at -0.65 to 1.2 mV_{SCE} with the scan rate of 0.05mV/sec, under deaerated environment at room temperature.

Fig. 4.19 (a & b) shows PDP response of $Fe_{(82-x)}$-Cr_{18}-Si_x (x = 2) alloy in 0.2M NaCl and 0.5M H_2SO_4 solutions at room temperature. Based on densification values (section 4.1.3), we know that maximum densification was achieved at 1100 °C, 10 min holding and 100 degree/min heating rate with 50 MPa of applied pressure . So it was expected that the specimen sintered at 1100 °C will have high corrosion resistance because of less porosity as compared to other two samples (sintered at 900 and 1000°C). Guo et al. [61] has investigated the effect of sintering temperature on the corrosion resistance of Ti-24Nb-4Zr-

7.9Sn alloy and reported that alloys with lower density (sintered at low temperature) has lower corrosion resistance and vice versa. This lower corrosion resistance is due to more porous/less dense structure, when sintered at low temperature. It is very well known that porosity in sintered samples will allow the corrosion medium stagnation in pores, which will lead to crevice corrosion. High density materials have less interconnected porosity and there are lesser chances for electrolyte to penetration into such interconnected pores and cause corrosion. On the other hand, high porosity samples will have less corrosion resistance due to open interconnected porosity. So it is clear from Fig. that the specimen sintered at 1100 °C exhibited the highest corrosion resistance in terms of pitting potential (Epit), passive current density (i_p) and corrosion potential (Ecorr). The sample sintered at 1100 °C has an Ecorr value of -533.4 and -340.1 mV_{SCE} in 0.2M NaCl and 0.5M H_2SO_4 respectively. Fig. 4.19 shows that, the sample sintered at 900 °C does not exhibit a stable passive film and the reason for the unstable passive film is low density at 900 °C as compare to density at 1100 °C. Ecorr value of sample sintered at 900°C is -549.7 and -505.0 mV_{SCE} in 0.2M NaCl and 0.5M H_2SO_4 respectively which is lower than that of sample sintered at 1100 °C. Pitting potential (Epit), is an important parameter for the investigation of localized corrosion resistance of passive materials. The sample sintered at 1100 °C exhibit highest Epit value of -454.8 and 241.5 mV_{SCE} in 0.2M NaCl and 0.5M H_2SO_4 respectively which means it is the most resistant to localized corrosion under these conditions. Similarly if we compare the passive current density of three samples at

-480 and -170 mV_{SCE} in 0.2M NaCl and 0.5M H_2SO_4 respectively, it is the lowest for sample sintered at 1100 °C .The lowest passive current density means, sample sintered at 1100 °C has more protective oxide film, which is able to protect the sample from corrosion under these conditions. The results reported in this study are in complete agreement with the literature. Hussein et.al [55] investigated the effect of sintering parameters on the corrosion of Nb-Zr alloys prepared by MA and sintered by SPS. They reported that, the sample sintered at higher sintering temperatures exhibit a stable passive film while the sample sintered at lower sintering temperature does not exhibit a stable passive film. Bautista et.al investigated the role of sintering temperature on density and the corrosion properties and reported that sample having higher density exhibit good corrosion resistance [62]. Xie et.al also reported the lower corrosion resistance of samples with high porosity [57]. Table 4.1 summarizes the PDP response of sintered alloys in 0.2M NaCl and 0.5M H_2SO_4 solutions.

Table 4.1: PDP results of Fe_{80}-Cr_{18}-Si_2 alloy sintered at three different temperature in 0.2M NaCl and 0.5M H_2SO_4 solutions

Electrolyte	**0.2M NaCl**					**0.5M H_2SO_4**				
Sample	*Ecorr*	*icorr*	*Epass*	*Epit*	*Ip*	*Ecorr*	*Icorr*	*Epass*	*Epit*	*Ip*
	mV	*nA*	*mV*	*mV*	*μA*	*mV*	*μA*	*mV*	*mV*	*μA*
900 °C	-549.7	4.526	-480	N/A	N/A	-505	176.2	-170	N/A	N/A
1000 °C	-539.5	1.824	-480	-453.6	26.5	-454.8	41.48	-170	-75.54	6.215
1100 °C	-533.4	0.154	-480	-454.8	8.522	-340.1	8.033	-170	241.5	1.184

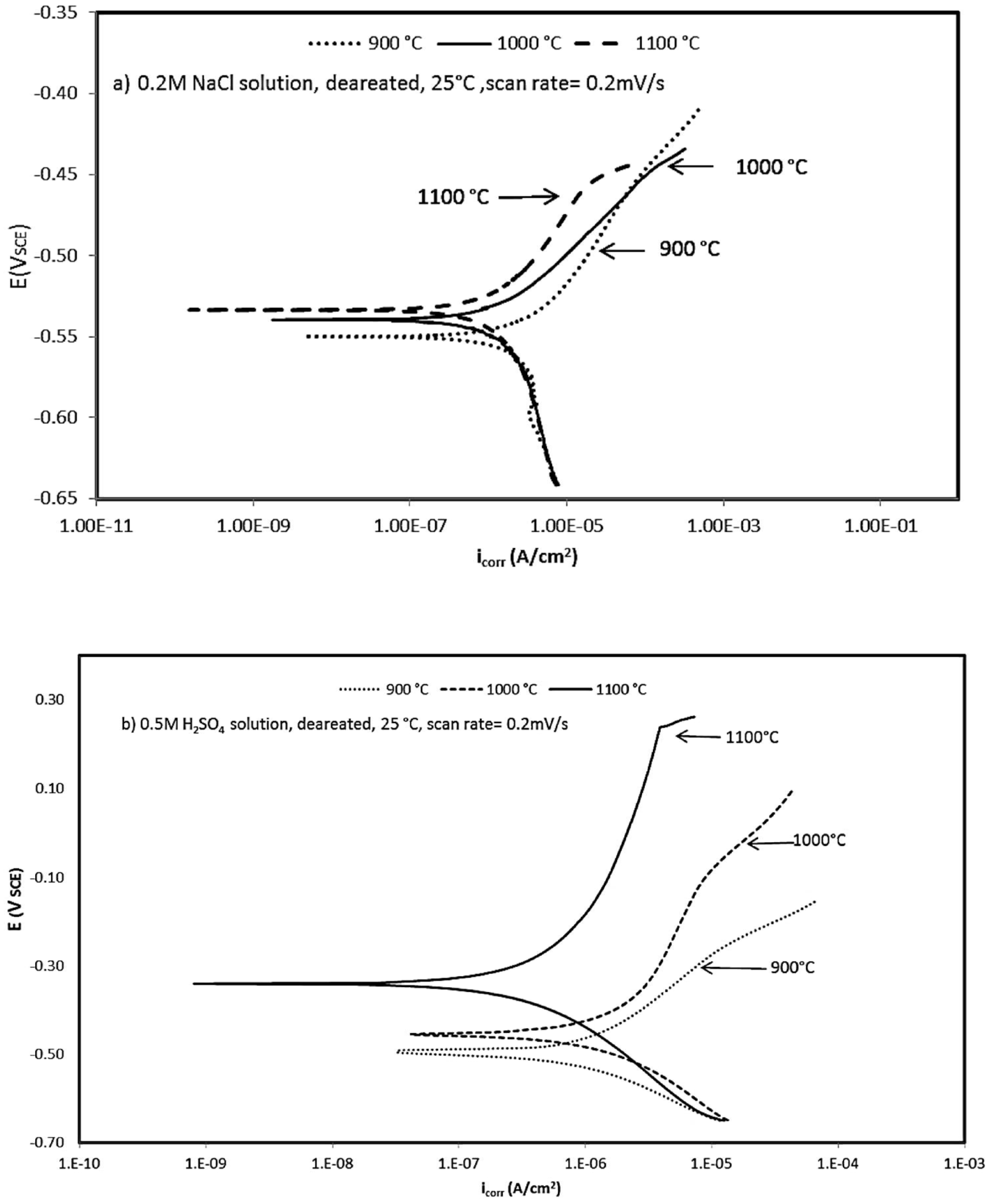

Figure 4.19: PDP curves showing the effect of sintering temperature on the corrosion behavior of $Fe_{(82-x)}$-Cr_{18} -Si_x (x = 2) alloy a) 0.2M NaCl b) 0.5M H_2SO_4 solution.

Similarly, the effect of holding time on the electrochemical properties of $Fe_{(82-x)}$ - Cr_{18}-Si_x (x = 2) under the same conditions was also studied. The powders were sintered at

1100 °C, varying holing time (5, 10 and 15 min), heating rate of 100 degree/min and 50 MPa of applied pressure. Fig. 4.20 (a & b) shows the PDP response of sintered alloys in 0.2M NaCl and 0.5M H_2SO_4 respectively. Densification values showed that, sample sintered with 15 min holding exhibit highest (91.4%) densification and is expected to have high corrosion resistance as compare to that of low densification samples. Fig clearly shows that, sample sintered with 15 min holding have Ecorr values of -512.3 and -340.1 mV_{SCE} in 0.2M NaCl and 0.5M H_2SO_4 respectively. The reason for the high corrosion resistance is high density at higher holding time. Summary of Potentiodynamic response of Fe $_{(82-x)}$-Cr_{18}-Si_x (x = 2) alloy sintered with different holding time have been shown in Table 4.2.

Table 4.2: PDP results of $Fe_{(82-x)}$-Cr_{18} -Si_x (x = 2) alloy sintered at three different holding time in 0.2M NaCl and 0.5M H_2SO_4 solutions

Electrolyte	**0.2M NaCl**					**0.5M H_2SO_4**				
Sample	*Ecorr*	*icorr*	*Epass*	*Epit*	*Ip*	*Ecorr*	*Icorr*	*Epass*	*Epit*	*Ip*
	mV	*nA*	*mV*	*mV*	*µA*	*mV*	*µA*	*mV*	*mV*	*µA*
5 min	-539.5	1.824	-488.5	N/A	26.29	-378.3	31.23	-60.68	-38.83	21.36
10 min	-533.4	0.1544	-488.5	-460.1	8.474	-405	40.49	-60.68	237.9	7.723
15 min	-512.3	0.548	-488.5	-438.8	4.093	-340.1	8	-60.68	234.2	1.88

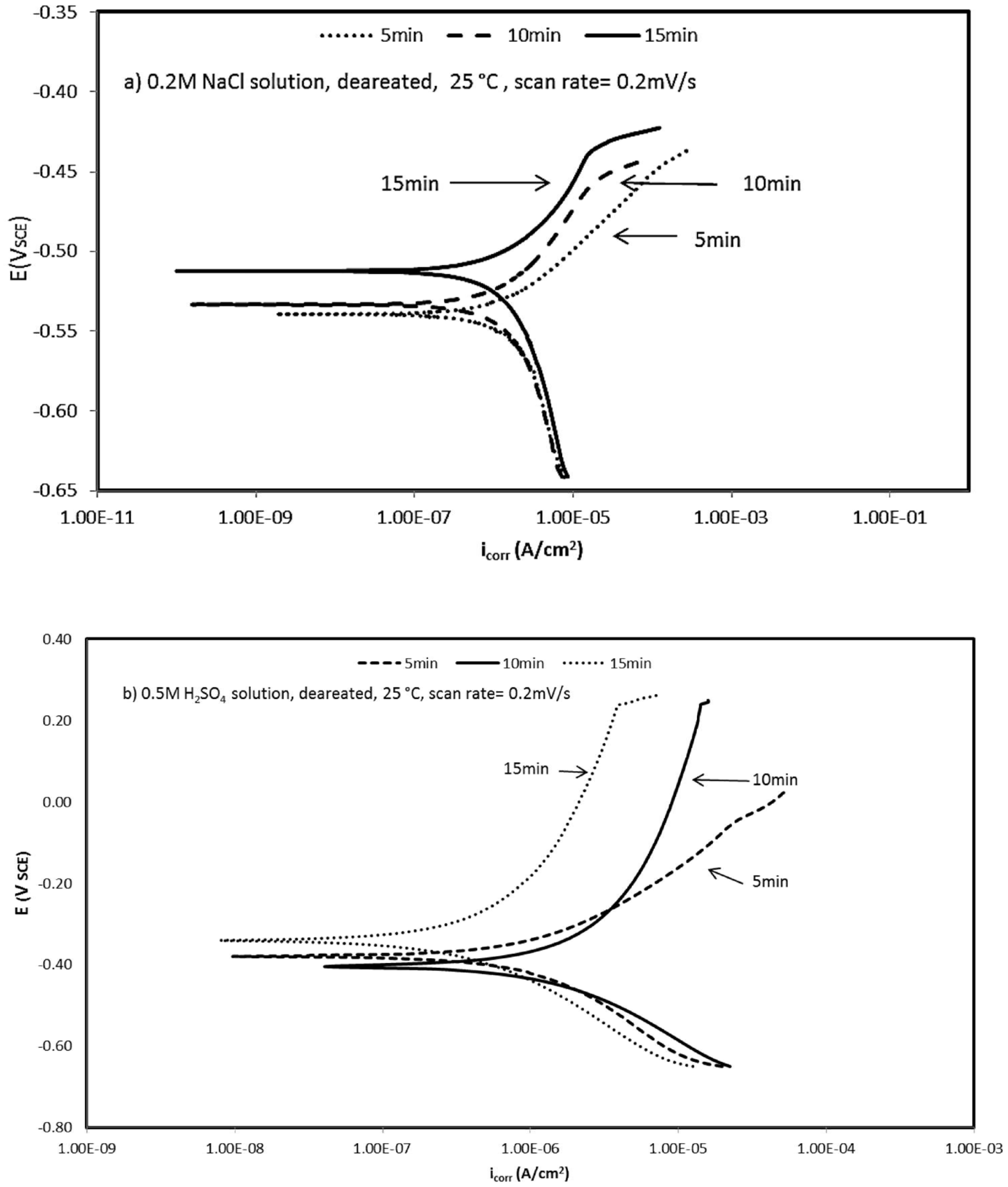

Figure 4.20: PDP curves showing the effect of sintering temperature on the corrosion behavior of $Fe_{(82-x)}$-Cr_{18} -Si_x (x = 2) alloy a) 0.2M NaCl b) 0.5M H_2SO_4 solution.

4.1.4.1.2. Linear Polarization Resistance (LPR)

The polarization resistance (Rp) is strongly dependent on the passive film formed on the surface of the specimen and is the direct measure of the corrosion resistance of the material [41]. LPR was conducted by changing the potential from -0.02 to 0.02V at the scan rate of 0.3 mV/sec under deaerated environment at room temperature. Fig. 4.21 (a & b) and it can be seen that as the sintering temperature increases, Rp also increases. Rp value of sample sintered at 1100 °C is very much higher than that of samples sintered at 900 & 1000 °C. The samples with low densification have low Rp value because of the absence of stable film on the surface of the samples as compare to that of high density sample. Gu et.al [63] investigated the corrosion performance of SSs Rebars coated by two different coating techniques giving different % porosity in the coating. LPR resting of coated rebars showed that, the coating with high % porosity exhibit low Rp value and coating with low % porosity exhibit high Rp value. So, presence of pores, in 900 and 1000 °C sintered samples, is the main cause of low Rp values as compare to 1100 °C sintered sample. The trend shown by LPR results in both conditions verifies PDP results that sample sintered at 1100 °C exhibit good EC properties. The results are in complete agreement with the results reported by Lins et al. while studying the effect of porosity on the electrochemical properties of phosphate conversion coatings [64]. Guo et al studied the effect of sintering temperature on the corrosion of Ti–24Nb–4Zr–7.9Sn alloys in Hank’s solution. They concluded that, the sample sintered at higher sintering temperature (1250 °C) exhibit a clear passive film as compare to that of samples sintered at lower temperatures [61]. Xie et al also reported the lower corrosion resistance properties of Ti-Mo alloys having high porosity after laser sintering

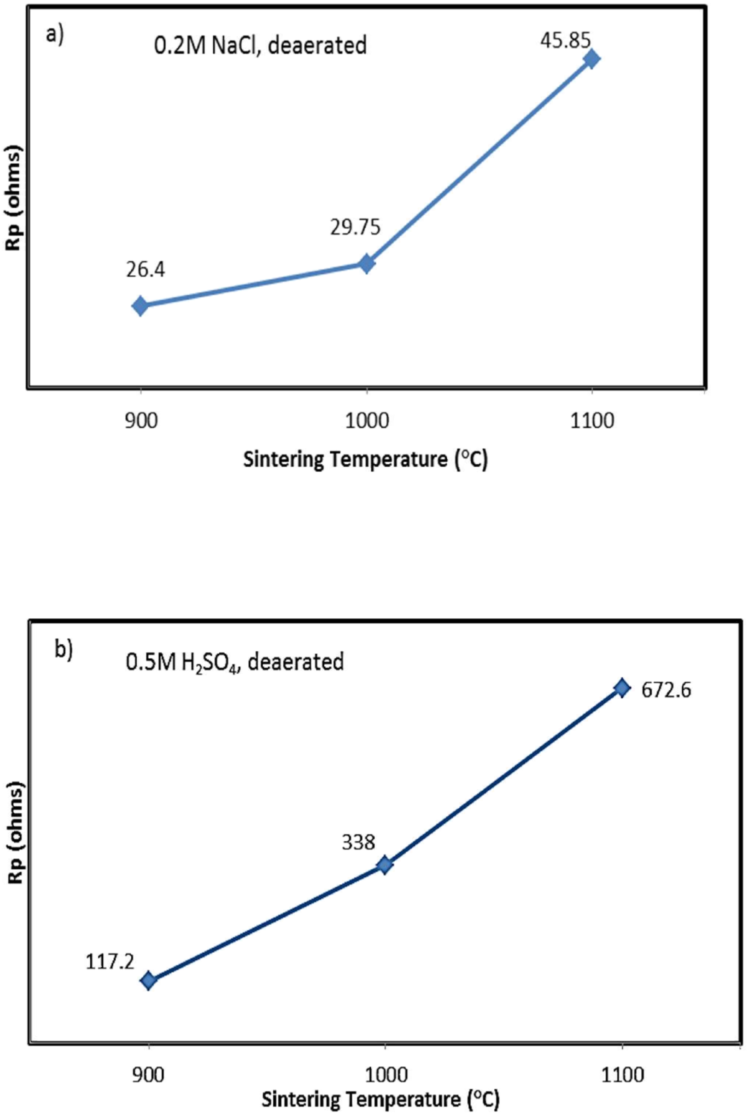

Figure 4.21: Effect of sintering temperature on the polarization resistance of $Fe_{(82-x)}$-Cr_{18} -Si_x (x = 2) sintered alloys in a) 0.2M NaCl, b) 0.5M H_2SO_4 solution

Similarly, the effect of holding times (5, 10 and 15 min) on the Rp values have been shown in Fig. 4.22 (a & b). As shown that sample sintered at 15 min holing at 1100 °C showed the maximum densification, so here it was expected that, the very sample will have high polarization resistance value. The results are in complete agreement with Guo et al.

[61] and Xie et al. [65] that high density of sintered alloys resulted in higher corrosion resistance by making a stable passive layer and consequently exhibiting higher Rp values.

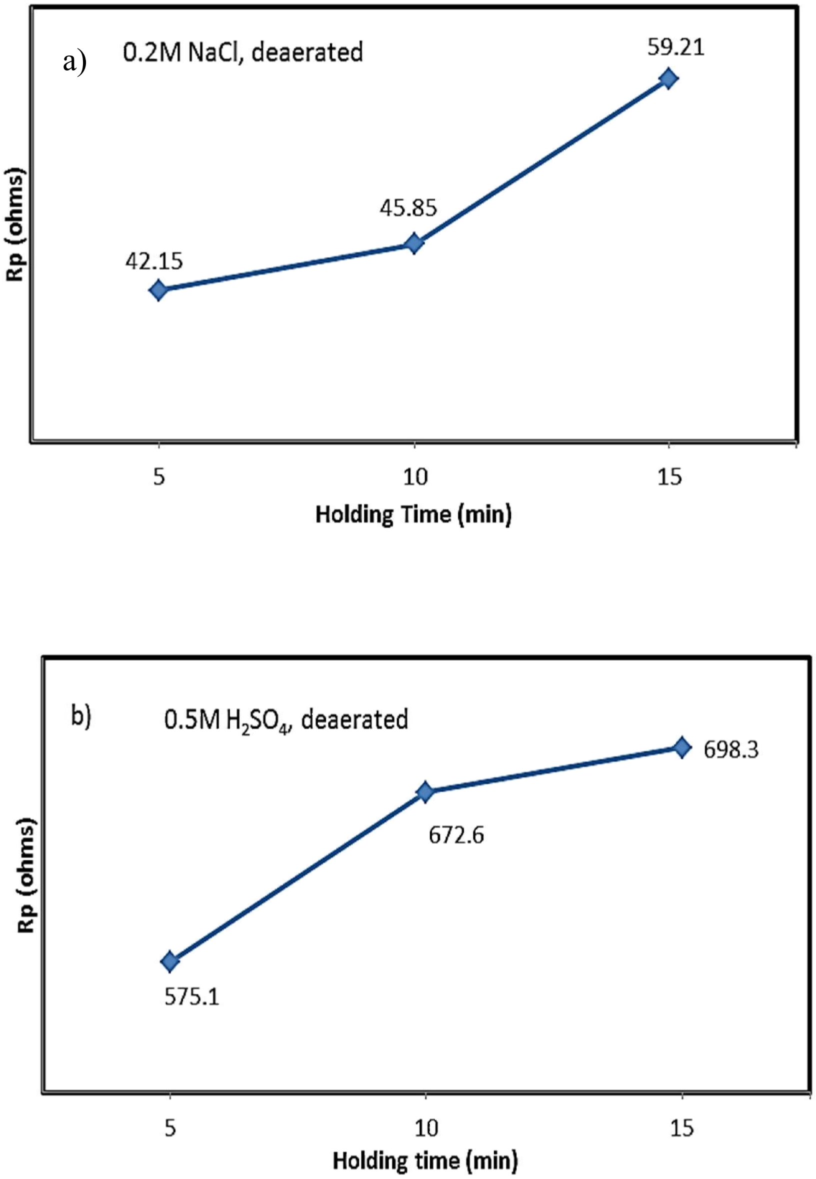

Figure 4.22: Effect of sintering holding time on the polarization resistance of $Fe_{(82-x)}$-Cr_{18} -Si_x (x = 2) sintered alloys in a) 0.2M NaCl solution, b) 0.5M H_2SO_4

4.1.4.1.3. Electrochemical Impedance Spectroscopy

Electrochemical impedance spectroscopy was also carried out to study the effect of sintering process parameters (temperature and holding time) on the electrochemical properties of $Fe_{(82-x)}$-Cr_{18}-Si_x (x = 2) alloy.

Electrochemical impedance Spectroscopy was carried out in 0.2M NaCl and 0.5M H_2SO_4 solutions at -0.50 and -0.15V DC voltage respectively. The voltage was selected from polarization curves and it lies in the passive region of all the three samples. Before conducting the test, a passive film was formed for 30 min.

Nyquist plots obtained in 0.2M NaCl and 0.5M H_2SO_4 solutions respectively are shown in the Fig. 4.24 (a & b). The diameter of the Nyquist plot is a direct function of the polarization resistance of the samples and it can be said that, the sample having larger diameter will have high corrosion resistance. Fig shows that, the spectrum of sample sintered at 1100 °C has the biggest diameter semicircle as compare to that sample sintered at 1000 and 900 °C. Gu et al. [63] investigated the quality of coatings having different % porosity ratio by EIS and concluded that, coating having high porosity have a small semi-circle diameter while coating with low porosity give exhibit large semi-circle diameter. The coating having high porosity allows the Cl- ions to pass and react with the substrate and cause corrosion Xie et al. used EIS technique to study the effect of porosity in Ti-Mo alloys sintered by laser and reported that, semicircle diameter becomes larger with the decrease of the porosity, demonstrating a nobler electrochemical behavior [65].

Since the EIS spectra are relatively simple with only one time constant, the equivalent circuit shown in Fig. 4.23 was used for quantitative study of the spectrum and good quality fitting was obtained. In the equivalent circuit, a constant phase element “CPE” was used instead of capacitance because many times the measured capacitance is not ideal. The impedance representation of CPE is given by Z(CPE) = 1/[Yo(jω)n] [41]. Here Yo is the fit parameter.

The physical meanings of the components involved in the circuit are as follows Rs correspond to the electrolyte resistance, CPE correspond to constant phase element and Rp is the polarization resistance of the passive film. The same kind of model has been used by Wallinder et.al to study the effect of surface conditions on the corrosion of 316VM SSs [34]. The results obtained after EIS curve fitting are shown in Table 4.3

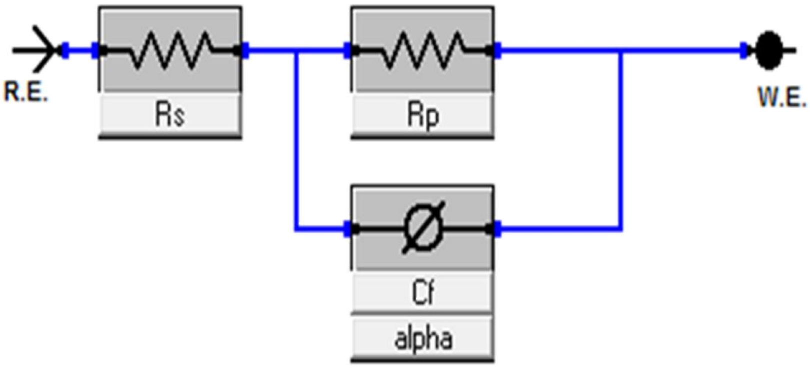

Figure 4.23: CPE model used for curve fitting

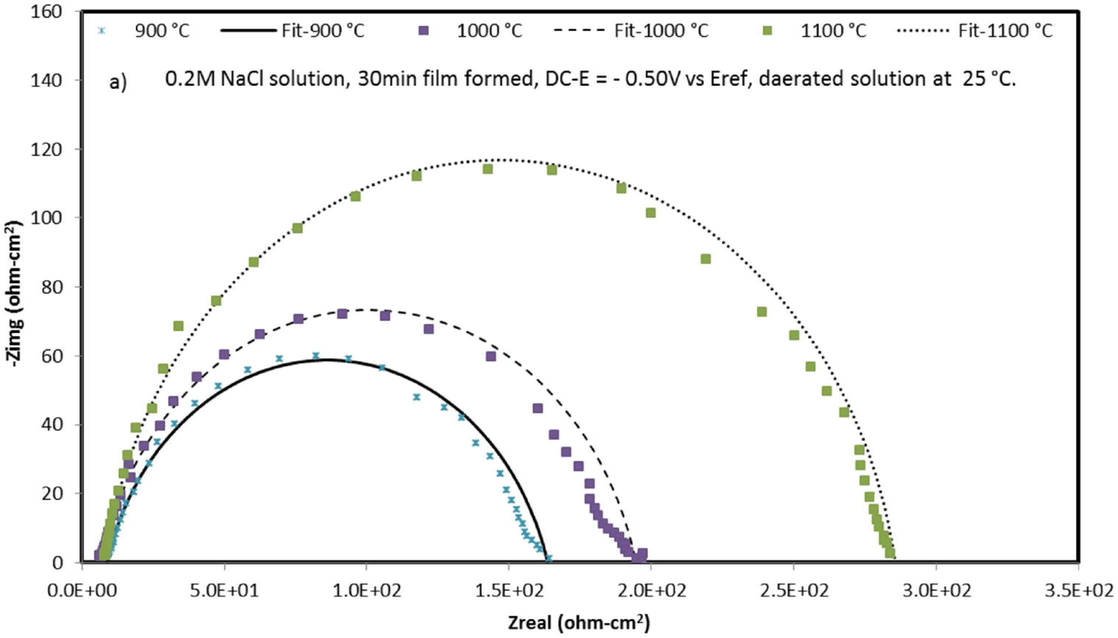

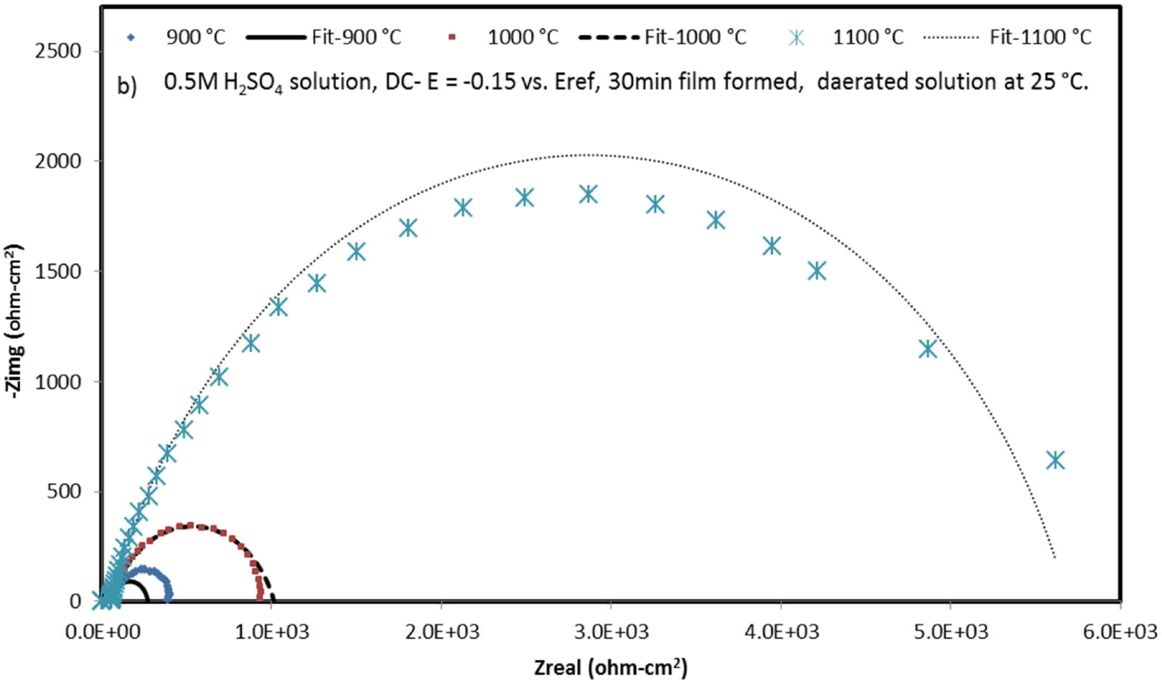

Figure 4.24: Nyquist plot of the samples sintered at different temperature along with fitting by CPE model a) 0.2M NaCl b) 0.5M H_2SO_4 solution

Table 4.3: Summary of EIS data obtained after curve fitting with CPE model

Electrolyte	***0.2M NaCl***		***0.5M H_2SO_4***	
Sample	*Rp(ohms)*	*Rs(ohms)*	*Rp(ohms)*	*Rs(ohms)*
900 °C	154.9	8.639	210.9	58.47
1000 °C	188.1	6.478	959.1	54.51
1100 °C	277.8	7.86	5.64E+03	52.49

Similar kind of experimentation was carried out at -0.475 and -0.2 V, selected from PDP, to study the effect of holding time on corrsion. It is clear from the Fig. 4.25 that, with the increase in holding time, the diameter of spectra increases. The increase in imedance is attributed to the increase in density due to higher time given to sintering. Table 4.4 shows the results of Nyquist curve fitting by CPE.

Table 4.4: Summary of EIS data obtained after curve fitting by CPE model

Sample	***0.2M NaCl***		***0.5M H_2SO_4***	
	Rp(ohms)	*Rs(ohms)*	*Rp(ohms)*	*Rs(ohms)*
5min	240.6	7.315	3.13E+03	51.74
10min	277.8	7.86	5.64E+03	52.49
15min	533.3	7.428	6.69E+03	51.82

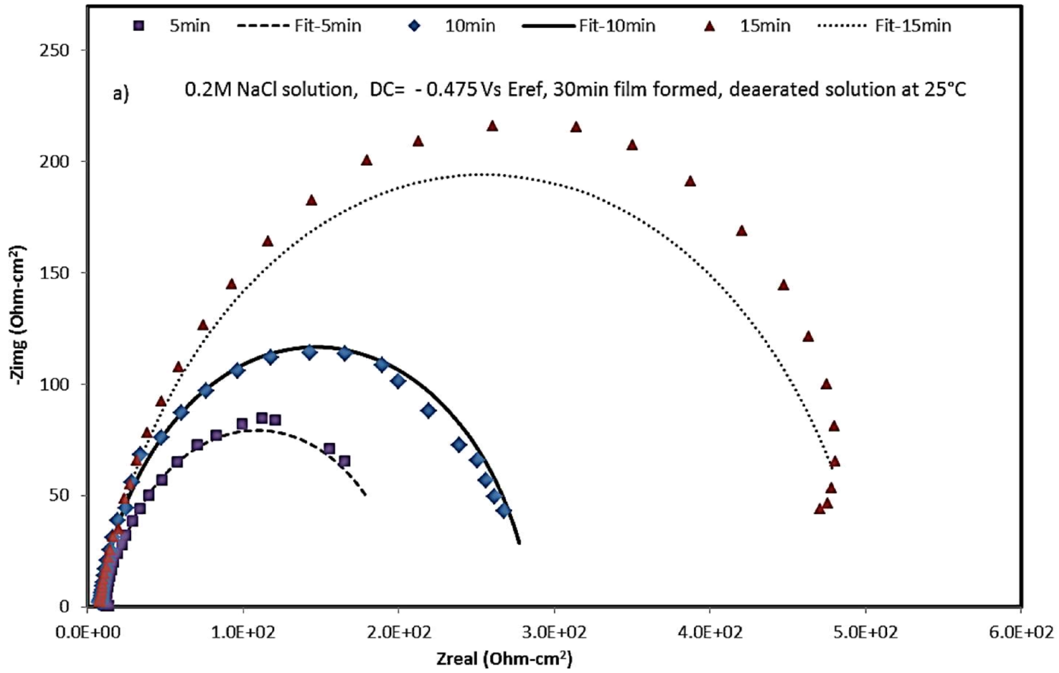

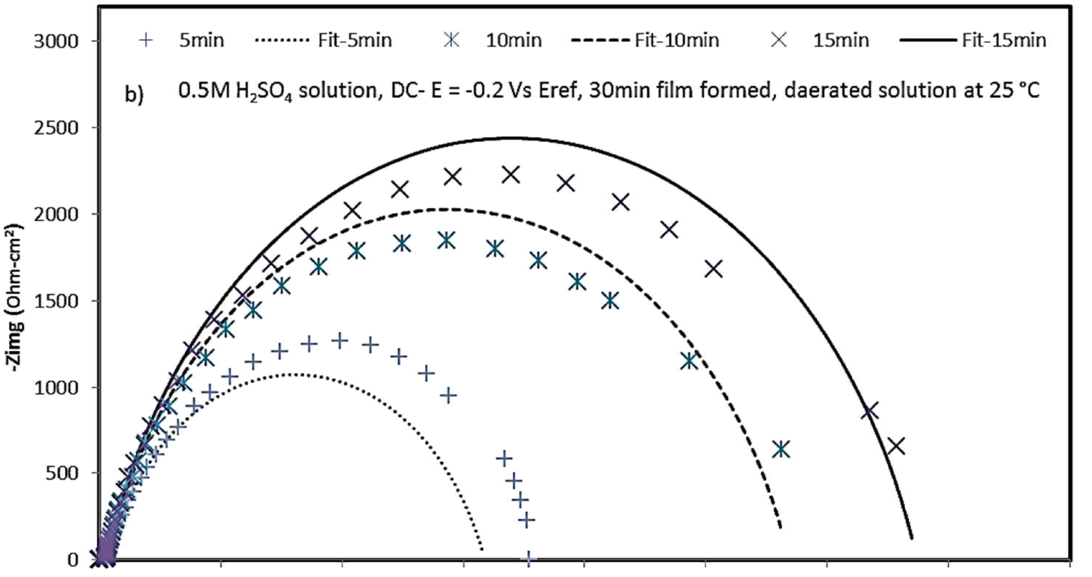

Figure 4.25: Nyquist plot of the samples sintered with different holding time along with CPE fitting a) 0.2M NaCl, b) 0.5M H_2SO_4 solution

4.1.4.2. Effect of Si on electrochemical properties of $Fe_{(82-x)}$-Cr_{18}-Si_x (x = 0, 1, 2, 3) sintered alloys

In this section, we studied the effect of Si content on the EC properties of Fe $_{(82-x)}$ Cr_{18} Si_x (x = 0, 1, 2, 3) sintered alloys by PDP, LPR and EIS. These EC investigations have been carried out in 0.2M NaCl and 0.5M H_2SO_4 solutions under deaerated environment at room temperature.

4.1.4.2.1. Potentiodynamic polarization testing

Potentiodynamic polarization tests were conducted at -0.65 to 1.2 mV_{SCE} at the scan rate of 0.05 mV/sec, under deaerated environment at room temperature.

Fig. 4.26 (a & b) shows the PDP response of $Fe_{(82-x)}$-Cr_{18}-Si_x (x = 0, 1, 2, 3) sintered alloys in deaerated 0.2M NaCl and 0.5M H_2SO_4 solutions at room temperature. Different parameters [Epit (pitting potential), i_{corr} (corrosion current density), i_p (passive current density), Ecorr (corrosion potential)] were calculated and have been summarized in Table 4.5.

From Fig and Table, it can be inferred that wt. % Si does not have a significant effect on Ecorr values but it does have a positive effect on the i_{corr} (nA) of sintered alloys. The highest i_{corr} was 98.42 nA for $Fe_{(82-x)}$-Cr_{18}-Si_x (x = 0) alloy and the lowest was 10.08 nA for $Fe_{(82-x)}$-Cr_{18}-Si_x (x = 3) sample in 0.2MNaCl solution. Similarly, in 0.5M H_2SO_4 solution, highest i_{corr} was 1.752 µA and lowest was 0.821 µA for $Fe_{(82-x)}$-Cr_{18}-Si_x (x = 0) and $Fe_{(82-x)}$-Cr_{18}-Si_x (x = 3) respectively.

It is well known that, pitting potential (E_{pit}) is an important parameter for the investigation of localized corrosion resistance of passive materials. E_{pit} is highest (-

125.2mV) for sample with 3 wt. % Si as compare to other samples and it can be said that sample with 3 wt. % Si is most resistant to localized corrosion under these conditions. Similarly if we compare the passive current density of these samples at -300 mV_{SCE}, it is the lowest for sample with 3 wt. % Si which means that, sample with 3 wt. % Si has a more protective passive film and capable to protect the sample as compare to others $Fe_{(82-x)}$-Cr_{18}-Si_x (x = 0, 1, 2).

Many authors reported the positive effect of Si content on the corrosion properties of SSs. Velasco et al. [15] compared the i_{corr} values of the alloy prepared by PM having Si content with commercially produced cast alloy without Si content. Despite the fact that cast alloys are dense as compare to that of sintered alloys, they observed that Si has the beneficial effect on the corrosion properties. Toor et al. [20] investigated the effect of Si content on 304 and 304Si SSs and reported that Si has a pronounced positive effect on the Epit of the alloys. Nishimura et al. [28] deposited the Si on the SUS 304 SSs and studied the effect of Si on the pitting corrosion resistance and crevice corrosion resistance. They found out that, Si enhanced both the pitting corrosion and crevice corrosion resistance as compare to that of simple SUS 304 SSs. Tasi et al. [67] studied the effect of Si content on the corrosion resistance of 304 sintered SSs. They reported the formation of SiO_2 layer on the surface of the sample having Si content which helps in improving the corrosion resistance as compare to the sample without Si. So, now it is established that, the reasons for the improvements in the corrosion resistance of Si containing SSs is because of the presence of Si in the passive layer. Robin et al. [69] developed the correlation between the composition of the passive layer and the corrosion resistance of SSs with Si content. The XPS studies of the passive layer revealed that, Si is present in the passive layer in large amount.

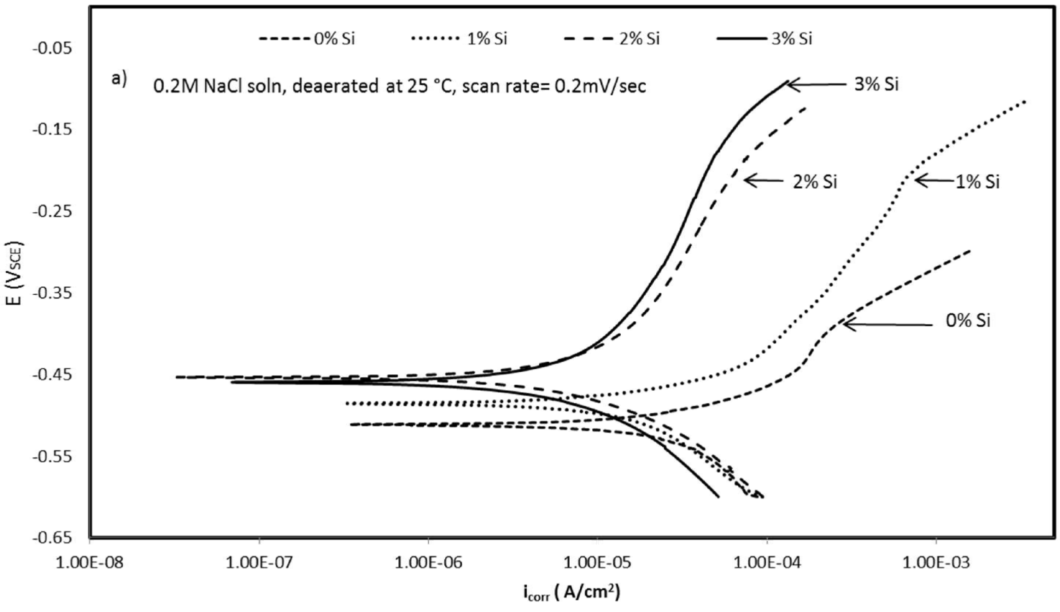
0% Si
1% Si
2% Si
3% Si
a)
0.2M NaCl soln, deaerated at 25 °C, scan rate= 0.2mV/sec
3% Si
2% Si
1% Si
0% Si
-0.05
-0.15
-0.25
-0.35
-0.45
-0.55
-0.65
E (VSCE)
1.00E-08
1.00E-07
1.00E-06
1.00E-05
1.00E-04
1.00E-03
icorr (A/cm2)

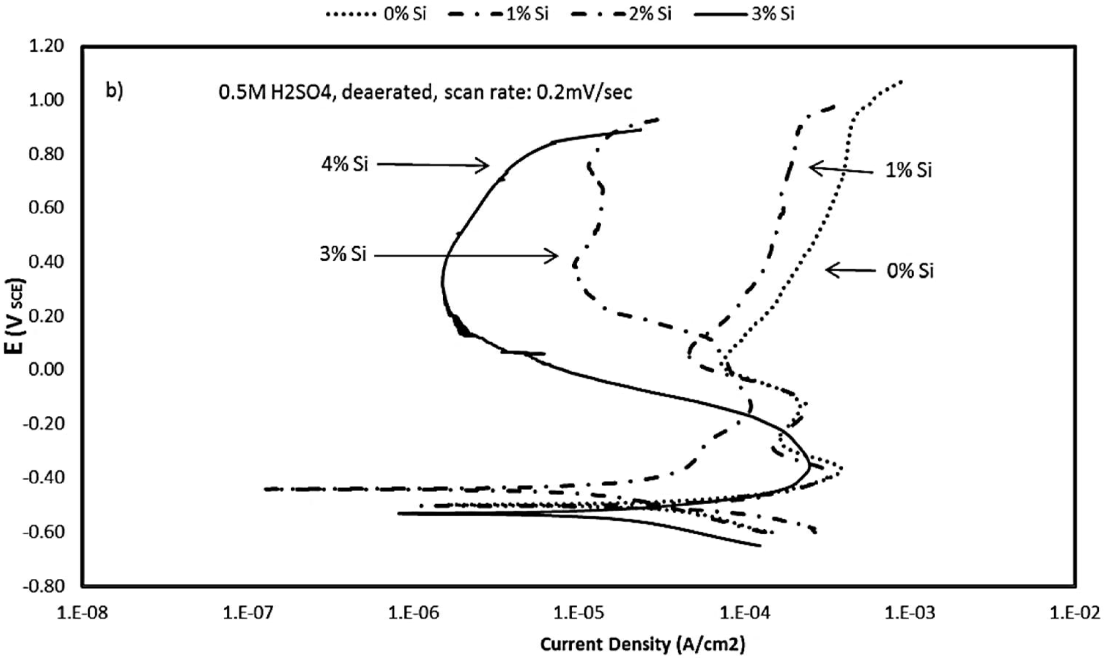

Figure 4.26: PDP response of $Fe_{(82-x)}$-Cr_{18} -Si_x (x = 0, 1, 2, 3) sintered alloys a) 0.2M NaCl, b) 0.5M H_2SO_4 solutions

Table 4.5 PDP results of $Fe_{(82-x)}$ -Cr_{18} -Si_x (x = 0, 1, 2, 3) sintered alloys in 0.2M NaCl and 0.5M H_2SO_4 solutions

Electrolyte	**0.2M NaCl**					**0.5M H_2SO_4**				
Sample	E_{corr}	i_{corr}	E_{pass}	E_{pit}	i_p	E_{corr}	i_{corr}	E_{pass}	E_{pit}	i_p
	mV	nA	mV	mV	μA	mV	μA	mV	mV	μA
0% Si	-511.8	98.42	-300	-398.4	393.3	-482.3	1.752	442	937.5	292
1% Si	-485.8	86.66	-300	-220.1	82.23	-497.9	1.573	442	937.7	288

2% Si	-460	63.63	-300	-164.1	37.63	-442	1.089	442	838	12.2
3% Si	-454.5	10.08	-300	-125.2	28.92	-529.9	0.821	442	844.7	1.67

4.1.4.2.2. **Linear Polarization Resistance**

LPR was conducted by changing the potential from -0.02 to 0.02V at the scan rate of 0.3 mV/sec under deaerated environment at room temperature.

Fig. 4.27 (a & b) shows the LPR response of $Fe_{(82-x)}$-Cr_{18}-Si_x (x = 0, 1, 2, 3) sintered alloys in 0.2M NaCl and 0.5M H_2SO_4 solutions respectively. It can be inferred from the Fig that the sample having high wt. % Si content (3 %) have high Rp value while the sample having low wt. % Si (0 %) have low Rp value. As Rp value is a direct measure of the corrosion resistance of the material, so it is clear that Si improves the corrosion resistance of the material.

LPR is a very useful tool in measuring the corrosion resistance of the steels. Many researchers have used this technique to investigate the effect of different environments on the corrosion resistance of steels. Vuković et al. studied the inhibition effect of Thiobacillus ferrooxidans Bacteria on the corrosion of steel by LPR technique [70]. Choi et al. studied the corrosion behavior of carbon steel and weathering steel in aerated acidic chloride solution by using weight loss and LPR technique [99].

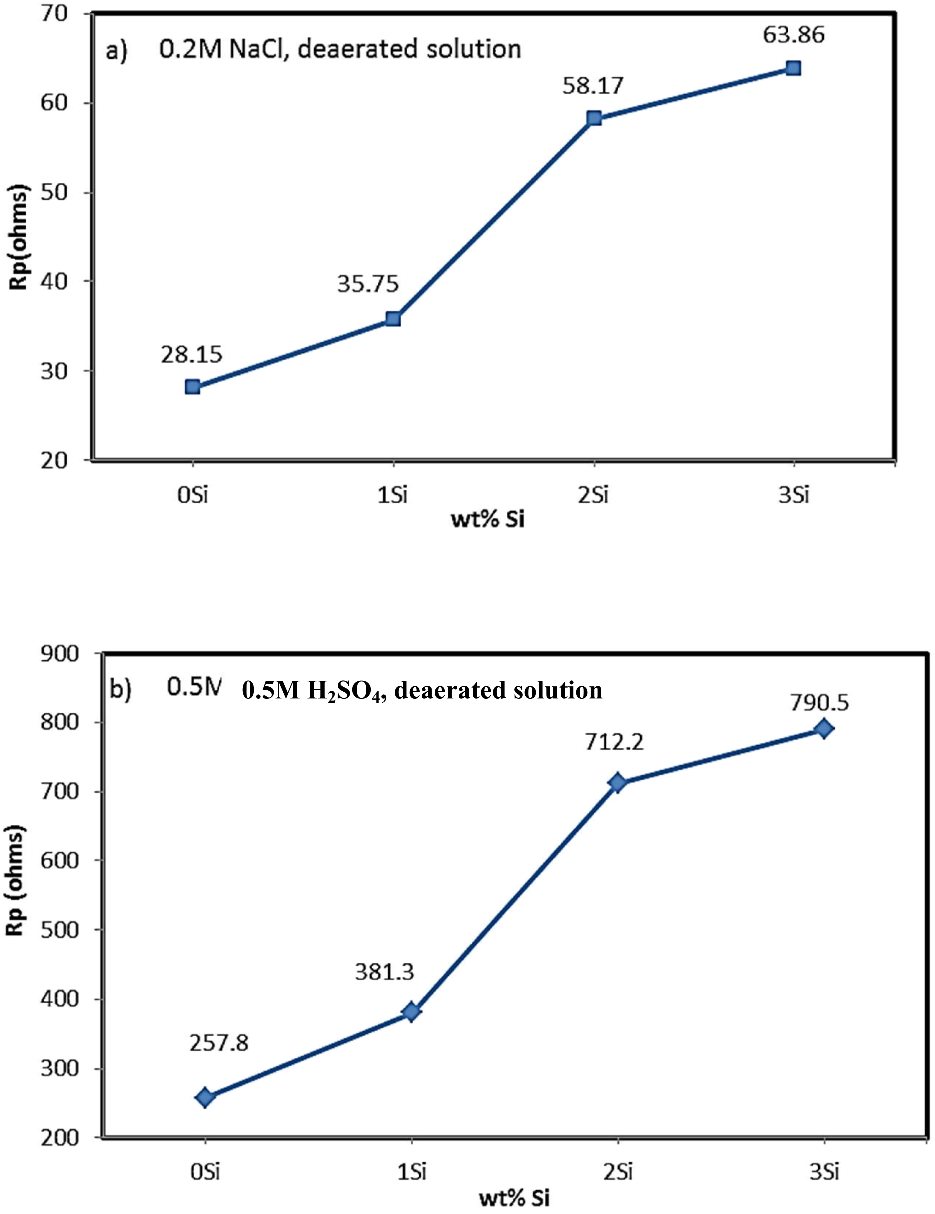

Figure 4.27: Linear polarization response of $Fe_{(82-x)}$-Cr_{18}-Si_x (x = 0, 1, 2, 3) sintered alloys in a) 0.2M NaCl, b) 0.5M H_2SO_4 solutions

4.1.4.2.3. Electrochemical Impedance Spectroscopy

Electrochemical impedance Spectroscopy was carried out at -0.2 and 0.2V DC voltage in 0.2M NaCl and 0.5M H_2SO_4 solutions respectively. The voltage was selected from polarization curves and it lies in the passive region of all the samples. Before conducting the test, a passive film was formed for 30 min.

Nyquist plot (Fig. 4.28 a & b) have been drawn to show the effect of Si content on the electrochemical properties of $Fe_{(82-x)}$ -Cr_{18} -Si_x (x = 0, 1, 2, 3) sintered alloys in 0.2M NaCl and 0.5M H_2SO_4 solutions. The diameter of the Nyquist is a direct function of the corrosion resistance of the samples and it can be said that, the sample having larger diameter will have high corrosion resistance. Fig shows that, $Fe_{(82-x)}$-Cr_{18} -Si_x (x = 3) have the highest diameter semi-circle as compare to other samples $Fe_{(82-x)}$-Cr_{18}-Si_x (x = 0, 1, 2). To fit the EIS spectra, CPE model (shown in Fig. 4.27) has been used and the results have been given in table 4.6.

Generally, electrochemical impedance spectroscopy is used to study the stability of passive film of Stainless steels. Many authors used this technique to study the behavior of passive films of different alloys in different conditions. Jinlong et al. studied the effect of grain size corrosion behavior of 304SSs by using EIS in borate buffer solution and reported that, nano-crystalline 304SSs have a semi-circle with much higher diameter as compare to micro-crystalline 304SSs [71]. C Garcia et al. studied the passivation behavior of austenitic and duplex SSs by using EIS technique in pore solution [72].

Table 4.6: Summary of EIS results of Fe$_{(82-x)}$ -Cr$_{18}$ -Si$_x$ (x = 0, 1, 2, 3) alloys obtained after curve fitting by CPE model

Sample name	0.2M NaCl			0.5M H_2SO_4		
	Rp (Ohm)	Rs (Ohm)	CPE $\mu F/cm^2$	Rp (Ohm)	Rs (Ohm)	CPE $\mu F/cm^2$
0% Si	171.1	36.22	2.60E-01	668.5	31.47	1.54E-01
1% Si	424.2	37.34	2.38E-01	776.5	29.39	1.64E-01
2% Si	722.7	35.82	3.02E-01	2.34E+03	24.03	5.67E-01
3% Si	876.5	40.16	8.35E-01	5.65E+03	28.46	5.67E-01

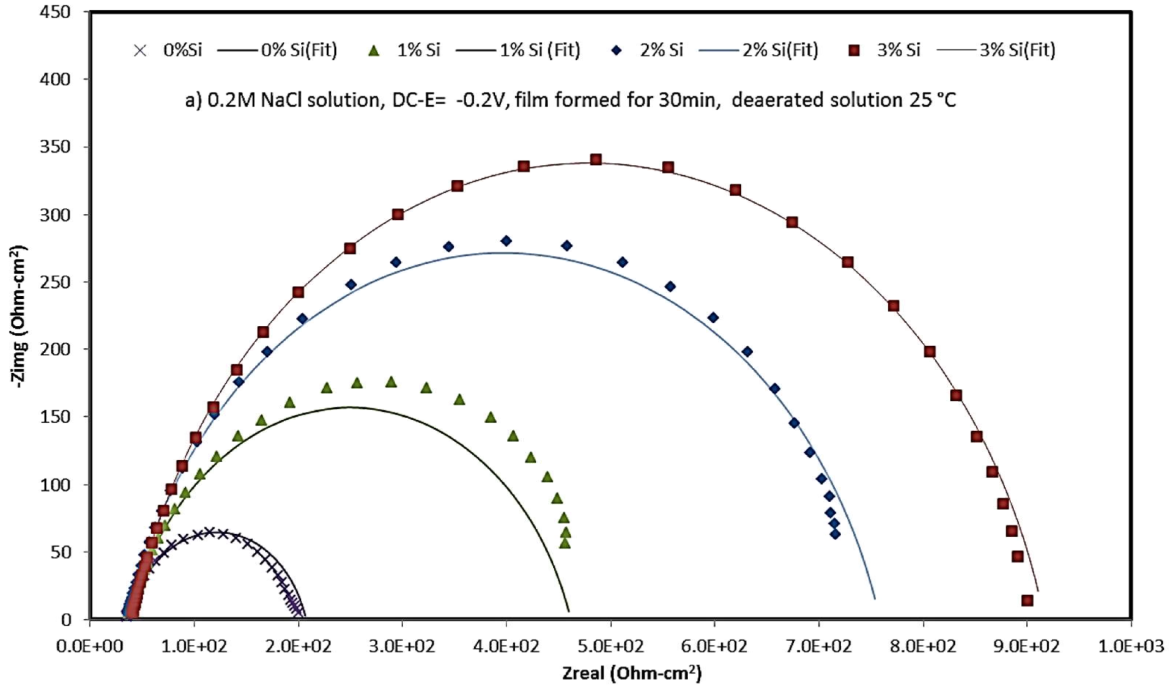

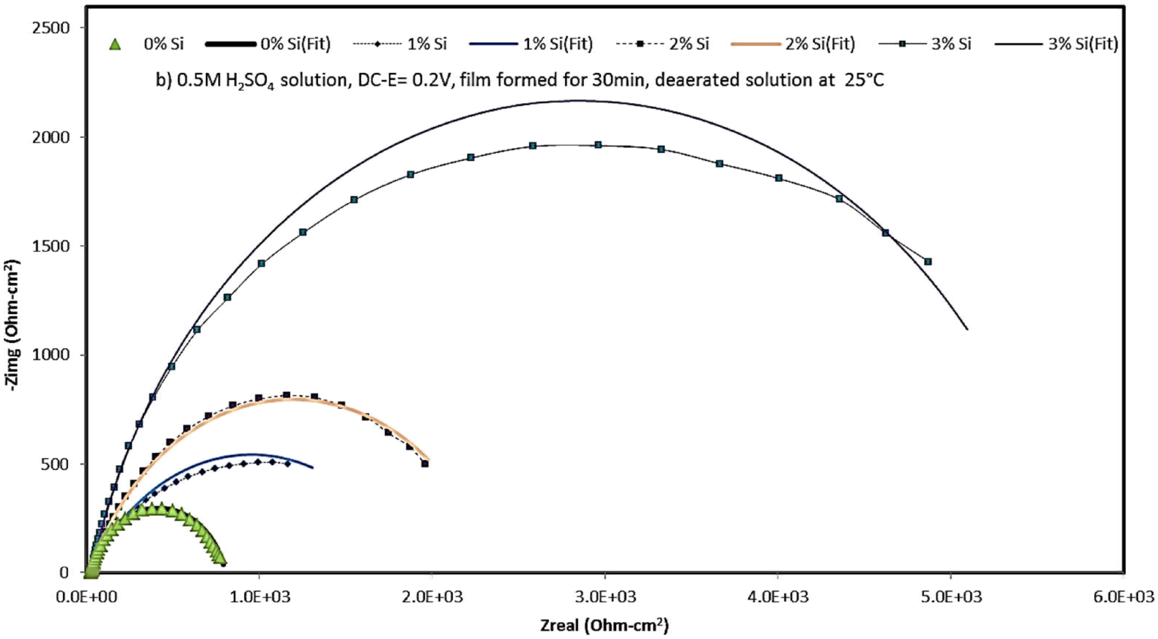

Figure 4.28: EIS (Nyquist Plot) response of Fe(82-x) Cr18-Six (x = 0, 1, 2, 3) sintered alloys in a) 0.2M NaCl, b) 0.5M H_2SO_4 solutions

4.1.5. Passive film analysis by using XPS

XPS was carried out on $Fe_{(82-x)}$-Cr_{18}-Si_x (x = 0, 1, 3) sintered alloys to study the passive film formed in 0.5 H_2SO_4 solution at -0.2mV for 30min at room temperature. Since the passive layer on SSs is of some tenths of Angstroms, XPS analysis gives a measure of overall film composition. Fig. 4.29 (a, b & c) show Fe_{2p}, Cr_{2p} and Si_{2p} XPS spectra recorded at 90° respectively.

The Fe_{2p} ionization results show that, the passive layer developed on 0% Si alloy at -0.2mV consist of mainly Fe-oxide (Fig. 29 a). The oxide of iron can be either Fe_2O_3 or Fe_3O_4. But it is very difficult to differentiate between them. So the species found in the range of 710-711 eV be generally assigned as Fe^{+3}. In all Fe_{2p} spectra, the dominant peak was associated with Fe^{+3}. The presence of pure Fe has not been analyzed in any of the alloy.

Cr_{2p} ionization (Fig. 29 b) was characterized by the presence of peak around 577 eV. This peak is related to the Cr^{+3} oxides. The results showed that, Cr-oxides are present on the surface of both 1 and 3 wt. % Si alloy. Very small contribution of Cr metal can also be seen at lower binding energy values. Since the passive layer on SSs is mainly composed of Cr-oxide, thus it can be said that, both the alloys undergo passivation at -0.2mV. This result justifies the PDP results. As this potential lies in the passive range of both of the alloys.

Si_{2p} ionization (Fig. 29 c) was characterized by the presence of peak at 103.5eV. This particular peak is related to the Si^{+2}. The presence of Si-oxide in the passive layer has been confirmed. There is very small concentration of Si-oxide in 1% Si alloy.

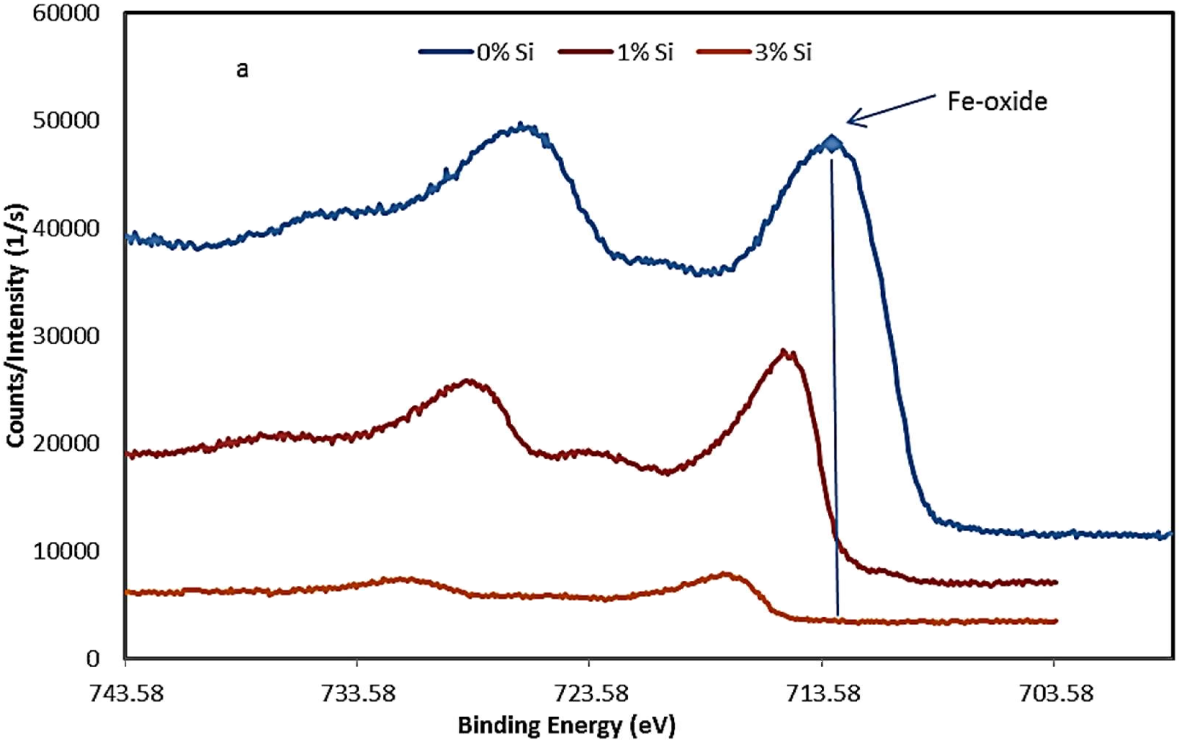

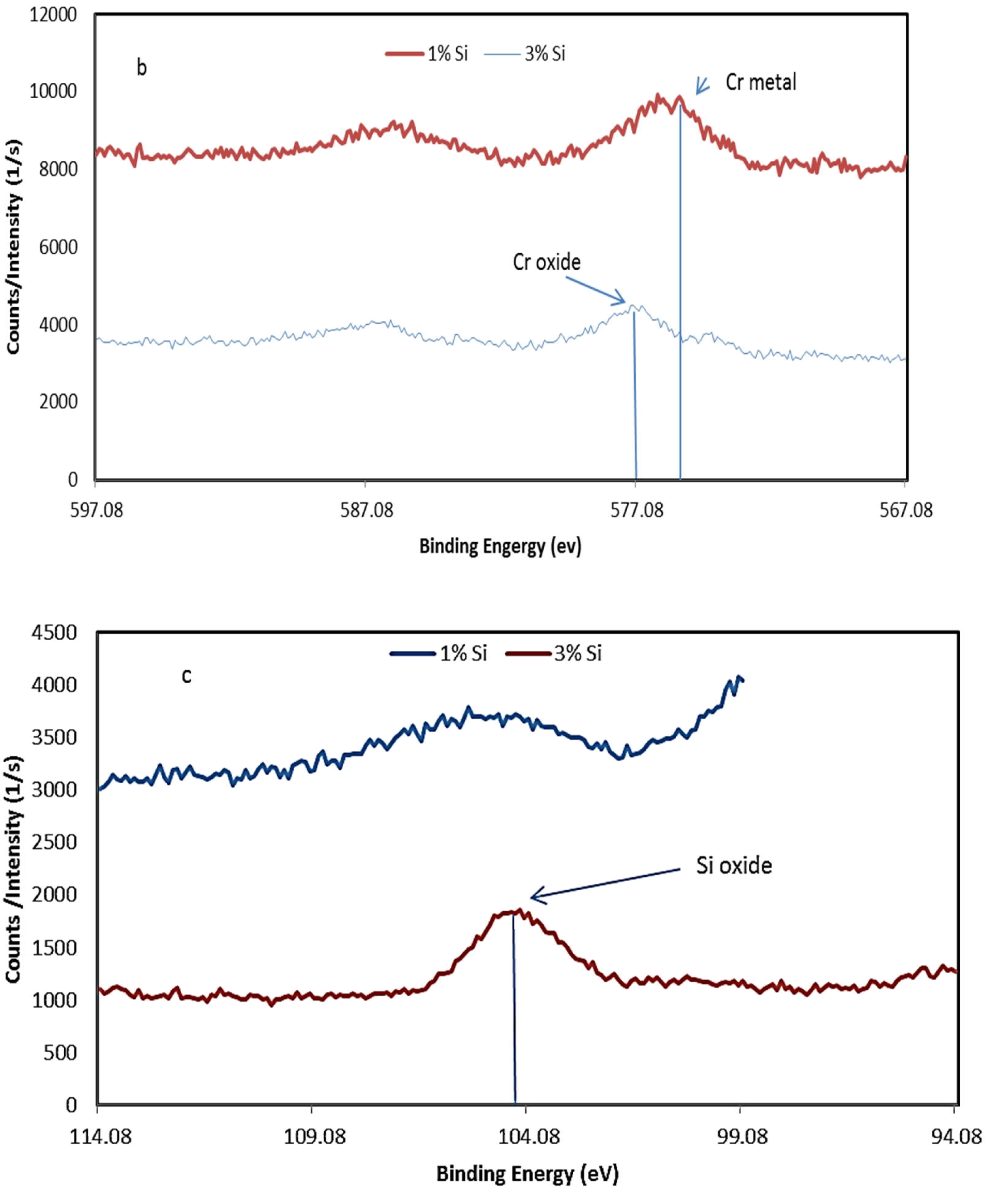

Figure 4.29: XPS analysis of $Fe_{(82-x)}$-Cr_{18}-Si_x (x = 0, 1, 3) alloys, a) Fe_{2p} , b) Cr_{2p}, c) Si_{2p}

4.2. Austenitic Stainless Steels [$Fe_{(73-x)}$-Cr_{18}-Ni_9-Si_x (x = 0, 1, 2, 3)]

Austenitic stainless steels are most widely used SSs because of their higher corrosion resistance and mechanical properties as compare to other SSs. It has found its applications in oil and gas sector, structural applications as well as in medical field including surgical cutting tools and implants.

In this section, were prepared by ball milling the pure elemental powder in 250ml hardened stainless steels vials. Ball to powder ratio was maintained at 30:1 during the complete cycle and argon was purge to provide inert atmosphere for milling. Phase evolution was studied using XRD and FE-TEM of milled powders while the morphology of milled powder was studied using SEM. Spark plasma sintering of milled powder was carried out under optimized conditions discussed in section 4.1.2. FE-SEM was used to investigate the mico-structure of sintered alloys and XRD was used to study the phase/phases formation after sintering. Electrochemical properties of $Fe_{(73-x)}$-Cr_{18} -Ni_9 -Si_x (x = 0, 1, 2, 3) alloys were studied by carrying out PDP, LPR and EIS in deaerated 0.2M NaCl and 0.5M H_2SO_4 solutions at room temperature.

4.2.1. Alloy development by MA

4.2.1.1. XRD studies of ball milled $Fe_{(73-x)}$-Cr_{18}-Ni_9-Si_x (x = 0 & 2) powders

XRD of powder specimen milled for 5, 10, 20, 50, 100, 160, and 160 h-annealed gave clear indication of the phase evolution during milling and the phase change in $Fe_{(73-x)}$-Cr_{18}-Ni_9-Si_x (x = 0 & 2) have been reported in this section. XRD of un-milled powder {Fig. 4.30 A)} showed sharp peaks of Fe and Cr while milling (5 h) resulted in the reduction of peak intensity and considerable broadening. Patil et al. [73] reported that, particle refinement due to ball milling is the cause of the broadening in the XRD pattern. It can be seen from the Fig. that, after 5 h of milling, Fe (110) peaks shifted towards higher angles (2θ = 44.66°) with little broadening because of solid solution formation of Fe-Cr-Ni and particle refinement. Fig. 4.30 B) shows that, the characteristic Fe (110) peak shifted to higher angle (2θ = 45.06°) which is due to the dissolution of Cr, Ni and Si in lattice of Fe.

Despite the fact that, Ni is a strong austenite stabilizer, there is an unexpected formation of α-phase rather than γ-phase at 5hr of milling. The formation of α-solid solution during milling of austenitic powders has been reported by many researchers in the past. Kaloshkin et al. [74] milled Fe-Ni alloy system with different percentages of Ni, milled in AGO-2U planetary mill with water-cooled vials and observed the formation of α-solid solution and called it martensitic phase. Continued milling resulted in the formation of γ-solid solution which was confirmed by XRD pattern. Enayati et al. [75] observed a phase change of stainless steel powders prepared from a planetary ball mill under argon atmosphere after 60 h milling. Oleszak et al. [76] obtained austenitic stainless steel powder using a Fritsch planetary P5 mill after milling for 100 h. Thus it can be concluded that the formation of both α (martensitic) and γ (austenitic) phases during MA depends upon milling time. Similarly, Haghir et al. [77] did annealing after 120 h of milling and studied phase transformation of α to γ. The possible reason for the formation of α-phase is that, both Ni and Cr elements decreases both the temperature of start of martensite formation as well as the completion of martensite formation [47].

Milling for 10 h resulted in the decrease in peak intensity and more broadening but XRD pattern of 20 h milled powder did not show any peak. This type of behavior is attributed to the formation of amorphous phase and has been reported by Patil et al. [73] in $Fe_{60}Co_8Zr_{10}Mo_5W_2B_{15}$ at 20 h of milling. It is well established that with the progression of milling, the long range order of constituent particles is broken down to a short range order because of the formation of different structural defects like dislocations, vacancies due to severe plastic deformation. Movahedi et al. [47] investigated Fe–Cr–Mo–B–P–Si–C system and observed the formation of saturated solid solution at early stages of milling which later with continued milling transformed to an amorphous phase. Sharma et al. [48] also reported the vanishing of Fe(110) peaks at 10 h of milling due to amorphous phase formation. Suryanarayana have enlisted many instances where the formation of amorphous phase took place due to milling of powders [30]. The criteria for the amorphous phase formation during MA is that there should be a difference in the atomic sizes of the constituent elements (solute and solvent) and produce lattice strain [50]. Egami et al. [51] explained the effect of difference in atomic sizes of constituent elements on the glass formability of metals as the lattice strain increases linearly with increasing concentration of solute atoms. When lattice strain reaches a certain value, glassy alloy becomes more energetically favorable as compare to its crystalline counterpart. In simple words, the induce lattice strain destabilizes the crystal lattice and resulting in the amorphous phase formation.

XRD results show that, even after 160 h of milling, amorphous phase did not changed to austenitic phase. As reported elsewhere [70, 71, 72] that the milling of powders to high milling time resulted in the development of γ-phase because milling intensity play an important role in the development of γ-phase. There are two things that changes with the change in milling intensity. 1) Concentration of different crystal defects. 2) Temperature of milling [70]. So we decided to anneal the powders to get the required phase. XRD (Fig. 4.30) results revealed that, the amorphous phase developed during milling transformed into austenitic phase after annealing at 1100 °C. Very low noise in the XRD of annealed powders also confirmed that, due to annealing, strains that were developed during milling have been annihilated.

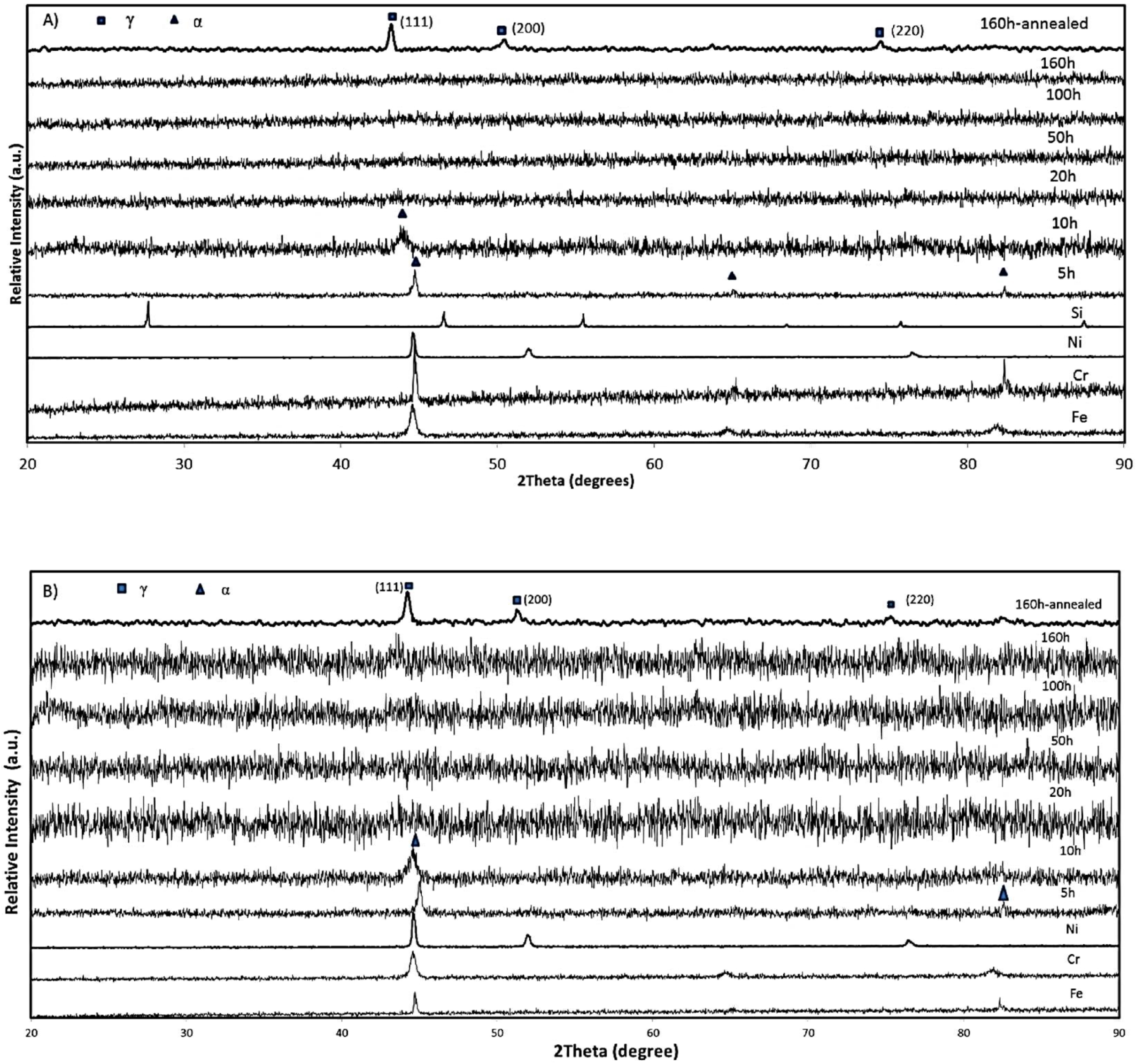

Figure 4.30: XRD analysis of ball milled powders taken at different intervals of time. A) XRD of Fe_{73}-Cr_{18}-Ni_9-Si_0 B) Fe_{71}-Cr_{18}-Ni_9-Si_2

4.2.1.2. TEM of ball milled Fe_{71}-Cr_{18}-Ni_9-Si_2 powders

To confirm the XRD results (formation of α-phase at 5 h milling and amorphous phase at 20hrs and evolution of γ-phase after annealing) FE-TEM was carried out. Fig. 4.31 (a, b) shows the BF-TEM image of 5 h milled powder and the respective SAD pattern. SAD pattern matched with that of α-phase which confirmed the formation of α-phase at 5 h of milling. Fig. 4.31 (c, d) shows the BF-TEM image of 20 h milled powder and its respective SAD pattern. The BF-TEM images confirms the particle refinement due to milling and its SAD pattern showed the diffused rings of amorphous phase as indicated by XRD results. Fig. 31 (e, f) shows the BF-TEM images of 160 h milled-annealed powder and its respective SAD pattern. The BF-TEM images confirm the particle refinement at 160h and its SAD diffraction pattern confirmed the γ-phase formation after annealing. These TEM investigations confirmed the XRD results.

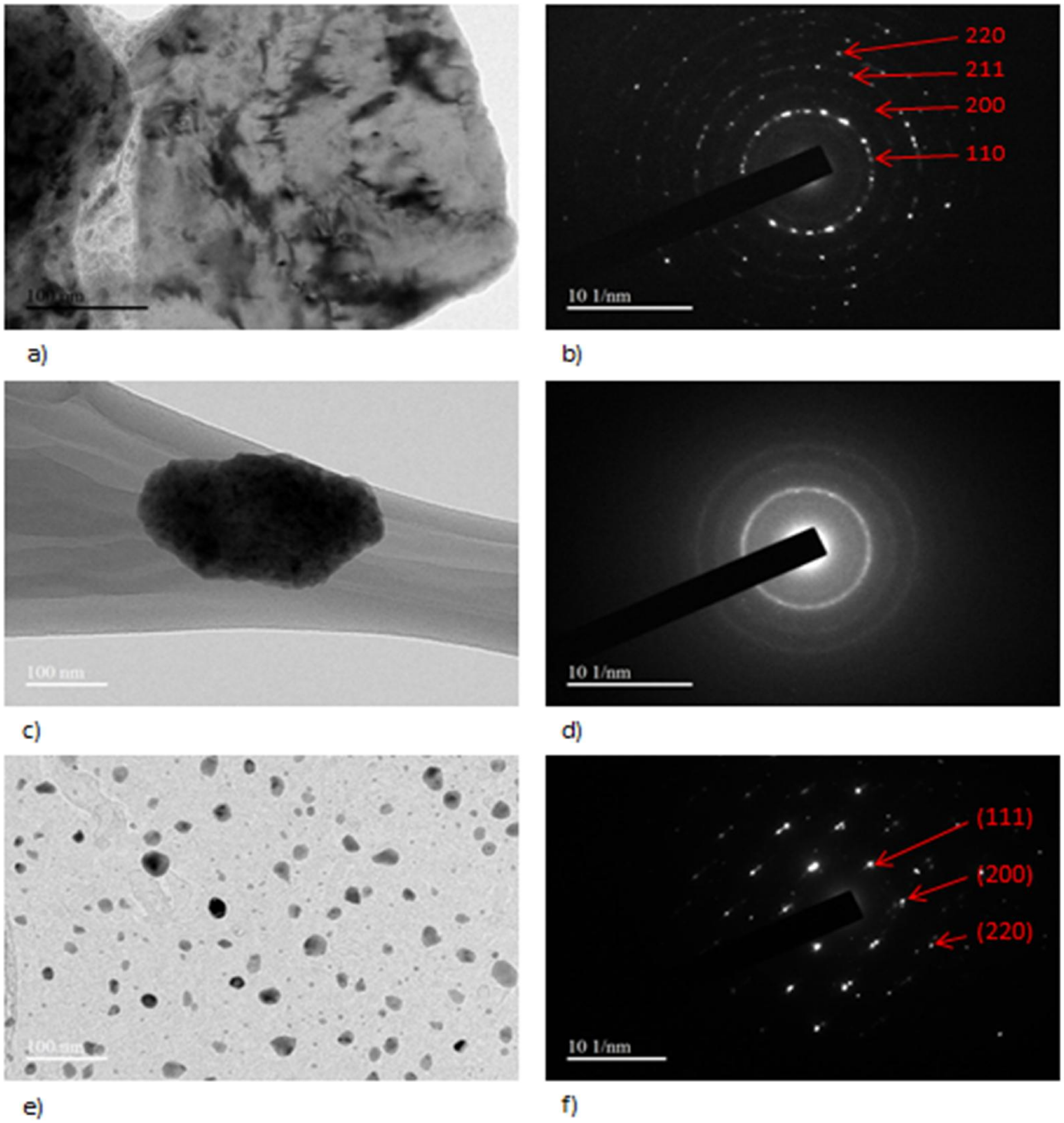

Figure 4.31: TEM bright-field images and selected area electron diffraction patterns of Fe$_{71}$-Cr$_{18}$-Ni$_{9}$-Si$_{2}$. a) 5 h milled powder, b) SAD pattern of 5 h milled powder. SAD pattern matched with the α-phase, c) 20 h milled powder, d) SAD pattern of 20 h milled powder showing amorphous phase, e) 160 h-annealed powder, f)SAD pattern of 160 h-annealed powder and it matches with γ-phase

4.2.1.3. SEM morphology of milled powders

Fig. 4.32 & Fig. 4.33 shows the morphological evolution of $Fe_{(73-x)}$-Cr_{18}-Ni_9-Si_x (x = 0 & 2) milled powders for 0, 10, 20, 50, 100, 160 h respectively. It can be seen from the Fig. that, powders have different morphologies at different milling time. Fig. 4.32 a) shows the morphology of un-milled powders where spongy particles are of Fe and smooth particles are of Cr and after 15 h of milling powder show high agglomeration of particles. At this stage, powders get flattened by the forces generated by the contact of ball-powder-ball or ball-powder-vials which lead to the increase in particle size along with the formation of some small particles as well [52]. The production of small and very large particles is usually observed in the early stage milling of ductile materials because of the continuous cycles of plastic deformation, cold welding and fracturing [52]. Increase in milling time resulted in the refinement of particles and the process continues. Suryanarayan reported that with the increase in milling time, powder particles will become finer [30].

Fig. 4.33 shows the SEM micrograph of the powder annealed at 1100 °C with different Si content. It is clear that, alloy with more wt. % Si have finer particle size. Thus it can be said that, with high percentage of Si, fracture mechanism is more predominant over cold welding. And this agreed with the results reported by [52] that the presence of Si imparts brittleness to the powders. Grain size calculations from BF-TEM revealed that, the average grain size after annealing of 160 h milled powder was less than 20nm.

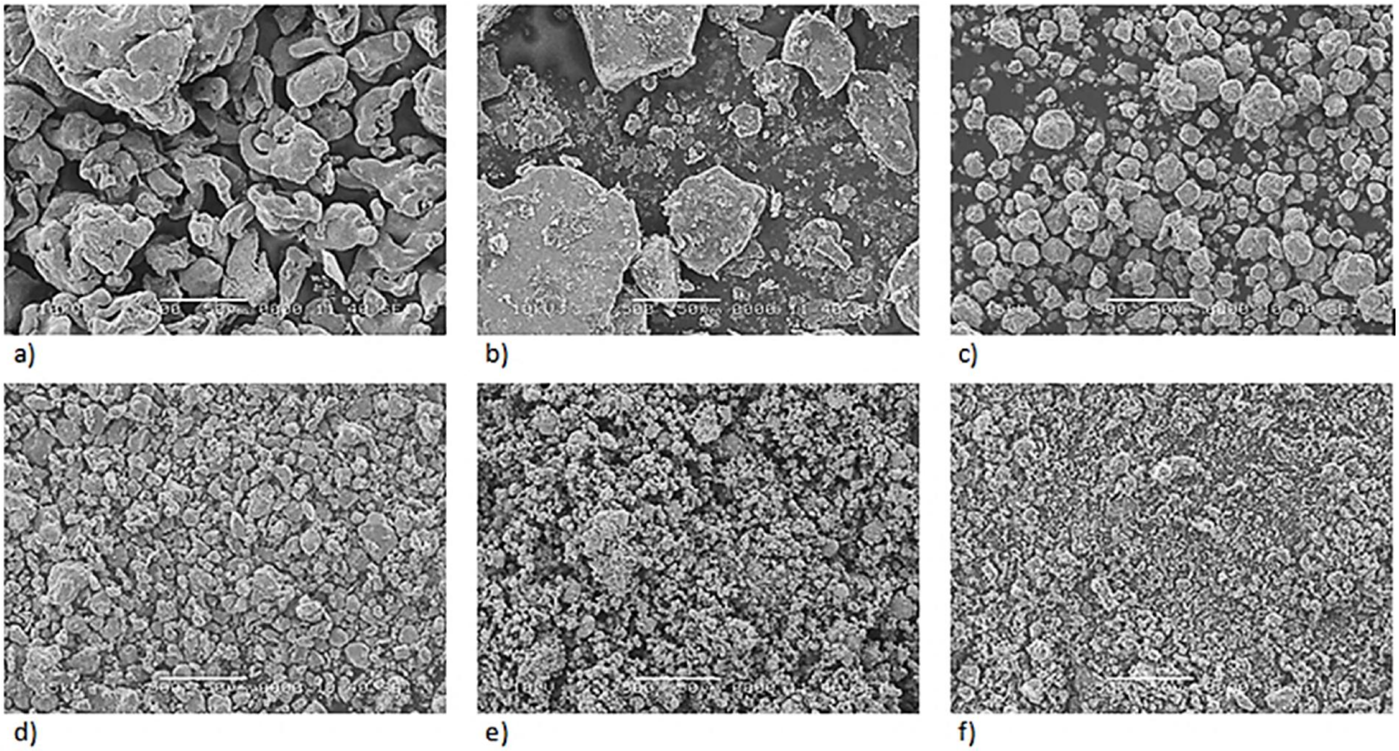

Figure 4.32: SEM morphology of Fe_{73} -Cr_{18} –Ni_9 milled powders, a) 0 h, b)20 h, c) 60 h, e)100 h, f)160 h, E) 160 h milled and annealed at 1100 °C

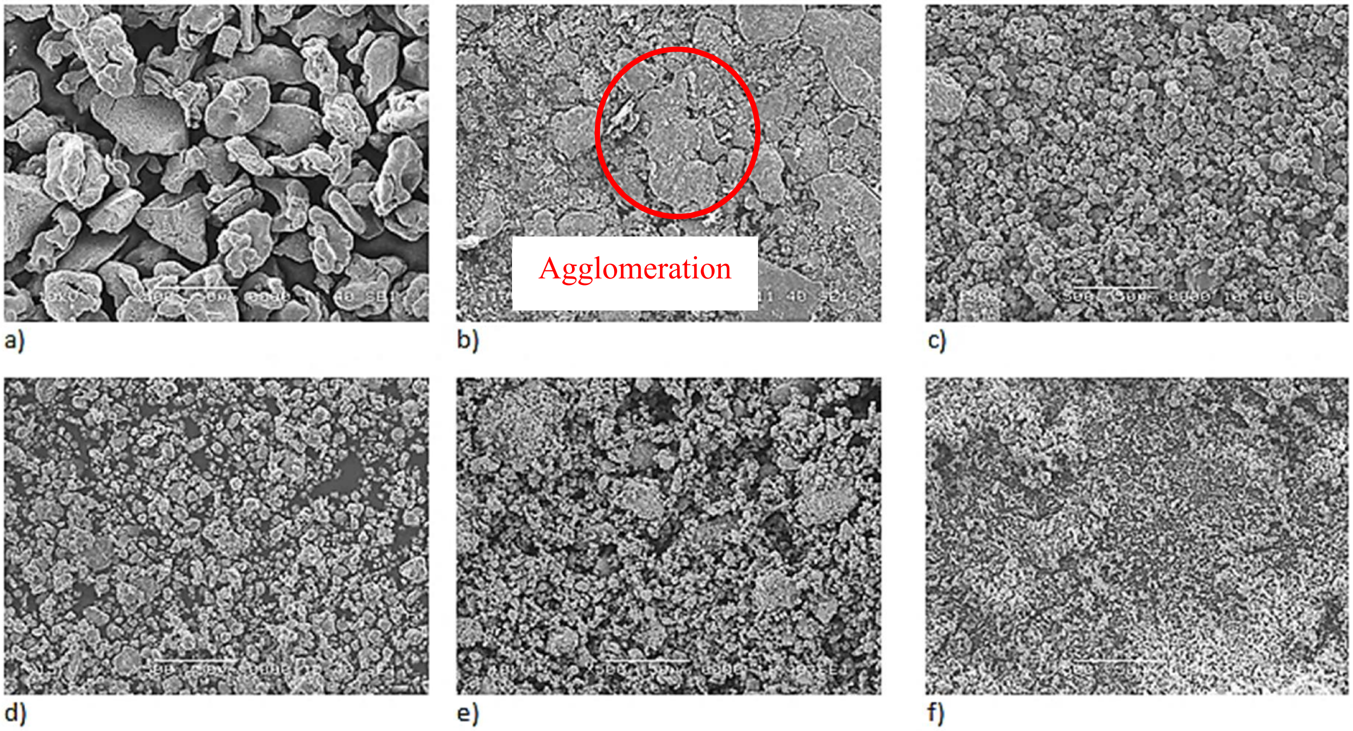

Figure 4.33: SEM morphology of Fe_{73} -Cr_{18} –Ni_{9} –Si_{2} milled powders, a) 0 h, b)20 h, c) 60 h, e)100 h, f)160 h, E) 160 h milled and annealed at 1100 °C

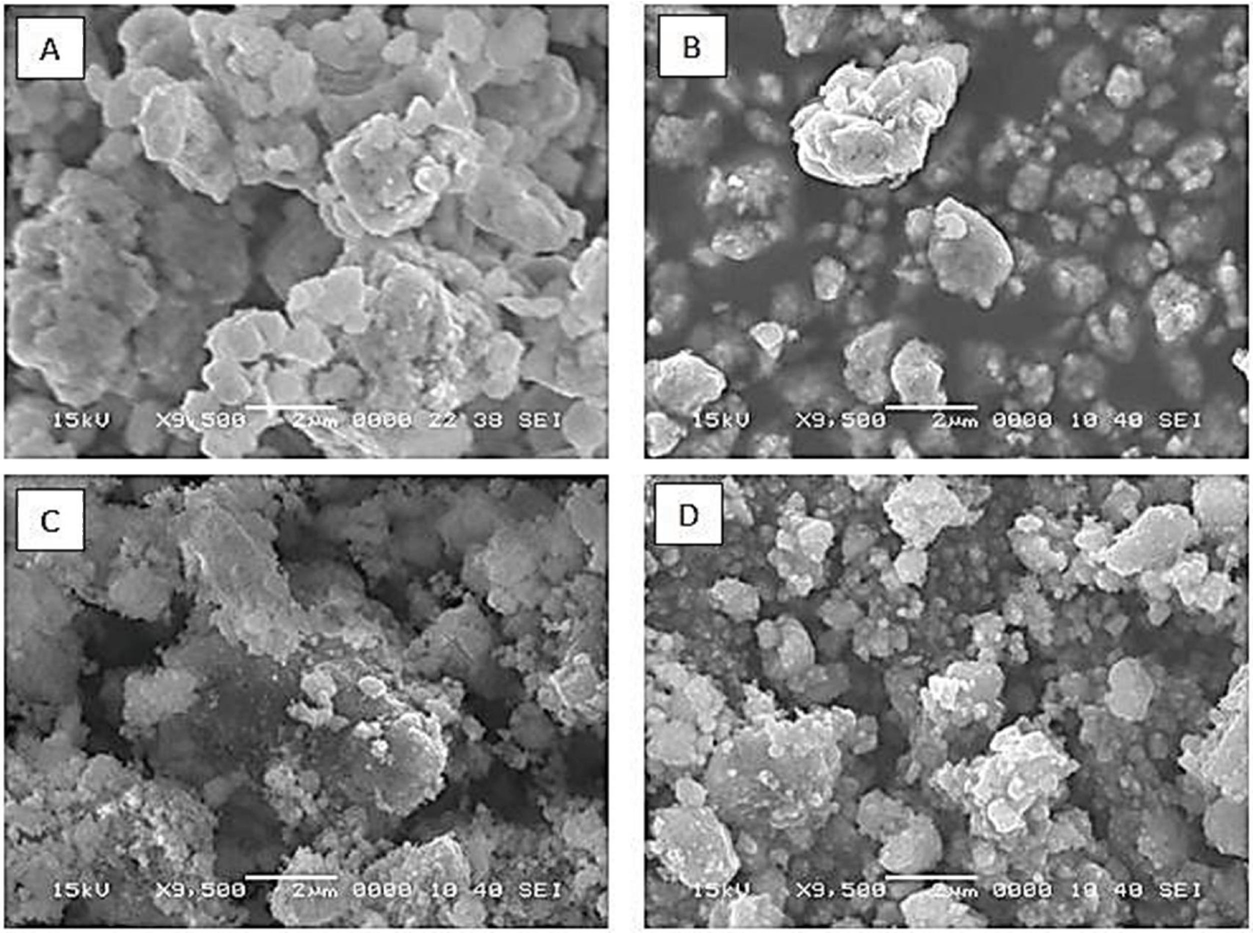

Figure 4.34: Effect of Si on the powder morphology of 160 h milled and subsequently annealed at 1100 °C

4.2.1.4. Lattice parameter and crystallite size calculations

Fig. 4.35 shows the variation of lattice parameter of $Fe_{(73-x)}Cr_{18}Ni_9Si_x$ (x = 0 & 2) alloys milled at 5, 10, 160 h-annealed. The variation of lattice parameter can be explained by keeping in the mind Fig. 4.30 where there is the formation of α-phase at 5 and 10 h and γ-phase after annealing of 160 h powder. The formation of α-phase at 5 h of milling resulted in the decrease in lattice parameter (as Fe(110) peak shifted towards higher angles) due to solid solution formation. This decrease is lattice parameter is due to the fact that, Ni have smaller atomic radius as compare to Fe and its dissolution will dilate the lattice. After 10 h milling, Fe(110) peak shifted toward smaller angles indicating the increase in lattice parameter which is due to the dissolution of bigger atomic radius solute atoms i.e. Cr into Fe. Yousefi et al. [52] also reported the variation of lattice parameter due to dissolution of bigger atomic radius Co in Fe. They also reported the dissolution of smaller atomic radius Si in Fe dilate the lattice parameter. The annealing of amorphous powder at 1100 °C, resulted in the formation of FCC structure (γ-phase) having lattice parameter greater than BCC-α-phase. The same kind of trend has been reported by F.Tehrani et.al [78]. Fig. 4.32 also shows that, the powders having 2 % Si content has smaller lattice parameter as compare to that of 0 % Si which is due to the fact that, Si has atomic radius smaller than that of Fe.

Fig. 4.36 shows the effect of Si content on the lattice parameter of 160 h milled powder after annealing in Argon atmosphere at 1100 °C. Results showed that the sample with 3 % Si has the lattice parameter of about 0.328 nm. Lattice parameter calculations done by the SAD pattern of 160 h-annealed powder showed 0.3278 nm which is very close to that of calculations done by XRD.

The crystallite size of milled powders during milling and alloy powders after 160 h milling has been calculated using famous Williamson Hall equation(β_{hkl} $\cos\theta = K\lambda/D + 4\varepsilon\sin\theta$). Fig. 4.37 shows the effect of milling time on the crystallite size variation of $Fe_{(73-x)}Cr_{18}Ni_9Si_x$ (x = 0 & 2) during milling. In early stages of milling (till 10 h) there was a drastic decrease in crystallite size. The reduction of crystallite size was more drastic in case of $Fe_{71}Cr_{18}Ni_9Si_2$. The drastic decrease in crystallite size is because of the brittleness imparted by Si. The same kind of trend of decrease in crystallite size has been reported elsewhere [52]. Fig. 4.38 shows the effect of Si content on the change in crystallite size of 160 h-annealed milled powder.

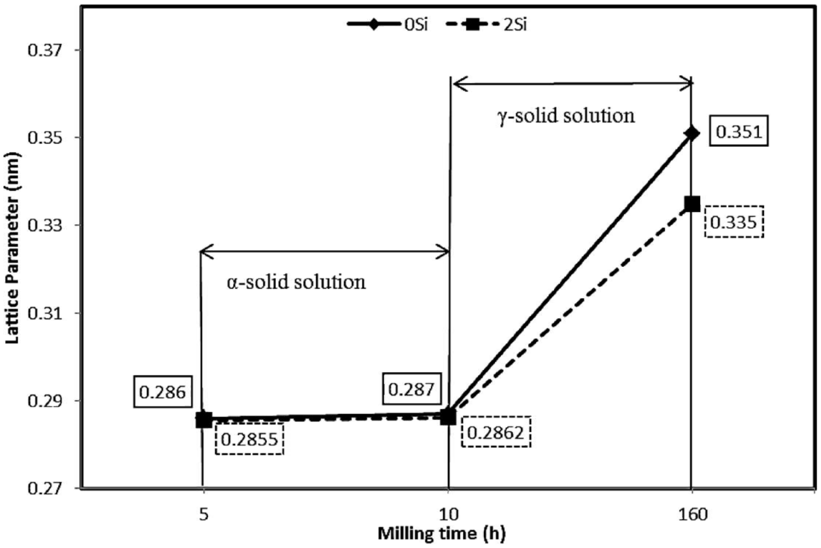

Figure 4.35: Lattice parameter variation of $Fe_{(73-x)}$-Cr_{18}-Ni_9-Si_x (x = 0, 2) alloy with milling time

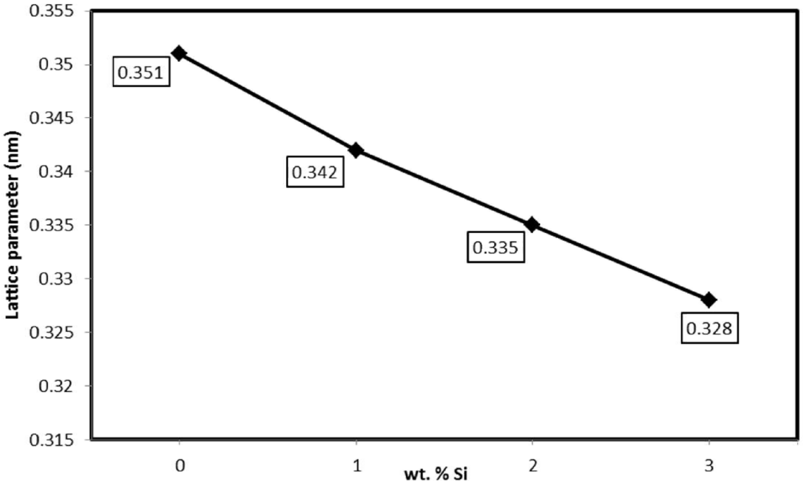

Figure 4.36: Lattice parameter variation of $Fe_{(73-x)}$-Cr_{18}-Ni_9-Si_x (x = 0, 1, 2, 3) alloy milled for 160h and annealed at 1100 °C

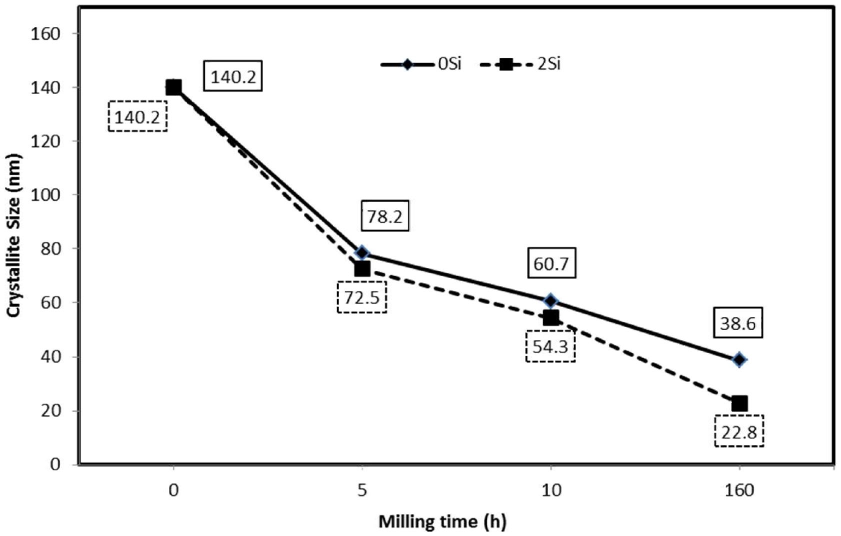

Figure 4.37: Crystallite size variation of $Fe_{(73-x)}$ -Cr_{18} -Ni_9-Si_x (x = 0, 2) alloy with milling time.

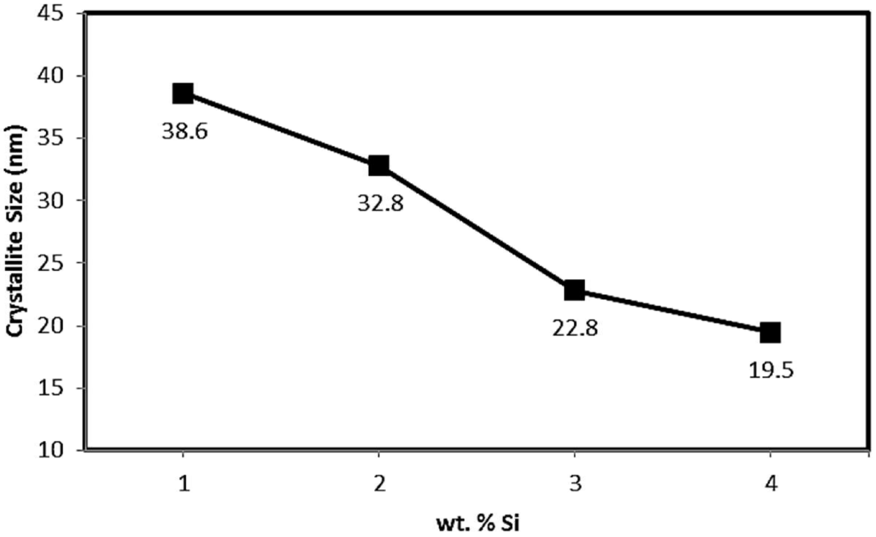

Figure 4.38: Crystallite size variation of $Fe_{(73-x)}$-Cr_{18}-Ni_9 -Si_x (x = 0, 1, 2, 3) alloy milled for 160h and annealed at 1100 °C

4.2.2. SPS of ball milled $Fe_{(73-x)}$-Cr_{18}-Ni_9-Si_x (x = 0, 1, 2, 3) alloys

Spark plasma sintering of nano-structured $Fe_{(73-x)}$-Cr_{18}-Ni_9-Si_x (x = 0, 1, 2, 3) powder was carried out on the optimized parameters as discussed in section 4.1.2. XRD of the sintered specimen was carried out to investigate the evolution of phase/phases after sintering and FE-SEM was carried out to study the microstructure.

4.2.2.1. Characterization of sintered alloys

Fig. 4.39 shows the XRD spectrum of $Fe_{(73-x)}Cr_{18}Ni_9Si_x$(x = 0, 1, 2, 3) sintered alloys XRD results show that, there is an unexpected formation of α- phase along with γ-phase after sintering.

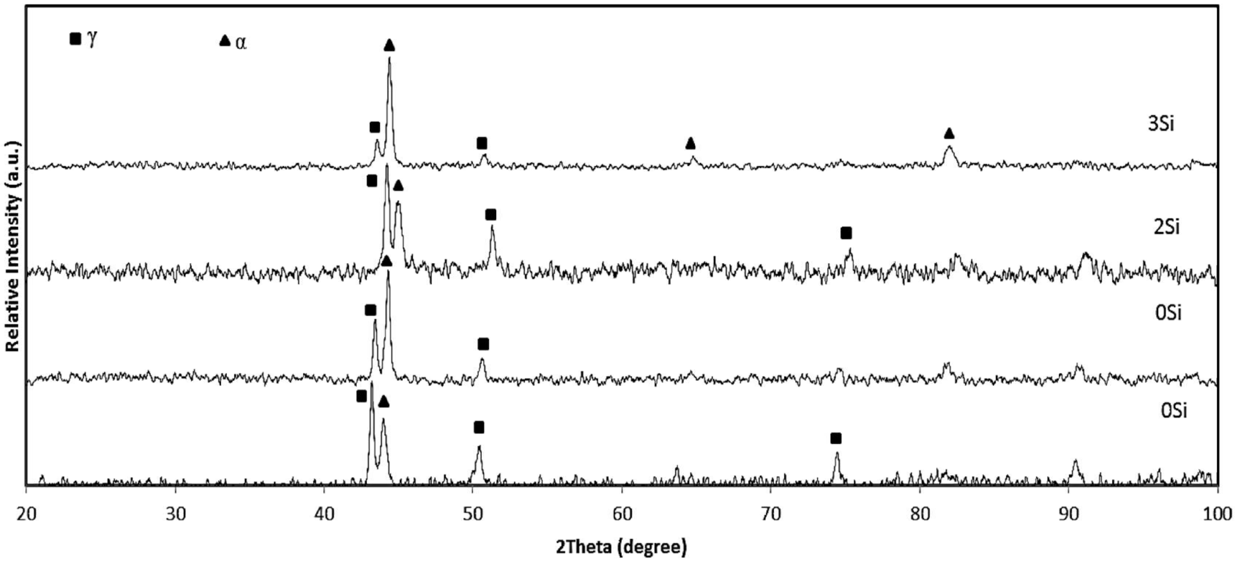

Figure 4.39: XRD spectra of $Fe_{(73-x)}Cr_{18}Ni_9Si_x$(x = 0, 1, 2, 3) Spark Plasma Sintered samples

Fig.4.40 shows the BSE-SEM images of $Fe_{(73-x)}Cr_{18}Ni_9Si_x$(x = 2) sintered alloy etched with Villela's reagent. The contrast in BSE-SEM image confirmed the variation of composition in dark and grey regions. Fig A) show the BSE image and confirm the compositional variation in the black and grey regions. Point EDX analysis revels that, the black regions are rich in Cr and grey regions are rich in Fe. Ni and Si are homogenously distributed throughout the matrix.

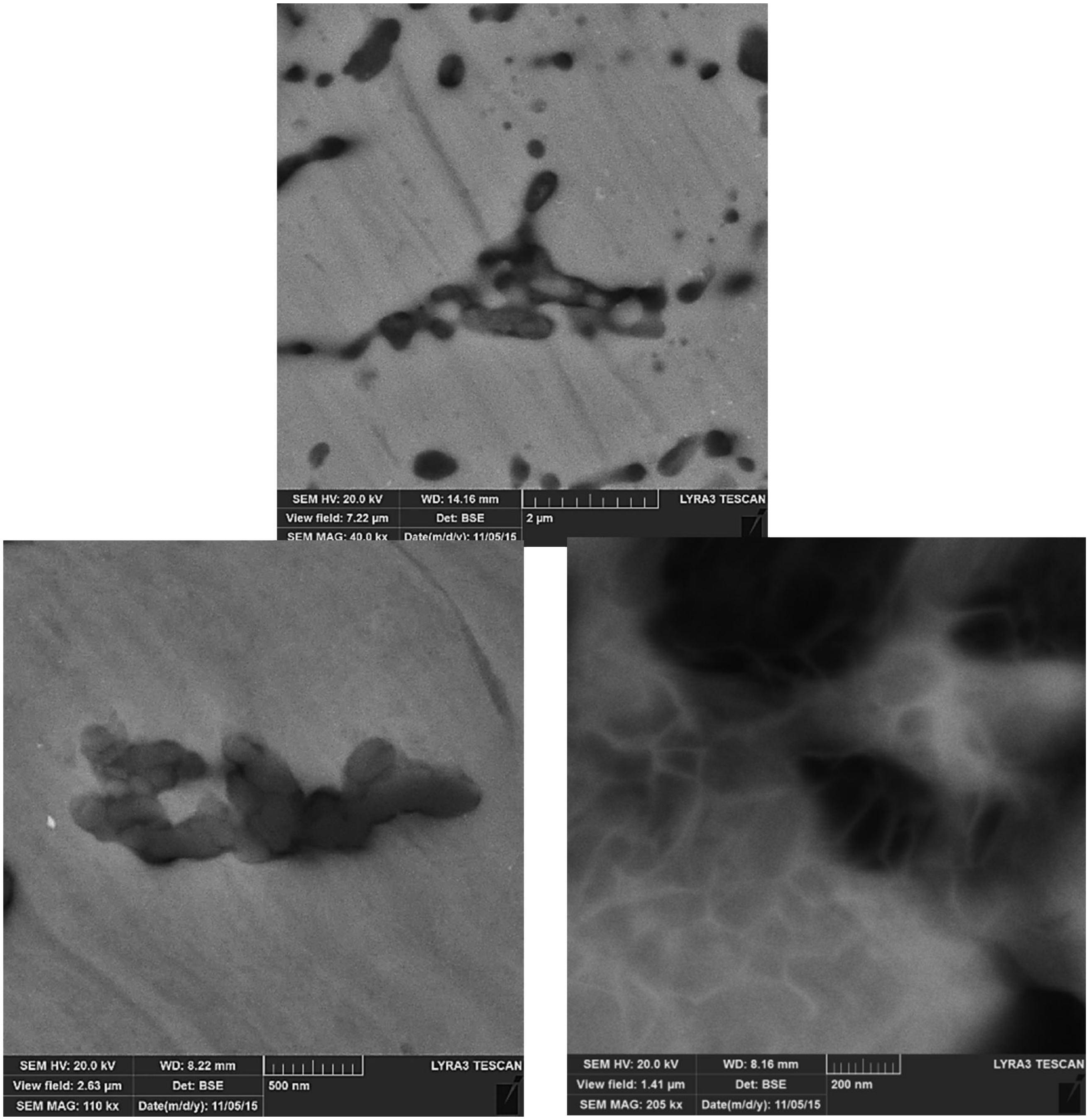

Figure 4.40: BSE-SEM morphology of $Fe_{(73-x)}Cr_{18}Ni_9Si_x$(x = 2) sintered specimen A) BSE image showing the compositional contrast. B) Magnified image of the black precipitates C) Magnified image showing the grain size.

4.2.2.2. **Densification and micro-hardness calculations**

Sintered density was calculated by Archimedes' principle and micro-hardness was obtained by using Bheuler micro-vicker. Fig. 4.41 (a & b) illustrats the effect of wt % Si on the micro-hardness and densification of $Fe_{(73-x)}$-Cr_{18}-Ni_9-Si_x($x = 0, 1, 2, 3$). The results show that, as the Si content in the specimen increases, hardness and densification increases as well.

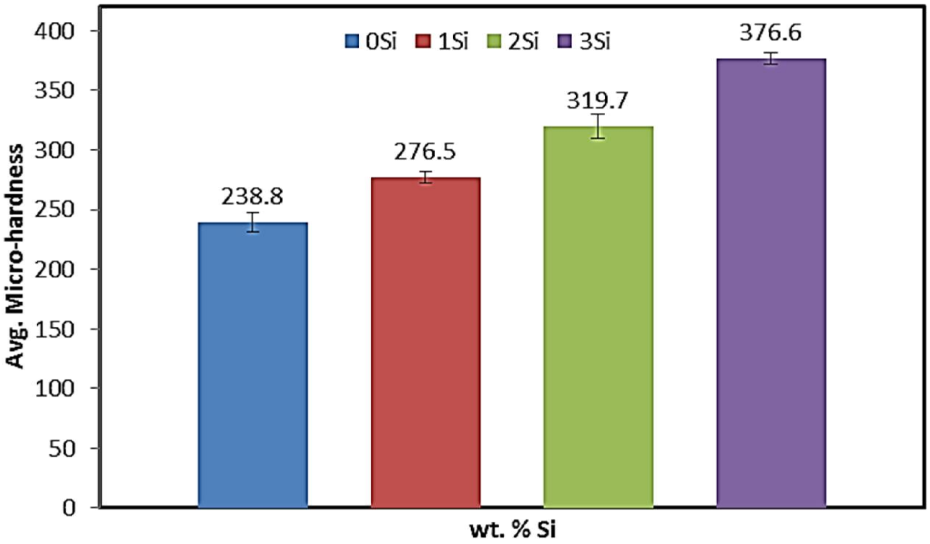

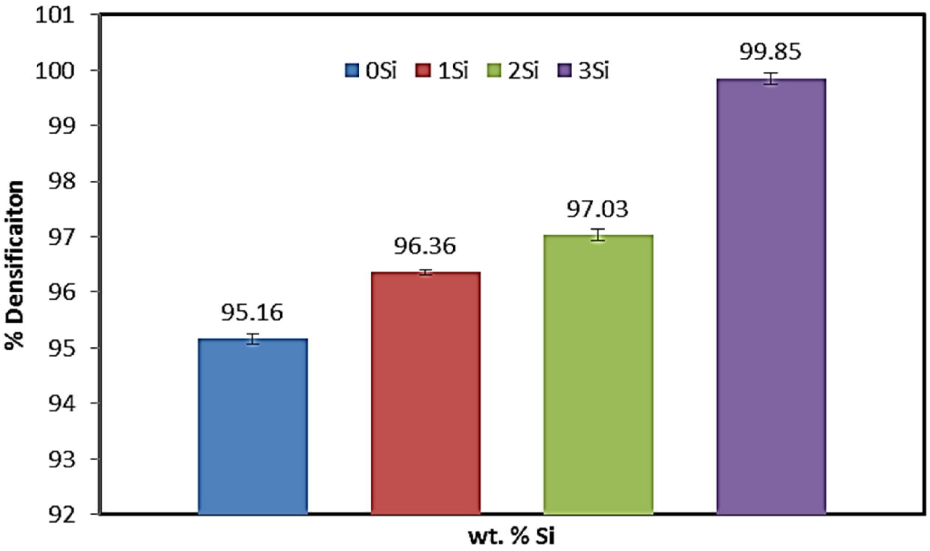

Figure 4.38: Effect of Si content on micro hardness and densification of $Fe_{(73-x)}$-Cr_{18}-Ni_9-Si_x(x = 0, 1, 2, 3) alloys prepared by SPS

4.2.3. Effect of Si content on the corrosion properties

In this section, we studied the effect of Si content on the electrochemical properties of $Fe_{(73-x)}$-Cr_{18}-Ni_9-Si_x(x = 0, 1, 2, 3) sintered alloys by PDP, LPR and EIS. These EC investigations have been carried out in 0.2M NaCl and 0.5M H_2SO_4 solutions under deaerated environment at room temperature. A conventional three electrode system was used with sample under investigation acted as working electrode, graphite rod as counter and SCE as reference electrode. The system was deaerated by purging N_2 for 15min and the flow was maintained during the experiment. The area exposed during testing was 0.1cm^2.

4.2.3.1. Potentiodynamic polarization (PDP)

PDP tests were conducted by swiping the voltage from -0.65 to 1.2 mV_{SCE} at the scan rate of 0.2mV/sec under deaerated environment at room temperature. Fig. 4.41 (a & b) shows PDP response of $Fe_{(73-x)}$-Cr_{18}-Ni_9-Si_x(x = 0, 1, 2, 3) in 0.2M NaCl and 0.5M H_2SO_4 solution respectively. Different parameters [Epit (pitting potential), i_{corr} (corrosion current density), i_p (passive current density), Ecorr (corrosion potential)] were calculated and have been summarized in Table 4.6.

From Fig. 4.41 & Table. 4.6, it can be inferred that addition of Si does not have a significant effect on the improvement of E_{corr} as well as on i_{corr} of sintered alloys. The PDP response of sample with 0 %Si in 0.2M NaCl solution shows that, the sample does not exhibit a stable passive film but addition of only 1% Si significantly improved the corrosion resistance as the sample exhibit a passive layer and i_p was significantly reduced. Passive current density (i_p) calculated at 19.42mV (in 0.2M NaCl) was highest for sample with 0% Si (4400 nA) and sample with 2% Si exhibited the lowest (134.2 nA). PDP response of $Fe_{(73-x)}$-Cr_{18}-Ni_9-Si_x(x = 0, 1, 2, 3) samples in 0.5M H_2SO_4 solution showed that, sample with 0% Si do exhibit a stable passive film but i_p value was very high (224.2 μA) as compare to that of sample with 1% Si (i_p = 5.377 μA). So it can be said that, sample with 3% Si have the highest corrosion resistance in terms of passive current density as it has the lowest i_p value (1.42 μA). Lowest i_p value inferred that, sample with 3% Si exhibit the most protective passive film which is able to protect the sample under these conditions.

It can also be inferred that, addition of Si improved the pitting potential (E_{pit}), which is the most important parameter to study the corrosion properties of SSs. Epit was highest (259.6 & 917.2 mV in 0.2M NaCl and 0.5M H_2SO_4 solution respectively) for sample with 3wt % Si as compare to other samples. High E_{pit} values indicate that, the sample with 3% Si is most resistant to localized corrosion under these conditions.

Many authors reported the positive effect of Si content on the corrosion properties of SSs. Velasco et al. [15] compared the Icorr values of the alloy prepared by PM having Si content with commercially produced cast alloy without Si content. Despite the fact that cast alloys are dense as compare to that of sintered alloys, they observed that Si has the beneficial effect on the corrosion properties. Toor et al. [20] investigated the effect of Si content on 304 and 304Si SSs and reported that Si has a pronounced positive effect on the Epit of the alloys. Nishimura et al. [28] deposited the Si on the SUS 304 SSs and studied the effect of Si on the pitting corrosion resistance and crevice corrosion resistance. They found out that, Si enhanced both the pitting corrosion and crevice corrosion resistance as compare to that of simple SUS 304 SSs. Tasi et al. [67] studied the effect of Si content on the corrosion resistance of 304 sintered SSs. They reported the formation of SiO_2 layer on the surface of the sample having Si content which helps in improving the corrosion resistance as compare to the sample without Si. So, now it is established that, the reasons for the improvements in the corrosion resistance of Si containing SSs is because of the presence of Si in the passive layer. Robin et al. [69] developed the correlation between the composition of the passive layer and the corrosion resistance of SSs with Si content. The XPS studies of the passive layer revealed that, Si is present in the passive layer in large amount.

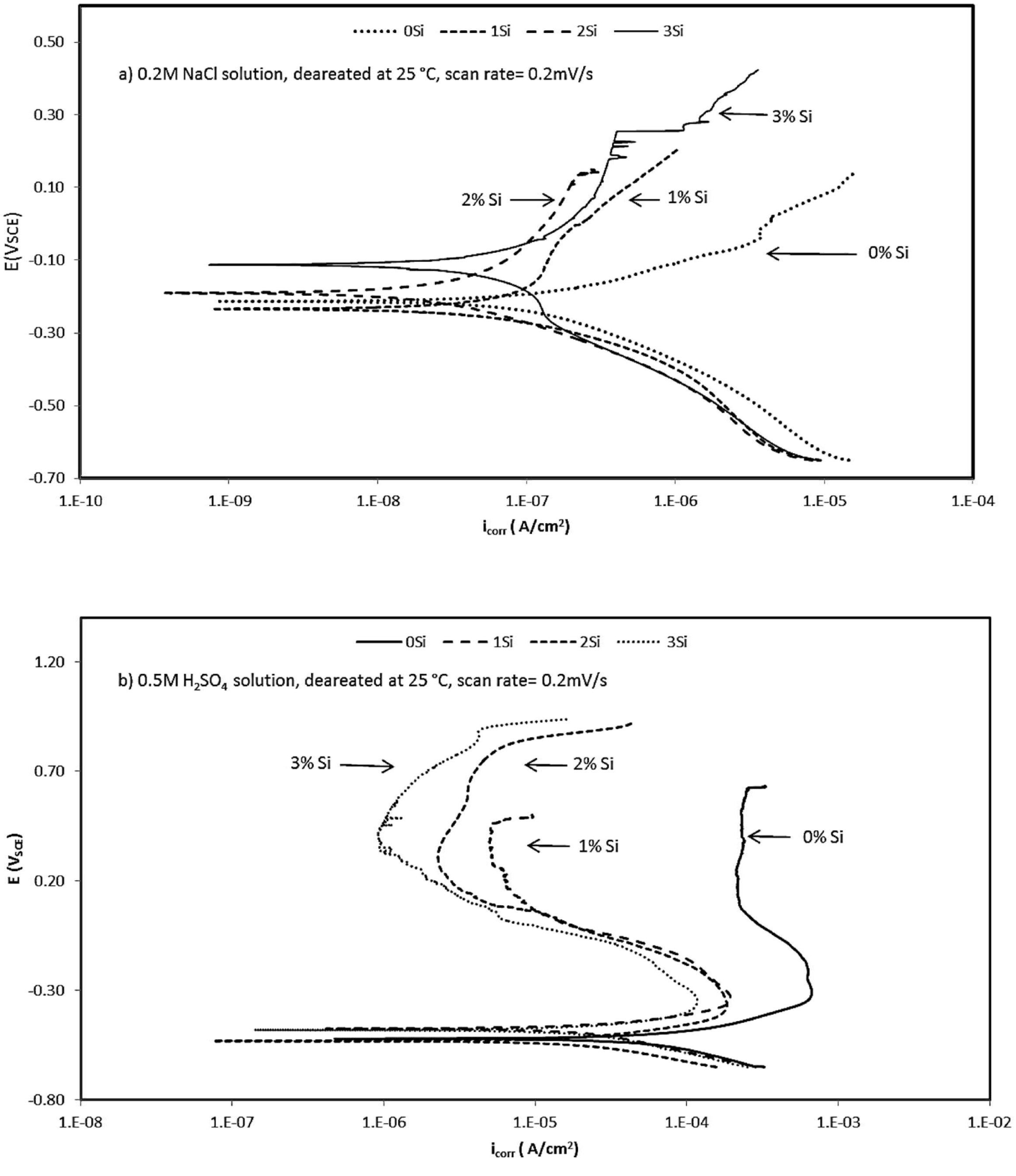

Figure 4.41: Potentiodynamic polarization response of $Fe_{(73-x)}$-Cr_{18}-Ni_9-Si_x(x = 0, 1, 2, 3) sintered alloys a) 0.2M NaCl b) 0.5M H_2SO_4 solution.

Table 4.7: Summary of PDP response of of Fe(73-x)-Cr18-Ni9-Six(x = 0, 1, 2, 3) in 0.2M NaCl and 0.5M H2SO4 solution

Electrolyte	***0.2M NaCl***					***0.5M H_2SO_4***				
Sample	E_{corr}	I_{corr}	E_p	E_{pit}	i_p	E_{corr}	I_{corr}	E_p	E_{pit}	i_p
	mV	***pA***	***mV***	***mV***	***nA***	***mV***	***nA***	***mV***	***mV***	***µA***
0%Si	-231.6	867.5	19.42	N/A	4400	-521.8	474.2	286	631.1	224.2
1%Si	-233	773.3	19.42	12.14	279.2	-475.2	472.1	286	461.1	5.377
2%Si	-173.5	565.2	19.42	134.2	146.8	-550	356.2	286	805.8	2.48
3%Si	-104.4	739.2	19.42	259.6	217.2	-481	142.89	286	917.2	1.428

Linear polarization resistance (LPR)

LPR was conducted by swiping the potential from -0.02 to 0.02V at the scan rate of 0.3 mV/sec in deaerated environment at room temperature.

Fig. 4.42 (a & b) shows the LPR response of $Fe_{(73-x)}$-Cr_{18}-Ni_9-Si_x(x = 0, 1, 2, 3) sintered alloys in 0.2M NaCl and 0.5M H_2SO_4 solutions respectively. It can be inferred from the Fig that the sample having high wt% Si content (3%) have high Rp value while the sample having low % Si (0%) have low Rp value. As Rp value is a direct measure of the corrosion resistance of the material, so it is clear that Si improves the corrosion resistance of the material.

LPR is a very useful tool in measuring the corrosion resistance of the steels. Many researchers have used this technique to investigate the effect of different environments on the corrosion resistance of steels. Vuković et al. studied the inhibition effect of Thiobacillus ferrooxidans Bacteria on the corrosion of steel by LPR technique [70]. Choi et al. studied the corrosion behavior of carbon steel and weathering steel in aerated acidic chloride solution by using weight loss and LPR technique [99].

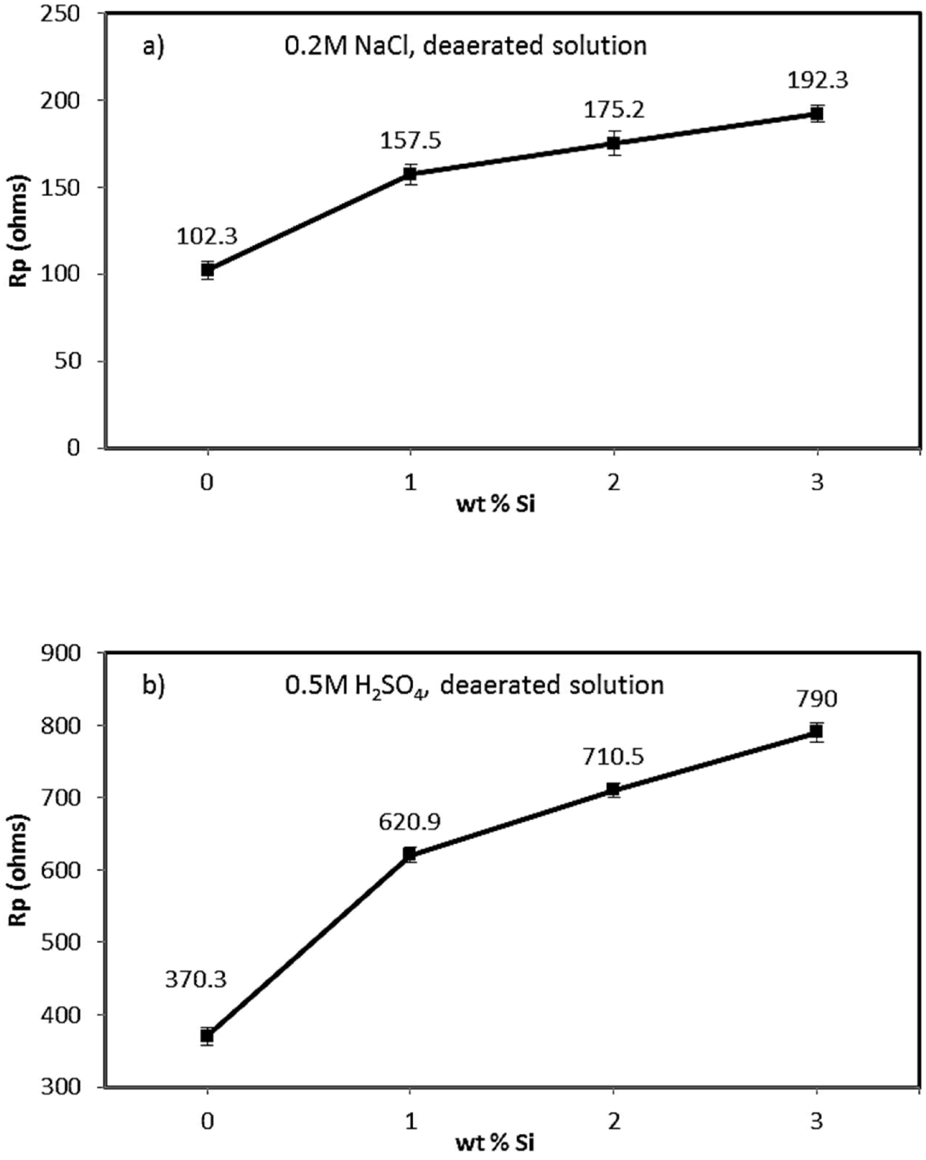

Figure 4.42: Effect of wt% Si content on the Rp value a) 0.2M NaCl b) 0.5M H_2SO_4 solutions

4.2.3.2. Electrochemical impedance spectroscopy (EIS)

Electrochemical impedance Spectroscopy was carried out at 0.05 and 0.35 DC voltage in 0.2M NaCl and 0.5M H_2SO_4 solutions respectively. The voltage was selected from polarization curves and it lies in the passive region of all the samples. Before conducting the test, a passive film was formed for 30min.

Nyquist plot (Fig. 4.42 a & b) have been drawn to show the effect of Si content on the electrochemical properties $Fe_{(73-x)}$-Cr_{18}-Ni_9-Si_x($x = 0, 1, 2, 3$) sintered alloys. The diameter of the Nyquist plot (semi-circle) is a direct function of the corrosion resistance of the samples and it can be said that, the sample having larger diameter will have high corrosion resistance. Fig shows that, $Fe_{(73-x)}$-Cr_{18}-Ni_9-Si_x($x = 3$) have the highest diameter semi-circle as compare to other samples $Fe_{(73-x)}$-Cr_{18}-Ni_9-Si_x($x = 0, 1, 2$). To fit the EIS spectra, CPE model (shown in Fig. 4.27) has been used and the results have been given in Table 4.7.

Generally, electrochemical impedance spectroscopy is used to study the stability of passive film of Stainless steels. Many authors used this technique to study the behavior of passive films of different alloys in different conditions. Jinlong et al. studied the effect of grain size on the corrosion behavior of 304SSs by using EIS in borate buffer solution and reported that, nano-crystalline 304SSs have a semi-circle with much higher diameter as compare to micro-crystalline 304SSs [71]. Garcia et al. studied the passivation behavior of austenitic and duplex SSs by using EIS technique in pore solution [72].

Table 4.7: Summary of EIS results of $Fe_{(73-x)}$-Cr_{18}-Ni_9-Si_x(x = 0, 1, 2, 3) alloys obtained after curve fitting by CPE model

sample name	***0.2M NaCl***			***0.5M H_2SO_4***		
	Rp	***Rs***	***CPE***	***Rp***	***Rs***	***CPE***
	(Ohm)	***(Ohm)***	***$\mu F/cm^2$***	***(Ohm)***	***(Ohm)***	***$\mu F/cm^2$***
0% Si	214.5	33.18	1.67E-01	2.34E+03	24.03	5.67E-01
1% Si	1.87E+03	21.07	1.10E-01	2.61E+03	28.67	1.99E-01
2% Si	2.61E+03	33.81	1.99E-01	5.65E+03	28.46	1.64E-01
3% Si	5.65E+03	28.46	1.64E-01	9.74E+03	33.81	7.11E-01

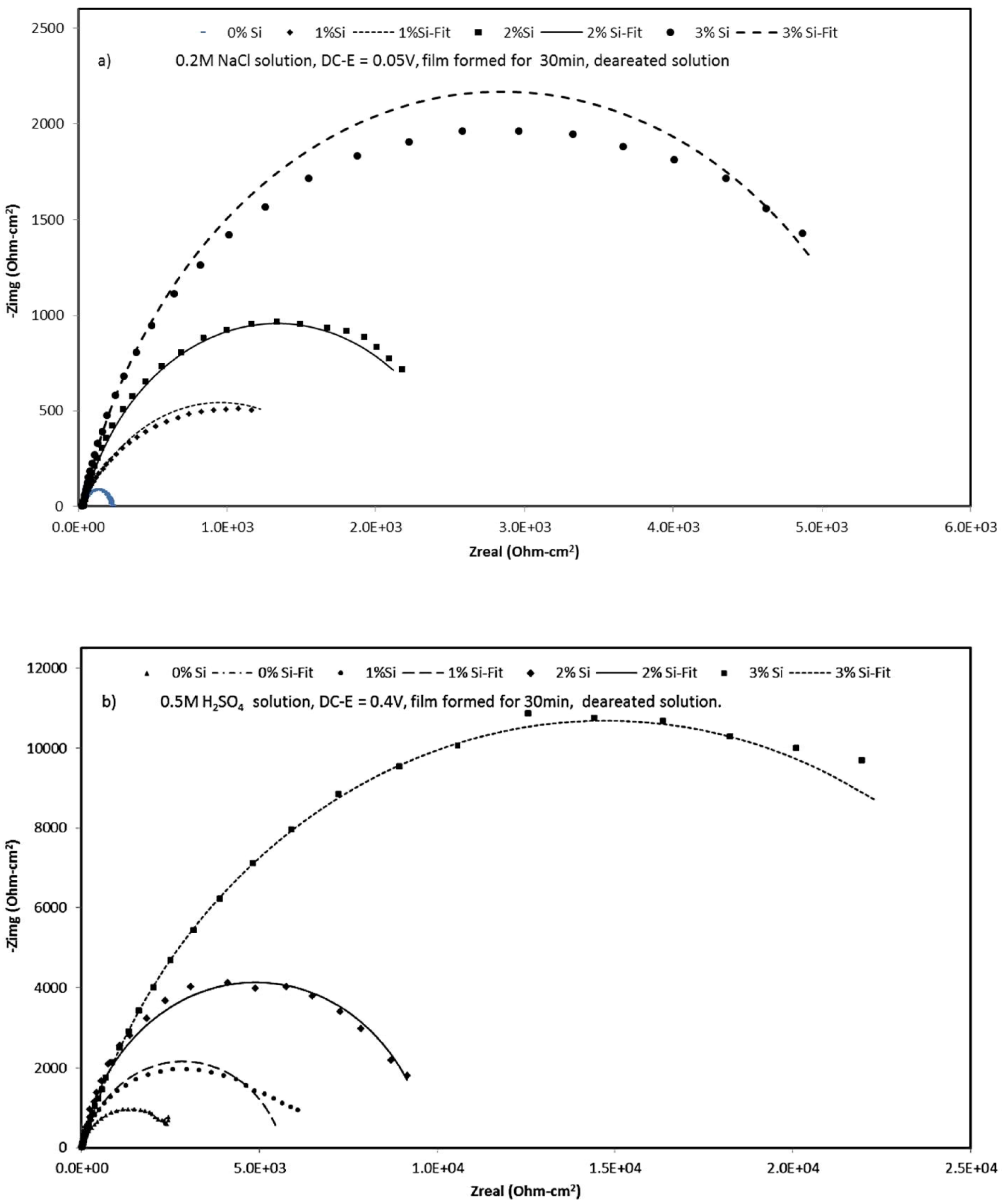

Figure 4.43: Nyquist spectra showing the effect of Si content on the corrosion resistance a) 0.2M NaCl b) 0.5M H_2SO_4 solutions

It is believed that, the corrosion rate of PM SSs is higher than that of cast counter parts. [80]. The occurrence of the phenomenon is linked with the development of localized solutions with concentration different than the overall electrolyte inside of the pores. Huge number of pores favors the establishment of differential airing cavities and differential concentration of protons. In pores acting as cracks, a point is reached where O_2 is being used up while the ventilated zones of the surface have an adequate access to this O_2. Under these circumstances, the Ecorr in the ventilated zone of the pore is maintained above that of passivation and consequently the passive layer remains stable in that areas while in O_2 deficient regions inside the pores, an active-passive cells are set up.

The formations of cracks, leading to corrosion in PM SSs, come into being with the release of metallic ions, principally Cr, inside of the pores. Then a hydrolysis reaction leads to the acidification of the pore. [80]. Eq. 1 shows the formation of acid due to hydrolysis inside of the pore

$$Cr^{3+} + 3H_2O \longleftrightarrow Cr(OH)_3 + 3H^+ \qquad \text{Eq.1}$$

The crack/pore geometry is the most important controlling factor in this type of corrosion. By taking into account the efficiency in generating the phenomenon of crevice corrosion, these types of crevices can be classified as per their degree of narrowness and their depth. In case of PM materials, in which pore is very narrow, the volume of electrolyte to be deoxygenated and acidified inside the pore is very small. This will lead to the initiation of attack which will be both rapid and severe. When the proton concentration is quit high to put the material in the corrosion zone of the Pourbaix diagram, the passive layer get dissolved and attack move towards the inner side of the pore. This phenomenon is explained in the Fig.4.44 (A & B). At next stage, the attack progress towards the interior of PM SSs by means of basic mechanisms. While on the other hand, the established active-passive cells resulted in the disintegration of particles. This step has been shown in Fig. 4.44 C.

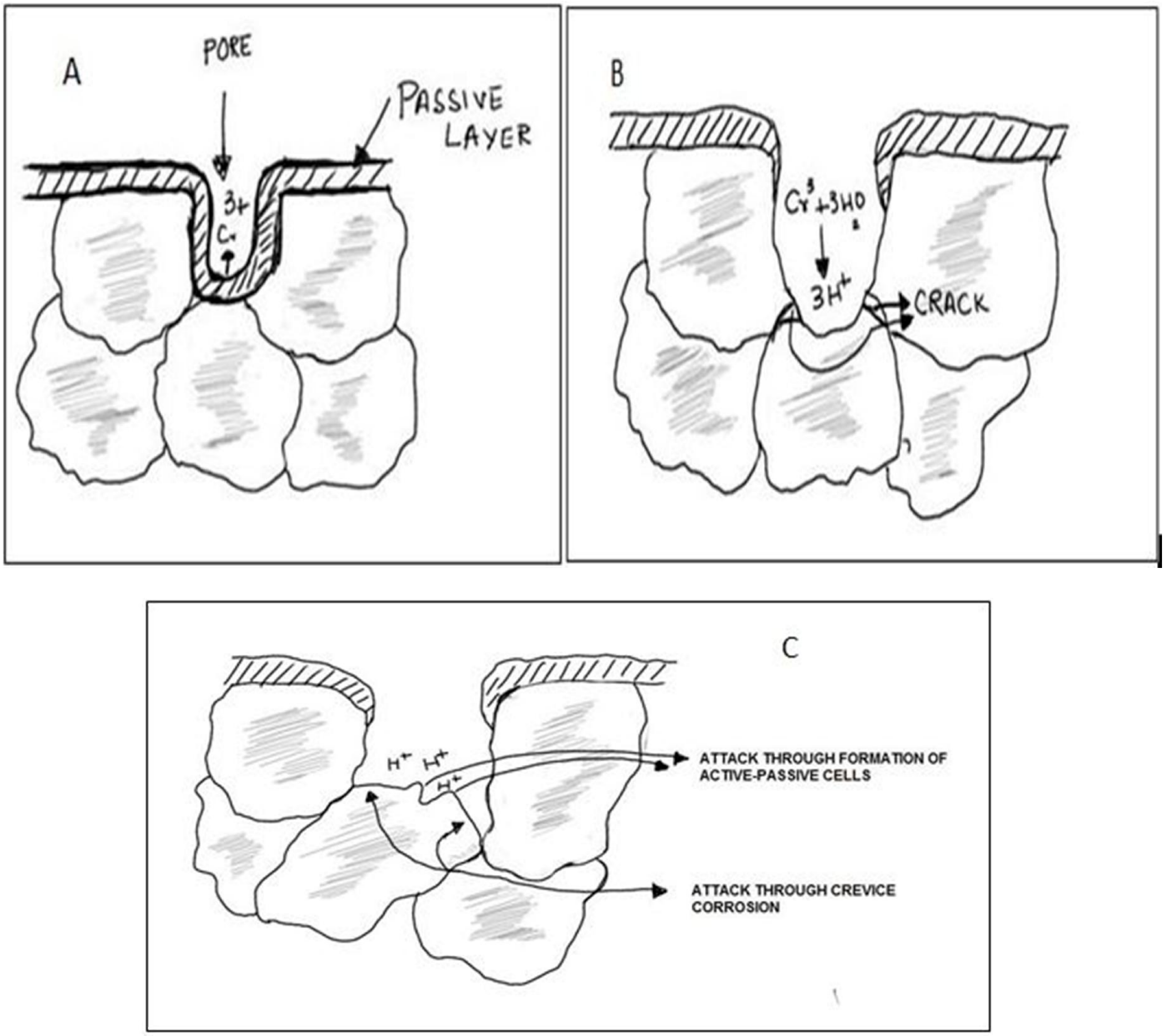

Figure 4.44: Corrosion mechanism of PM SSs, a) Porosity having the passive layer, b) Acidification of the pore leading to the formation of H+ ions in the pore, c) Crevice corrosion because of the acidification

CHAPTER 5

CONCLUSIONS

Ferritic and Austenitic stainless steels were developed by mechanical alloying of pure elemental powders using planetary ball mill followed by spark plasma sintering. Spark plasma sintering process parameters (temperature, holding time, applied pressure, heating rate) were optimized to obtain high densification. Electrochemical properties of spark plasma sintered alloys were investigated at room temperature under Cl^{-1} and SO_4^{-1} solutions. Following are the conclusions drawn from current study regarding development, characterization and electrochemical investigation of $Fe_{(82-x)}$-Cr_{18} -Si_x and $Fe_{(73-x)}$-Cr_{18} –Ni_9-Si_x (x = 0, 1, 2, 3) alloys.

$Fe_{(82-x)}$-Cr_{18}-Si_x alloy system,

- Mechanical alloying (MA) of pure elemental powders lead to the formation of solid solution at early stages of milling. Continued milling resulted in the formation of amorphous phase which lead to mechanical crystallization upon milling at higher milling time.
- Formation of solid solution, amorphous phase formation and mechanical crystallization had been studied by XRD and TEM.
- Lattice parameter, crystallite size and lattice strain calculations showed that, with the increase in wt. % Si, lattice parameter, crystallite size decreased while lattice strain increased.

- SEM images of powders showed different morphologies at different times. Cold welding/agglomeration was predominant at early stages of milling while at higher milling times, the fracture mechanism was predominant.
- Sintering process parameters (temperature, holding time, heating rate and applied pressure) were optimized, on Fe_{80}-Cr_{18}–Si_2, to obtain maximum densification.
- Sintering temperature was varied as 900, 1000, 1100 and 1200 °C, while holding time was fixed at 10 min, heating rate at 100 degree/min and applied pressure at 50 MPa. Densification results showed that, 1100 °C demonstrated highest value.
- Holding time was varied as 5, 10 and 15 min by keeping sintering temperature fixed at 1100 °C, heating rate at 100 degree/min and applied pressure at 50 MPa. Densification results showed highest value at 15 min holding.
- Heating rate was varied as 100 and 50 degree/min while applied pressure varied as 50, 60 and 70 MPa by keeping sintering temperature fixed at 1100 °C, holding time at 15 min. Densification results showed highest value with 60 MPa of pressure. So, it is concluded that, 1100 °C temperature, 15 min holding, 50 degree/min holding and 60 MPa pressure are the optimized parameters.
- XRD results of samples sintered at different conditions showed the BCC α-phase at all conditions.
- Crystallite size calculations of sintered alloys revealed maximum size of 29.02 nm at optimized conditions.
- Electrochemical investigations of samples sintered at different parameters showed that, with the increase in densification, corrosion resistance increased. The sample with highest densification (96.0 %) showed best corrosion resistance in terms of

highest pitting potential, lowest corrosion current density. Maximum polarization resistance and highest impedance was also observed by very sample.

- $Fe_{(82-x)}$-Cr_{18}-Si_x (x = 0, 1 & 3) were sintered at optimized conditions. Densification and hardness results showed that, with the increase in wt. % Si, densification and hardness increased.
- Electrochemical investigation of samples with varying wt. % Si showed that, with the increase in Si content, corrosion resistance increased in terms of noble corrosion potential, low corrosion current density, high pitting potential and low passive current density.
- Highest polarization resistance and impedance was shown by 3 wt. % Si sample.

$Fe_{(73-x)}$-Cr_{18} –Ni_9-Si_x alloy system,

- MA of pure Fe, Cr, Ni and Si powders led to the development of α-solid solution at early stages of milling which transformed into an amorphous phase on further milling. The amorphous phase formed during milling did not show crystallization even at very high milling time (160 h)
- Annealing of 160 h milled powder at 1100 °C for 1h in argon atmosphere transformed the powder into γ-solid solution.
- Development of α-solid solution, amorphous phase and γ-solid solution was confirmed by XRD and TEM/SAD.
- Lattice parameter and crystallite size both decreased with the increase in wt. % Si.
- $Fe_{(73-x)}$-Cr_{18}–Ni_9-Si_x (x = 0, 1, 2, 3) milled powders were sintered at optimized parameter.

- Densification and hardness results showed that, increase in wt. % Si resulted in increase in densification and hardness.
- Electrochemical investigation of samples with varying wt. % Si showed that, with the increase in Si content, corrosion resistance increased in terms of noble corrosion potential, lower corrosion current density, higher pitting potential and lower passive current density.
- Highest polarization resistance and impedance was shown by 3 wt. % Si sample.

REFERENCES

[1] D.D. Macdonald, Passivity–the key to our metals-based civilization, Pure Appl. Chem. 71 (1999) 951–978.

[2] P. Cunat, Alloying elements in stainless steel and other chromium-containing alloys, Int. Chromium Dev. Assoc. (2004) 1–24.

[3] C.-O.. Olsson, D. Landolt, Passive films on stainless steels—chemistry, structure and growth, Electrochim. Acta. 48 (2003) 1093–1104.

[4] R.K. Gupta, N. Birbilis, The influence of nanocrystalline structure and processing route on corrosion of stainless steel: A review, Corros. Sci. 92 (2015) 1–15.

[5] R.J. Causton, C. Mumau, T.M. Cimino, PM stainless steels uses in automotive exhausts, Met. Powder Rep. 53 (1998) 22–26.

[6] K.H. Lo, C.H. Shek, J.K.L. Lai, Recent developments in stainless steels, Mater. Sci. Eng. R Reports. 65 (2009) 39–104.

[7] M. Durand-Charre, The basic phase diagrams, Microstruct. Steels Cast Iron. (2004) 47–89.

[8] Sigma-phase in Fe-Cr and Fe-V alloy systems and its physical properties Faculty of Physics and Applied Computer Science , AGH University of Science and Technology , 30-059 Kraków , Poland Abstract, (n.d.) 1–27.

[9] K.S. Narasimhan, Recent Advances in Ferrous Powder Metallurgy, Adv. Perform. Mater. 3 (1996) 7–27.

[10] R.K. Gupta, J. Zhang, N. Birbilis, Oxidation resistance of nanocrystalline alloys, INTECH Open Access Publisher, 2012.

[11] K.D. Ralston, N. Birbilis, Effect of Grain Size on Corrosion: A Review, Corrosion. 66 (2010) 75005–75013.

[12] H.J. Fecht, Intrinsic instability and entropy stabilization of grain boundaries, Phys. Rev. Lett. 65 (1990) 610.

[13] H. Mehrer, Diffusion in Nanocrystalline Materials, Diffus. Solids Fundam. Methods, Mater. Diffus. Process. (2007) 593–620.

[14] R.K. Gupta, R.K.S. Raman, C.C. Koch, B.S. Murty, Effect of Nanocrystalline Structure on the Corrosion of a Fe20Cr Alloy, 8 (2013) 6791–6806.

[15] F. Velasco, A. Bautista, High-temperature oxidation and aqueous corrosion performance of ferritic , vacuum-sintered stainless steels prealloyed with Si, Corros. Sci. 51 (2009) 21–27.

[16] N. Cabrera, N.F. Mott, Theory of the oxidation of metals, Reports Prog. Phys. 12 (1949) 163.

[17] F.P. Fehlner, N.F. Mott, Low-temperature oxidation, Oxid. Met. 2 (1970) 59–99.

[18] T. Tsuru, R.M. Latanision, Corrosion Resistance of Microcrystalline Stainless Steels, J. Electrochem. Soc. 129 (1982) 1402–1408.

[19] W.F. Wang, M.J. Wu, Effect of silicon content and aging time on density, hardness, toughness and corrosion resistance of sintered 303LSC-Si stainless steels, Mater. Sci. Eng. A. 425 (2006) 167–171.

[20] I.-H. Toor, J. Kwon, H. Kwon, Effects of Si on the Repassivation Kinetics and SCC Susceptibility of Stainless Steels, J. Electrochem. Soc. 155 (2008) C495.

[21] N.D. Tomashov, G.P. Chernova, O.N. Marcova, Effect of supplementary alloying elements on pitting corrosion susceptibility of 18Cr-14Ni stainless steel, Corrosion. 20 (1964) 166t–173t.

[22] P.I. Marshall, G.T. Burstein, Effects of alloyed molybdenum on the kinetics of repassivation on austenitic stainless steels, Corros. Sci. 24 (1984) 463–478.

[23] A. Paúl, S. Elmrabet, L.C. Alves, M.F. da Silva, J.C. Soares, J.A. Odriozola, Ion microprobe study of the scale formed during high temperature oxidation of high silicon EN-1.4301 stainless steel, Nucl. Instruments Methods Phys. Res. Sect. B Beam Interact. with Mater. Atoms. 181 (2001) 394–398.

[24] R. Pettersson, L. Liu, J. Sund, Cyclic oxidation performance of silicon-alloyed stainless steels in dry and moist air, Corros. Eng. Sci. Technol. 40 (2005) 211–216. doi:10.1179/174327805X66254.

[25] J.S. Dunning, D.E. Alman, J.C. Rawers, Influence of silicon and aluminum additions on the oxidation resistance of a lean-chromium stainless steel, Oxid. Met. 57 (2002) 409–425.

[26] J.A. Poston, R. V. Siriwardane, J.S. Dunning, D.E. Alman, J.C. Rawers, X-ray photoelectron spectroscopic analysis of oxidized Fe–16Cr–16Ni–2Mn–1Mo–2Si austenitic stainless steel, Appl. Surf. Sci. 253 (2007) 4872–4885.

[27] F.. Pérez, M.. Hierro, C. Gómez, L. Martínez, D. Duday, Silicon ion implantation on austenitic and ferritic stainless steels against localized aqueous corrosion, Surf. Coatings Technol. 133-134 (2000) 344–350.

[28] R. Nishimura, K. Yamakawa, J. Ishiga, Y. Matsumoto, H. Nagano, Highly corrosion resistant stainless steel with Si implanted/deposited phase, Mater. Chem. Phys. 54 (1998) 289–292.

[29] a. Sharon, D. Itzhak, Mechanical properties of sintered austenitic stainless steel—effect of silicon addition, Mater. Sci. Eng. A. 157 (1992) 145–149.

[30] C. Suryanarayana, Mechanical alloying and milling, Prog. Mater. Sci. 46 (2001) 1–184.

[31] C. Suryanarayana, E. Ivanov, V.. Boldyrev, The science and technology of mechanical alloying, Mater. Sci. Eng. A. 304-306 (2001) 151–158.

[32] W. Chen, U. Anselmi-Tamburini, J.E. Garay, J.R. Groza, Z. a. Munir, Fundamental investigations on the spark plasma sintering/synthesis process, Mater. Sci. Eng. A. 394 (2005) 132–138.

[33] M. Omori, Sintering , consolidation , reaction and crystal growth by the spark plasma system (SPS), 287 (2000) 183–188.

[34] O. Guillon, J. Gonzalez-Julian, B. Dargatz, T. Kessel, G. Schierning, J. Räthel, et al., Field-Assisted Sintering Technology/Spark Plasma Sintering: Mechanisms, Materials, and Technology Developments, Adv. Eng. Mater. 16 (2014) 830–849.

[35] Z.A. Munir, U. Anselmi-Tamburini, M. Ohyanagi, The effect of electric field and pressure on the synthesis and consolidation of materials: a review of the spark plasma sintering method, J. Mater. Sci. 41 (2006) 763–777.

[36] X. Song, X. Liu, J. Zhang, Neck Formation and Self-Adjusting Mechanism of Neck Growth of Conducting Powders in Spark Plasma Sintering, J. Am. Ceram. Soc. 89 (2006) 494–500.

[37] R.K.S. Raman, R.K. Gupta, Oxidation resistance of nanocrystalline vis-à-vis microcrystalline Fe–Cr alloys, Corros. Sci. 51 (2009) 316–321.

[38] R.K. Gupta, R.K. Singh Raman, C.C. Koch, Fabrication and oxidation resistance of nanocrystalline Fe10Cr alloy, J. Mater. Sci. 45 (2010) 4884–4888.

[39] I. Toor, Effect of Sintering Holding Time on the Corrosion Properties of Nano-Structured Fe-18Cr-2Si Alloy Prepared by SPS, 11 (2016) 2897–2908.

[40] A. Bautista, A. González-Centeno, G. Blanco, S. Guzmán, Application of EIS to the study of corrosion behaviour of sintered ferritic stainless steels before and after high-temperature exposure, Mater. Charact. 59 (2008) 32–39.

[41] D. Wallinder, J. Pan, C. Leygraf, a. Delblanc-Bauer, EIS and XPS study of surface modification of 316LVM stainless steel after passivation, Corros. Sci. 41 (1998) 275–289.

[42] A.S. Hamdy, Electrochemical Impedance Spectroscopy Study of the Corrosion Behavior of Some Niobium Bearing Stainless Steels in, Int. J. Electrochem. Sci. 1 (2006) 171–180.

[43] J. Pan, C. Leygraf, R.F. a Jargelius-Pettersson, J. Linden, Characterization of High-Temperature Oxide Films on Stainless Steels by Electrochemical-Impedance Spectroscopy, Oxid. Met. 50 (1998) 431–455.

[44] C.M. Abreu, M.J. Cristóbal, R. Losada, X.R. Nóvoa, G. Pena, M.C. Pérez, The effect of Ni in the electrochemical properties of oxide layers grown on stainless steels, Electrochim. Acta. 51 (2006) 2991–3000.

[45] M. a. Ameer, a. M. Fekry, F.E.-T. Heakal, Electrochemical behaviour of passive films on molybdenum-containing austenitic stainless steels in aqueous solutions, Electrochim. Acta. 50 (2004) 43–49.

[46] U. Patil, S.J. Hong, C. Suryanarayana, An unusual phase transformation during mechanical alloying of an Fe-based bulk metallic glass composition, J. Alloys Compd. 389 (2005) 121–126.

[47] B. Movahedi, M.H. Enayati, C.C. Wong, Study on nanocrystallization and amorphization in Fe–Cr–Mo–B–P–Si–C system during mechanical alloying, Mater. Sci. Eng. B. 172 (2010) 50–54.

[48] S. Sharma, C. Suryanarayana, Mechanical crystallization of Fe-based amorphous alloys, J. Appl. Phys. 102 (2007).

[49] M. Falcão de Oliveira, A simple criterion to predict the glass forming ability of metallic alloys, J. Appl. Phys. 111 (2012) 023509.

[50] N. Al-Aqeeli, C. Suryanarayana, M.A. Hussein, Formation of an amorphous phase and its crystallization in the immiscible Nb-Zr system by mechanical alloying, J. Appl. Phys. 114 (2013).

[51] T. Egami, Y. Waseda, Atomic size effect on the formability of metallic glasses, J. Non. Cryst. Solids. 64 (1984) 113–134.

[52] M. Yousefi, S. Sharafi, The effect of simultaneous addition of Si and Co on microstructure and magnetic properties of nanostructured iron prepared by mechanical alloying, Mater. Des. 37 (2012) 325–333.

[53] V. Mote, Y. Purushotham, B. Dole, Williamson-Hall analysis in estimation of lattice strain in nanometer-sized ZnO particles, J. Theor. Appl. Phys. 6 (2012) 6.

[54] B. Cantor, Novel nanocrystalline alloys and magnetic nanomaterials, CRC Press, 2004.

[55] M.A. Hussein, C. Suryanarayana, M.K. Arumugam, N. Al-Aqeeli, Effect of sintering parameters on microstructure, mechanical properties and electrochemical behavior of Nb–Zr alloy for biomedical applications, Mater. Des. 83 (2015) 344–351.

[56] C.X. Huang, G. Yang, Y.L. Gao, S.D. Wu, Z.F. Zhang, Influence of processing temperature on the microstructures and tensile properties of 304L stainless steel by ECAP, Mater. Sci. Eng. A. 485 (2008) 643–650.

[57] L. Cheng, Z. Xie, G. Liu, W. Liu, W. Xue, Densification and mechanical properties of TiC by SPS-effects of holding time, sintering temperature and pressure condition, J. Eur. Ceram. Soc. 32 (2012) 3399–3406.

[58] Y. Zhao, L.-J. Wang, G.-J. Zhang, W. Jiang, L.-D. Chen, Effect of holding time and pressure on properties of ZrB2–SiC composite fabricated by the spark plasma sintering reactive synthesis method, Int. J. Refract. Met. Hard Mater. 27 (2009) 177–180.

[59] Z.-F. Liu, Z.-H. Zhang, J.-F. Lu, A. V. Korznikov, E. Korznikova, F.-C. Wang, Effect of sintering temperature on microstructures and mechanical properties of spark plasma sintered nanocrystalline aluminum, Mater. Des. 64 (2014) 625–630.

[60] M.A. Auger, T. Leguey, A. Muñoz, M.A. Monge, V. De Castro, P. Fernández, et al., Microstructure and mechanical properties of ultrafine-grained Fe-14Cr and ODS Fe-14Cr model alloys, J. Nucl. Mater. 417 (2011) 213–216.

[61] S. Guo, A. Chu, H. Wu, C. Cai, X. Qu, Effect of sintering processing on microstructure , mechanical properties and corrosion resistance of Ti – 24Nb – 4Zr – 7 . 9Sn alloy for biomedical applications, J. Alloys Compd. 597 (2014) 211–216.

[62] A. Bautista, A. González-Centeno, G. Blanco, S. Guzmán, Application of EIS to the study of corrosion behaviour of sintered ferritic stainless steels before and after high-temperature exposure, Mater. Charact. 59 (2008) 32–39.

[63] P. Gu, B. Arsenault, J.. Beaudoin, J.-G. Legoux, B. Harvey, J. Fournier, Polarization Resistance of Stainless Steel-Coated Rebars, Cem. Concr. Res. 28 (1998) 321–327.

[64] V. de Freitas Cunha Lins, G.F. de Andrade Reis, C.R. de Araujo, T. Matencio, Electrochemical impedance spectroscopy and linear polarization applied to evaluation of porosity of phosphate conversion coatings on electrogalvanized steels, Appl. Surf. Sci. 253 (2006) 2875–2884.

[65] F. Xie, X. He, S. Cao, M. Mei, X. Qu, Influence of pore characteristics on microstructure, mechanical properties and corrosion resistance of selective laser sintered porous Ti-Mo alloys for biomedical applications, Electrochim. Acta. 105 (2013) 121–129.

[66] X.. Wang, D.. Li, Mechanical and electrochemical behavior of nanocrystalline surface of 304 stainless steel, Electrochim. Acta. 47 (2002) 3939–3947.

[67] W.-T. Tsai, Y.-N. Wen, J.-T. Lee, H.-Y. Liou, W.-F. Wang, Effect of silicon addition on the microstructure and corrosion behavior of sintered stainless steel, Surf. Coatings Technol. 34 (1988) 209–217.

[68] S. Todde, R. Licheri, R. Orrù, G. Cao, Spark plasma sintering processing for the evaluation of cryomilled CoNiCrAlY alloys for high temperature applications in oxidizing environment, Chem. Eng. J. 200-202 (2012) 68–80.

[69] R. Robin, F. Miserque, V. Spagnol, Correlation between composition of passive layer and corrosion behavior of high Si-containing austenitic stainless steels in nitric acid, J. Nucl. Mater. 375 (2008) 65–71.

[70] M. Vuković, B. Pesic, N. Štrbac, I. Mihajlović, M. Sokić, Linear polarization study of the corrosion of iron in the presence of Thiobacillus ferrooxidans bacteria, Int. J. Electrochem. Sci. 7 (2012) 2487–2503.

[71] J. Lv, H. Luo, Comparison of corrosion behavior between coarse grained and nano/ultrafine grained 304 stainless steel by EWF, XPS and EIS, J. Nucl. Mater. 452 (2014) 469–473.

[72] C. García, F. Martín, Y. Blanco, M.P. de Tiedra, M.L. Aparicio, Corrosion behaviour of duplex stainless steels sintered in nitrogen, Corros. Sci. 51 (2009) 76–86.

[73] U. Patil, S.-J. Hong, C. Suryanarayana, An unusual phase transformation during mechanical alloying of an Fe-based bulk metallic glass composition, J. Alloys Compd. 389 (2005) 121–126.

[74] S.. Kaloshkin, V.. Tcherdyntsev, I.. Tomilin, Y.. Baldokhin, E.. Shelekhov, Phase transformations in Fe–Ni system at mechanical alloying and consequent annealing of elemental powder mixtures, Phys. B Condens. Matter. 299 (2001) 236–241.

[75] M.H. Enayati, M.R. Bafandeh, Phase transitions in nanostructured Fe–Cr–Ni alloys prepared by mechanical alloying, J. Alloys Compd. 454 (2008) 228–232.

[76] D. Oleszak, A. Grabias, M. Pękała, A. Świderska-Środa, T. Kulik, Evolution of structure in austenitic steel powders during ball milling and subsequent sintering, J. Alloys Compd. 434-435 (2007) 340–343.

[77] T. Haghir, M.H. Abbasi, M.A. Golozar, M. Panjepour, Investigation of α to γ transformation in the production of a nanostructured high-nitrogen austenitic stainless steel powder via mechanical alloying, Mater. Sci. Eng. A. 507 (2009) 144–148.

[78] F. Tehrani, M.H. Abbasi, M. a. Golozar, M. Panjepour, The effect of particle size of iron powder on α to γ transformation in the nanostructured high nitrogen Fe–Cr–Mn–Mo stainless steel produced by

mechanical alloying, Mater. Sci. Eng. A. 528 (2011) 3961–3966.

[79] E. Salahinejad, R. Amini, M. Marasi, M.J. Hadianfard, The effect of sintering time on the densification and mechanical properties of a mechanically alloyed Cr-Mn-N stainless steel, Mater. Des. 31 (2010) 527–532.

[80] E. Otero, a. Pardo, M. V. Utrilla, E. Sáenz, J.F. Álvarez, Corrosion behaviour of AISI 304L and 316L stainless steels prepared by powder metallurgy in the presence of sulphuric and phosphoric acid, Corros. Sci. 40 (1998) 1421–1434.

Vitae

Name :Junaid Ahmed

Nationality :Pakistani

Date of Birth :6/21/1990

Email :engr.mjas@gamil.com

Address :Muhajir colony, street no 15, kocha talib hussain, Sadiq Abad, Distt.
Rahim yar khan

Academic Background :Master in Materials Science and Engineering

Research Achievements

J. Ahmed, M. R. Yousaf, U. Hayat, M. O. Lari, and I.H. Toor," Effect of Heat Treatment on the Electrochemical properties of Galvanized Steel in stripping solution," Technical paper in 2016 Middle East Corrosion Conference (Won "Best young Professional 2016" award)

Junaid Ahmed, Ihsan ul Haq Toor, "Effect of holding time on the corrosion properties of nano-structured Fe-18Cr-2Si alloys prepared by mechanical alloying followed by spark plasma sintering," Poster in 16th MECC 2016 (Presented).

Ihsan-ul-haq toor, Junaid Ahmed, N.Al-Aqeeli, M.A. Hussein ,"Synthesis of Fe-Cr-Si alloys by Spark Plasma Sintering" Powder Technology. (2nd Revision Submitted).

Junaid Ahmed, Ihsan-ul-haq toor," Amorphization and Mechanical crystallization of Fe-Cr alloy during mechanical alloying", Journal of Alloys and Compounds (Accepted)